



Herrera Martín, Antonio (2018) Wave dark matter as a gravitational lens for electromagnetic and gravitational waves. PhD thesis.

<http://theses.gla.ac.uk/9027/>

Copyright and moral rights for this work are retained by the author

A copy can be downloaded for personal non-commercial research or study, without prior permission or charge

This work cannot be reproduced or quoted extensively from without first obtaining permission in writing from the author

The content must not be changed in any way or sold commercially in any format or medium without the formal permission of the author

When referring to this work, full bibliographic details including the author, title, awarding institution and date of the thesis must be given

Enlighten:Theses
<http://theses.gla.ac.uk/>
theses@gla.ac.uk

Wave Dark Matter as a Gravitational Lens for Electromagnetic and Gravitational Waves

Antonio Herrera Martín, M.Phys.

Astronomy and Astrophysics Group
School of Physics and Astronomy
Kelvin Building
University of Glasgow
Glasgow, G12 8QQ
Scotland, U.K.



Presented for the degree of
Doctor of Philosophy
The University of Glasgow
April 2018

This thesis is my own composition except where indicated in the text.
No part of this thesis has been submitted elsewhere for any other degree
or qualification.

Copyright © 2018 by Antonio Herrera Martin

The oldest and strongest emotion of mankind is fear, and the oldest and strongest kind of fear is fear of the unknown. - H. P. Lovecraft

And if he left off dreaming about you, where do you suppose you'd be? - Lewis Carroll,
Through the Looking-Glass

Abstract

The majority of the matter in the known universe is believed to be in the form of Dark Matter, and its widely accepted description is done by Cold Dark Matter (CDM). Nevertheless, its exact properties and composition are still unknown, and it is one of the most active areas of research in Cosmology.

The use of Cold Dark Matter has been successful to describe the general behaviour of Dark Matter at large scales. However, it has encountered problems explaining phenomena at other regimes as on the scale of galaxy halos. Therefore, other models have been proposed over time which are able to retain the reasonable success of CDM on large scales and extend it to other regimes where CDM has problems to explain the observed data. One of such models is Scalar field Dark Matter (SFDM). Its properties allow it to produce similar results at large scales and solve the problems encountered at galactic scales. Nevertheless, the difficulty to obtain direct observations of Dark Matter makes it difficult to give a definitive comparison between the models. Therefore, it is important to study dark matter through different methods of analysis that would allow to increase the validity of its scope, and these methods are constantly being researched.

In this work, a particular density profile known as Wave Dark Matter is implemented as a gravitational lens to study its behaviour in the cases where it produces strong lensing of light and of gravitational waves. Analytical functions for the description of a soliton core and a soliton core + NFW tail are applied to a sub-sample of 6 galaxies from The Sloan Lens ACS Survey to constrain the lensing parameters and their relation with the profile. Furthermore, by considering the soliton core to be the main contributor to the mass profile, this is implemented as a lens for the case of the wave approximation

and further to describe the major effects of the lens on gravitational waves.

It was found that the soliton core is too compact and dense in order to reproduce the observed values of the data for the lensed galaxies. However, adding a NFW tail alleviates the problem and reaches radii and masses within the range reported in the literature, although the size of the NFW tail cannot be properly constrained. Meanwhile for gravitational waves, it was found that the lensing parameters of the soliton core, if they are expected to describe a galaxy, will be such that they are more likely to be observed spaceborne gravitational wave detectors.

In summary, therefore, a wave dark matter soliton in combination with a NFW tail is able to represent a galaxy, and the combination of light and gravitational waves should give new insight on the validity of the profile as a description of Dark Matter galactic haloes.

Contents

List of Tables	v
List of Figures	vii
Preface	xvi
Acknowledgements	xviii
1 Introduction	1
1.1 Modern Cosmology	4
1.1.1 Relativity	4
1.1.2 The early universe	7
1.2 Standard model of cosmology	11
1.2.1 Homogeneity and isotropy	11
1.2.2 Friedmann Equation	14
1.2.3 Λ CDM	15
1.2.4 Dark Matter	16
1.3 Scalar Field Dark Matter	18
2 Gravitational lensing	21
2.1 The bending of light	21
2.2 Lens equation	22
2.2.1 Point like lens	23
2.3 Time Delay	24
2.3.1 Lensing Potential and Fermat potential	25

2.3.2	Caustics and critical curves	25
2.4	Extended mass distribution	26
2.5	Most common lensing profiles	27
2.5.1	SIS profile	27
2.5.2	NFW profile	28
2.5.3	Burkert profile	29
2.6	Types of lensing	30
2.6.1	Strong lensing	30
2.6.2	Weak lensing	31
2.6.3	Microlensing	32
3	Bayesian inference for data analysis	33
3.1	Bayesian inference	34
3.1.1	Bayes' theorem	35
3.1.2	Hypothesis space	36
3.1.3	Marginalization	37
3.2	Parameter estimation	39
3.3	Model comparison	40
3.4	Markov Chain Monte Carlo (MCMC)	42
3.5	Nested sampling	44
3.5.1	Multinest	47
4	Lensing of scalar field dark matter	48
4.1	The reduced lens equation	48
4.2	Ultra light Dark Matter profiles	50
4.2.1	BEC or general SFDM profile	51
4.2.2	ψ DM soliton profile	51
4.3	Gravitational lensing with a SFDM profile	52
4.4	Gravitational lensing with a WaveDM profile	54
4.5	A more complete density profile	58

4.5.1	Surface mass density	60
4.5.2	Gravitational Lensing Mass	64
5	Galaxy analysis	67
5.1	Matching properties	67
5.2	Data analysis	72
5.2.1	Galaxy sample	72
5.2.2	Soliton core	73
5.2.3	Complete profile	79
5.2.4	Summary of results	90
6	Wave optics for gravitational lensing	92
6.1	Diffraction integral	93
6.1.1	The lensing system	93
6.1.2	The amplification factor	94
6.1.3	Geometrical optics approximation	95
6.2	Lens models	96
6.2.1	The point mass lens	96
6.2.2	Singular Isothermal Sphere(SIS) - lens	97
6.2.3	NFW lens	98
6.2.4	ψ DM - soliton lens	101
6.3	Comparison of lens properties	102
6.3.1	NFW and Soliton	104
6.3.2	Summary	105
7	Gravitational lensing of gravitational waves	106
7.1	Gravitational lensing effects	106
7.1.1	Effects on the lensed wave	107
7.1.2	Effects on parameter estimation	110
7.1.3	The soliton lens revisited	114
7.2	Lensing of a gravitational wave	121

7.2.1	Applying the amplification factor	122
7.2.2	Lensed signals	122
7.2.3	Summary	132
8	Concluding remarks and future work	134
	Bibliography	137
A	Galaxy posteriors	152
A.1	Posteriors for $M_s = 10^{11.5}$	153
A.2	Posteriors for $M_s < 10^{11.5}$	156
B	Lensing figures	160

List of Tables

4.1	A comparison of λ_{cr} for several profiles [90, 138, 42]. They are obtained by eq. (4.7).	56
5.1	List of selected galaxies from SLACS. These were selected because they have a fraction of luminous matter of 0.5 or less; see the values in the second column. Column (1) gives the label of the galaxies within the SDSS catalog, column (2) indicates the fraction of luminous matter and dark matter. Column (6) lists the measured Einstein radius in units of kpc.	73
5.2	The values of the soliton radius in the logarithmic scale $\log_{10}(r_s/\text{pc})$ obtained from the fits to the indicated galaxies, for three different values of the boson mass m_a	78
5.3	The values of the soliton density in the logarithmic scale $\log_{10}(\rho_s/M_\odot\text{pc}^{-3})$ obtained from the results of the radius from the different galaxy fits. The inverse relationship between the radius and density is clear, as for the largest radii, they possess smallest density, which preserves the soliton mass constant for the galaxy.	79
7.1	Expected numbers of lensed GW events from inspiralling DCOs of different classes under different evolutionary scenarios. Predictions for the Einstein Telescope in the initial and “xylophone” configuration. Table taken from [8].	111
7.2	Mass and physical parameters for the different lenses by considering similar source position of $y = 0.1$ and a normalization length $\xi_0 = 10\text{kpc}$	131

7.3	Mass and physical parameters for a soliton lens with a BH-BH source with total mass of $100 M_{\odot}$	132
-----	---	-----

List of Figures

1.1	Dante’s Scheme of the Universe. From Studies in the History and Method of Science, ed. by Charles Singer, 1917, Vol. I, Fig. 4.	3
1.2	a) Shows the simplest idea of space-time in special relativity and the concept of preservation of space-time interval. b) Shows in a simple manner an object with mass curving the space-time. The red arrows point to representation of “shortest paths” which defines the notion of geodesic.	5
1.3	Evolution fo the universe	11
1.4	A simple sketch exemplifying the homogeneity at larger scales. Below 100 Mpc, the galactic distributions seems lumpy. Above this, the distribution becomes regular the universe seems homogeneous up to the limit of the observable universe.	12
1.5	An all-sky map of temperatures from Planck mission of the CMBR [94]. Red and blue colours indicate warmer and cooler fluctuations with respect the mean temperature of 2.72 kelvin. These are extremely dim variations as they are just one part in 100,000. By ESA and the Planck Collaboration.	13
1.6	The relative amounts of the different constituents of the Universe. Image credit: ESA/Planck.	16
1.7	Representation of the observed comparison between the predicted rotation derived from Kepler’s Law and the observed velocity curves of galaxies.	17

2.1	Diagram showing the light path from the source to the observer, deflected by a mass in the lens plane. The diagram shows a point-like lens, but a similar diagram can be used to represent light deflection by a symmetric extended distribution.	24
2.2	Comparison of the three example profiles by a central density, ρ_0 and normalization length, r_0 . For the case of the SIS, it was defined $\rho_0 = \sigma^2/Gr_0^2$. For NFW and Burkert profiles $r_0 = r_s$. It is clear that the SIS and NFW profiles diverge at the centre, meanwhile the Burkert and NFW are similar at large radii.	29
2.3	Example of strong lensing. A luminous red galaxy distorting a more distant blue galaxy. By ESA/Hubble & NASA derivative work: Bulwersator via Wikimedia Commons.	30
2.4	Representation of the process of weak lensing. The image of several background sources is slightly distorted by a lens. The aberration is so weak that the effect is found by identifying discernible patterns in the statistical distribution of sources.	31
3.1	Sketch representing the mapping from the prior mass curve $X(L)$, at the right to the parameter space, at the left, which describes the boundaries of equivalent likelihood \mathcal{L}	45
4.1	The plot of the reduced lens equation for SFDM profile gives the basic idea of the effect that different values of λ produce for the generation of strong lensing. Multiple images, and at the same time the effect of lensing, are created when there is a zero crossing which corresponds to the value of the Einstein radius, θ_{*E}	53
4.2	Plot of the WaveDM profile (4.14), which shows the steep decrease with radius. The profile is normalized by the central density, ρ_s , and the radius by the characteristic radius, r_s	55

-
- 4.3 Einstein radius as a function of λ . This shows the relation between the different profiles and the values of λ necessary to produce an specific Einstein radius. The minimum value of λ is the corresponding λ_{cr} 57
- 4.4 Comparison between the complete profile and the individual densities with $r_{\epsilon^*} = 0.300845$ and $\alpha_{NFW} = 1$. The initial value for the complete profile is normalized to the soliton density and the radii to r_s , so the transition happens at $\epsilon = 0.5$. This was chosen arbitrarily. It can be seen how the individual profiles intersect, and the transition happens. The effect of the soliton section helps to eliminate the divergence present in the NFW profile. 59
- 4.5 Plot of the surface mass density as a function of arbitrarily selected values of $r_{\epsilon^*} = 2.5$ and $\alpha_{NFW} = 1$. The vertical line shows the transition between the branches for the density. There is a minimum value which is obtained at $\xi_* = 0$ 62
- 5.1 The normalized density profile of the soliton together with different examples of the normalized NFW profile. It is shown here that there are at most two values of the matching radius r_{ϵ^*} , which depend on the given values of the normalized density ρ_{NFW^*} and α_{NFW} (here $\alpha_{NFW} = 1$ is taken). 68
- 5.2 The normalized density ρ_{NFW} as a function of the matching radius r_{ϵ^*} , for different values of α_{NFW} , as indicated by eq. (4.27c). Notice that there are two possible values of r_{ϵ^*} for any given value of ρ_{NFW^*} , except for the maximum value of the latter. The vertical lines represent the minimum and maximum possible values for the peak of ρ_{NFW^*} for the range $0 \leq \alpha_{NFW} \leq \infty$ 70
- 5.3 The critical value λ_{cr} as a function of r_{ϵ^*} . for different values of α_{NFW} . The soliton alone value of $\lambda_{cr} \simeq 0.48$ is compared with several different α_{NFW} . The constraint $r_{\epsilon^*} \geq r_{\epsilon^*max}$ is considered. 71

5.4	Illustration of the use of eq. 5.8 to constrain the parameters for the soliton. The curves are shown for selected values of m_{a22} and how the left-hand side varies as a function of the Einstein angle. The vertical lines represent the range of values which satisfy the different samples.	76
5.5	Parameter constraint for the soliton case of galaxy J0008-0004. Only one parameter is represented, for the three selected values of boson mass.	77
5.6	Total mass M normalized by terms of the soliton mass M_s . It is important to notice that M can be up to three orders of magnitude compared with the the soliton mass. This is obtained just by integration of eq. (5.5) with an upper limit of $r_* = 20$. The black line represents $r_{\epsilon_*} = 1$, and the blue and purple lines are set as the range $0.25 < r_{\epsilon_*,max} < 0.48$.	80
5.7	Posteriors for galaxies J0008-0004 and J0935-0003. On the graph there is a clear delimitation of the area which the parameters can obtain to satisfy the lens mass given for the galaxies. The clear line shows where the soliton dominates and the rest gray area are the values for the NFW tail whose contribution is negligible.	84
5.8	Posteriors for a configuration of $m_{a22} = 1$ and $\log(M_s/M_\odot) = 11.5$. The larger radii show a flat prior, which turns out to be a reasonable explanation considering that at these values the contribution of the tail in negligible.	85
5.9	Posteriors for a configuration of $m_{a22} = 0.1$ and $\log(M_s/M_\odot) = 11.5$. The output is almost flat, and it only describes a minimum accepted value of radii.	86
5.10	Posterior for galaxy J0008-0004. Description is found in text.	88
5.11	Posterior for galaxy J0935-0003. Description is found in text.	89
6.1	The lensing system considering a wave emitted by a source which passes close to a gravitational lens. A wavelength comparable with the Schwarzschild radius of the lens will produce a diffraction effect.	94

- 6.2 Amplification factor for the point mass lens. a) The amplitude of the lens for $y = 0.3$ and $y = 1.0$. The values with high oscillation correspond to $w > 1$; as the frequency w increases it approaches to the geometrical limit. b) The phase of the point mass lens amplification factor. The selection of the phase constant allows the phase to be contained within a range of values of θ , and it can be seen how the increase in w produces the oscillatory effect on the phase, similar to the amplitude. 98
- 6.3 Amplification factor for Singular Isothermal Sphere (SIS). a) The amplitude of the SIS, as well as the point mass presents the same oscillatory pattern when $w > 1$, but for the same value of y the amplification of the amplitude is bigger for the SIS. As y increases, the oscillation in the amplitude is decreases but this in principle settles, which corresponds to the value in the geometric optics. b) The phase oscillates for higher values, but it is still bounded inside a region; the phase at the same time presents the same decreasing behaviour for increasing y 99
- 6.4 The NFW profile requires a different approach and has the extra parameter ks . Both of the images correspond to the case $k_s = 1$. a) The amplitude of the amplification factor is plotted for two examples of y which is normalized by y_{crit} which corresponds to the radial caustic. b) The phase in this case decays faster than in the previous profiles, and for the case where there is not decay, there is an abrupt change. 100
- 6.5 The soliton profile amplification factor for the fixed value of $ks = 2$. a) The amplitude of y is normalized by y_{crit} . It has three values, $y/y_{crit} = 0.3, y/y_{crit} = 1, y/y_{crit} = 2.0$. b) The phase has an oscillatory pattern due to the diffraction and image interference, but above y_{crit} the oscillations decrease and disappear at sufficiently high frequency as there is only one image produced. 103

- 7.1 Frequency distribution of the signal-to-noise ratio against for several configurations of point mass lenses, and positions y . It presents several deviations from the unlensed case as well as the oscillatory pattern which could represent a signature of gravitational lensing. Figure taken from [80]. 108
- 7.2 The top panel shows the mapping of the intrinsic redshift z and the inferred redshift \tilde{z} for contours of constant magnification μ , red lines, and fixed ratios of inferred and intrinsic mass \tilde{M}/M . The bottom panel shows the same plot but for lower redshifts. Taken from [28]. 113
- 7.3 The relation of k_s on the lens equation which affects the adimensional frequency. (a) is the case for no strong lensing which is a value below $k_s \approx 1.52$. In (b), $k_s = 2$, there is strong lensing, but r_s is bigger than the Einstein radius which means that w is bigger as well. The dashed lines show the transition from multiple to a single image and defines y_{crit} . (c) presents the case for $k_s = 10$ where the Einstein radius $\sim r_s$, and y_{crit} is closer to the unity in this case. 116
- 7.4 Density plot of the amplification factor for $k_s = 2.0$. Left side plot is the amplitude and the right is the phase. Oscillatory regions can be observed due to the multiple image interaction. 117
- 7.5 Density plots for $k_s = 5.0$. Left image is the amplitude of the amplification factor F , and the right image is the phase. The amplitude has a clear decrease in magnification after $y/y_{crit} = 1$ which is the transition between multiple image interaction and a single image. 118
- 7.6 Density plots for $k_s = 10.0$. The left and right images are the amplitude and phase of F , respectively. Different from the previous density plots, in this case the Einstein radius is almost the characteristic length of the profile, and low amplification can be observed in general. 119
- 7.7 Amplification factors for $y/y_{crit} = 0.1, 1.2$ and 2.0 for $k_s = 2$. Left plots are the amplitude, $|F|$ and Right are the phase, θ_F . The overall magnification can be seen to be up to 30 times for the lowest value of y , and it can be seen to be considerable even for bigger values. 120

- 7.8 Amplification factors for $y/y_{crit} = 0.1, 1.2$ and 2.0 for $k_s = 5$. Left plots are the amplitude, $|F|$ and Right are the phase, θ_F . Compared to the $k_s = 2$ the magnification is an order of magnitude lower, but still significant for the lower value; nevertheless, $y/y_{crit} > 1$ presents magnifications lower than 2. The phase oscillations decrease as well as the magnitude. 120
- 7.9 Amplification factors for $y/y_{crit} = 0.1, 1.2$ and 2.0 for $k_s = 10$. Left plots are the amplitude, $|F|$ and Right are the phase, θ_F . The overall magnification is slightly greater than 2 for the lowest y , meanwhile any of the values above $y/y_{crit} > 1$ presents no magnification whatsoever, and just small rippling due to the image diffracted by the central region. The phase follows a similar behaviour as the magnitude. 121
- 7.10 Form of the function $h(f)$ which was used as source signal. At the left, it is the magnitude, and at the right the phase. This is the generated source from the PhenomD model. 123
- 7.11 Unlensed Source signal, $h(t)$, which is the time domain version of $h(f)$. This is used as the source signal for the lensing. 123
- 7.12 Comparison of different lens type waves against unlensed by considering lensed mass equal to the source mass and $y = 0.1$. The left plot is the amplitude, and the right is the phase of the wave. Only the amplitude shows and magnification. 124
- 7.13 Comparison of the magnification amplitude for source positions $y = 1.2$ and $y = 2$ for a ratio $M_{z\text{lens}}/M_{\text{source}} = 1$ 125
- 7.14 Comparison of different lens type waves against unlensed by considering a lens a 100 times the mass of the source, and a position of $y = 0.1$. The left plot is the amplitude, which clearly shows a big magnification and oscillatory pattern from the magnification factor. The right is the phase of the wave. Compared with the amplitude, the phase presents oscillations, but they do not show any significant modification for the unlensed case. 126

7.15	Comparison of the magnification amplitude for source positions $y = 1.2$ and $y = 2$ for a ratio $M_{z\text{lens}}/M_{\text{source}} = 100$	127
7.16	Gravitational wave in the time domain. The axes are the normalized time with the source mass, and the amplitude of the strain h . a) Shows the time domain version of the amplitude of fig. 7.14. It is clear that there is an major modification on the wave. b) Corresponds to the time domain version of the amplitude of fig. 7.15 for $y = 2$ where there is no change if compared c), which is the unlensed wave with parameters $q = m_1/m_2 = 1$, $\chi_1 = \chi_2 = 0$	128
A.1	Posteriors for a configuration soliton+NFW tail considering $m_{a22} = 10$ and a soliton mass $M_s = 10^{11.5}$. The Galaxy labels is specified in each subfigure, and description in chapter 5.	153
A.2	Posteriors for a configuration soliton+NFW tail considering $m_{a22} = 1$ and a soliton mass $M_s = 10^{11.5}$. A transition value where the soliton has dominance is clearly delimited. The Galaxy labels is specified in each subfigure, and description in chapter 5.	154
A.3	Posteriors for a configuration soliton+NFW tail considering $m_{a22} = 0.1$ and a soliton mass $M_s = 10^{11.5}$. This is the particular case where the soliton dominates the configuration. This has the particular feature that the configuration of the tail is irrelevant. The Galaxy labels is specified in each subfigure, and description in chapter 5.	155
A.4	Posteriors for a configuration soliton+NFW tail considering different axion masses and soliton mass $M_s < 10^{11.5}$. The Galaxy labels is specified in each subfigure, and description in chapter 5.	156
A.5	Posteriors for a configuration soliton+NFW tail considering different axion masses and soliton mass $M_s < 10^{11.5}$. The Galaxy labels is specified in each subfigure, and description in chapter 5.	157

A.6	Posteriors for a configuration soliton+NFW tail considering different axion masses and soliton mass $M_s < 10^{11.5}$. The Galaxy labels is specified in each subfigure, and description in chapter 5.	158
A.7	Posteriors for a configuration soliton+NFW tail considering different axion masses and soliton mass $M_s < 10^{11.5}$. The Galaxy labels is specified in each subfigure, and description in chapter 5.	159
B.1	Source	161
B.2	Point mass	161
B.3	Soliton core similar to point mass	162
B.4	Soliton core below λ_{crit}	162
B.5	Soliton core with $\lambda = 5$	163
B.6	WaveDM similar to Soliton	164
B.7	WaveDM with $r_{\epsilon^*} = 0.5$	165
B.8	WaveDM with $\lambda = 5$	165

Preface

This thesis deals with the use of gravitational lensing in the regime of strong lensing by applying a Wave Dark Matter profile. This is done for the traditional description of light by using geometric lensing, but also includes a description of several profiles in the wave approximation for gravitational waves. A brief description and outline of the chapters is found in the following paragraphs.

Chapter 1 introduces the reader to the background cosmology followed during the thesis. It starts with a brief historical introduction of the Hot Big Bang model, and the overall view of the universe described by it. This is followed by a more technical description of the standard cosmological model establishing the basic idea for dark matter, with its successes and challenges, and introducing the type of model that will be used in the thesis.

Chapter 2 presents the standard formalism for gravitational lensing. In particular, it shows several of the profiles used in lensing, especially considering the geometrical optics approximations. Also, it presents some of the concepts of lensing used in later chapters.

Chapter 3 presents a brief introduction of several concepts for Bayesian inference. These are presented to the reader to ease the understanding the discussion and analysis given in later chapters.

Chapter 4 presents formally the profile distribution which is going to be analysed on the rest of the thesis. Also, it includes a brief discussion of other profiles with similar properties. Additionally, the main part introduces the normalization used, and it presents the equations necessary to describe the Wave Dark Matter profile as a

gravitational lens which were derived for the first time for the work carried out in this thesis, and it also sets out the conditions for strong lensing.

Chapter 5 describes the analysis done with a selected sample of data using the derived equations introduced on the previous chapter. The data analysis presented is done using Bayesian inference. A discussion of the results found is at the end of this chapter.

Chapter 6 is a brief introduction to the lensing effect on the wave approximation. It introduces the formalism used, presents results for several profiles already found in literature, and shows how the Wave Dark Matter profile is used in this approximation as a lens and briefly compares, and highlights, its differences with the other lenses.

Chapter 7 reviews importance of lensing for the detection of gravitational waves and presents a qualitative analysis of several profiles, with major attention given for Wave Dark Matter, and their consequences for future detections of lensed signal.

Finally, chapter 8 presents the conclusions of the thesis and description for future work.

Acknowledgements

In first instance, I would like to thank the Mexican National Council of Science and Technology (CONACYT) for the scholarship that made this work possible. To the University of Glasgow and SUPA for the Mobility support which allowed me to visit The University of the Balearic Islands and the Chinese University of Hong Kong.

Secondly to my supervisor Prof. Martin Hendry; without his support this work could not had taken shape. For his guidance and encouragement during this several years allowing me to expand this research, and enduring with me despite his busy schedule he always found a way to accommodate a last time meeting.

I am very grateful to Dr. Luis Ureña, who introduced me to the field of research, and to Dr. Alma Gonzales. An important part of this thesis would not be possible without their collaboration during this study.

Certainly, I appreciate the support of my parents and my brother who always tried to help in whatever was possible. Inadvertently, they put me in the path of science, and they always encourage my studies.

Special thanks to Atalia for being the sister I never had and surviving my constant nonsense, to Rafa for being a great friend and giving me support when needed, to Francesco for all those afternoon coffees of random talks, and to Adela for listening when needed. Equally thanks to the people in room 604: Ben, Stephen, Dina, Paul, Duncan, Graham, Kyle, Alastair, Galina. To the people who helped me without knowing how they did it: David, Monica, Susan, Cesar, Aoife, Uné, Sean (Yui Wai), Marco, Enrique, Alexis, and the old and new friends gained during the course of the work. And finally, thank you for reading this thesis and learning about my work.

Chapter 1

Introduction

For hundreds of years, Humanity has asked itself similar questions: what is the meaning of life? what is right and wrong? who am I? what is time?... From all of these one that has emerged from many different cultures is *what is the Universe?*. The answer for this question has not been unique and has changed as knowledge has advanced.

During history there has been several different ideas and descriptions of the cosmos, the Pythagorean, Atomist, Aristotelian and so on. It should be more correct to call them *models*. Each one of them presented a different cosmic picture, and all of these have been modified, refuted and become obsolete with each new discovery and change of human society.

Therefore, this points out that the idea of the Universe has changed with time, and the existence of *universes* or *universe models* is more appropriate. Hence, cosmology is the study of the cosmos by science, philosophy, theology, and any other subject that seeks understanding. For the purpose of science, cosmology is the study of large and small structures of the *universe models* and how these evolve with time, and the comparison and confrontation of these models with observations.

From the earlier days of mankind several different ideas appeared; one of the most primitive ideas involved a world of magic where everything was surrounded by protecting spirits. Eventually, the cosmic view evolved to myths: it was a new world dominated by gods, demi-gods, and heroes. These ideas faded and were replaced by

the humans as their centre, giving birth to anthropocentricity, which led to the idea of the earth as the centre of the universe. In particular, the Aristotelian model considered several concentric spheres with the earth at the centre. This was the basis for so-called “geocentric models”, and it was the dominant belief for centuries. With this in mind, writers and religion built their world. One of the most known representations is in Dante’s *Divine Comedy* where he guides the reader through out hell, purgatory and paradise conformed of a scheme of concentric spheres, as shown in figure 1.1, similar to the Aristotelian model. Although, the advent of new discoveries and the development of science challenged the old views because all these universes have something in common, they are too complex and there were phenomena that they could not explain at the time of their inception. These inconsistencies were challenged, and consequently, opened the door for new paradigms to enter to the world.

The sixteenth century saw a new change to take place. Until then, the earth was the central axis of the macrocosm, but this geocentric view had become extremely complex in its description of motion for celestial bodies. For this reason, a new idea that simplified and harmoniously explained the skies gained strength and challenged the fundamental belief that had been established for centuries. In brief, the works of Copernicus and Kepler placed the Sun as the protagonist of the picture; the heliocentric model was being born. Not so long later, Galileo raised his telescope to the heavens and saw the moons of Jupiter, suddenly, hammering the last nail in the coffin of the old geocentric ideas. Henceforth, a period of fast changes came for astronomy by the sudden addition of the telescope as an instrument; furthermore, Newton published his laws of motion describing accurately, as never was done before, how gravity interacted. His universal law of gravitation describes that the gravitational attraction between any two bodies varies as the inverse square of their separation [99, 47]; it became one of the cornerstone of the description of the cosmos for the next couple of centuries.

Later in the eighteen century, Thomas Wright described very closely the ring shaped distribution of stars of the galaxy, and the Universe expanded once more; it was not just the solar system any more, but an infinite and static universe. There was a new galactocentric model describing the Milky Way, although, still considering the Sun as

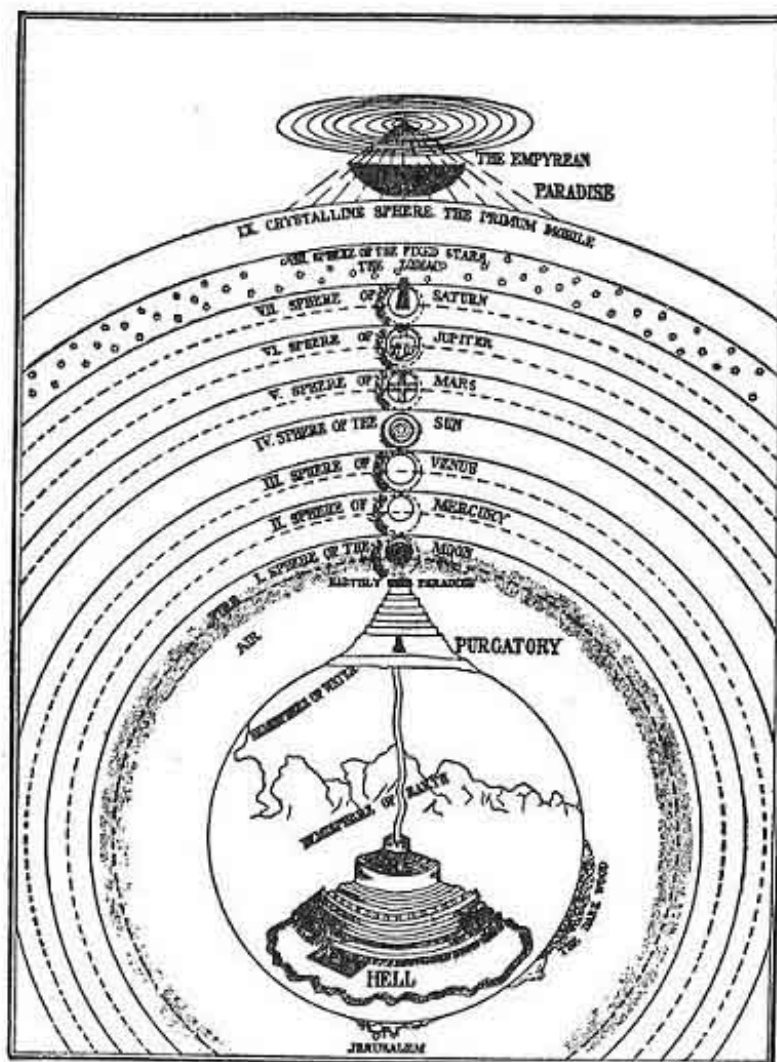


Figure 1.1: Dante's Scheme of the Universe. From *Studies in the History and Method of Science*, ed. by Charles Singer, 1917, Vol. I, Fig. 4.

its centre [47]. This idea was not long lived as the result of the marriage of astronomy and physics.

The speed of light was once thought to be infinite, but Olaus Roemer in 1676 was the first to successfully measure the speed of light. His method was based on observations of the eclipses of the moons of Jupiter. Another famous astronomer who measured light was Edmund Halley obtained a finite speed of 300 000 kilometres a second [47], which initiated an era for more precise measurements of distances. The nineteenth

century saw the birth of astrophysics, which introduced new advances in understanding the composition and motions of stars by taking into consideration Doppler effect (the change of frequency of light due to relative motion between the source and observer), atomic theory, chemical composition, and so on. A new cosmic picture took the scene, the Victorian universe, become the standard cosmological model. It described the universe as a one stand-alone island, the Galaxy, which was surrounded by other small ones. Nonetheless, it did not last much longer after Jan Oort confirmed that the Milky Way stars orbit around a distant centre [47].

In the twentieth century, General Theory of Gravity by Albert Einstein was implemented with success to solve old discrepancies that the Newtonian description of gravity could not. As a result, the modern standard cosmological model was formulated. The magic, old gods and myth had lost out to science for the description of the cosmos.

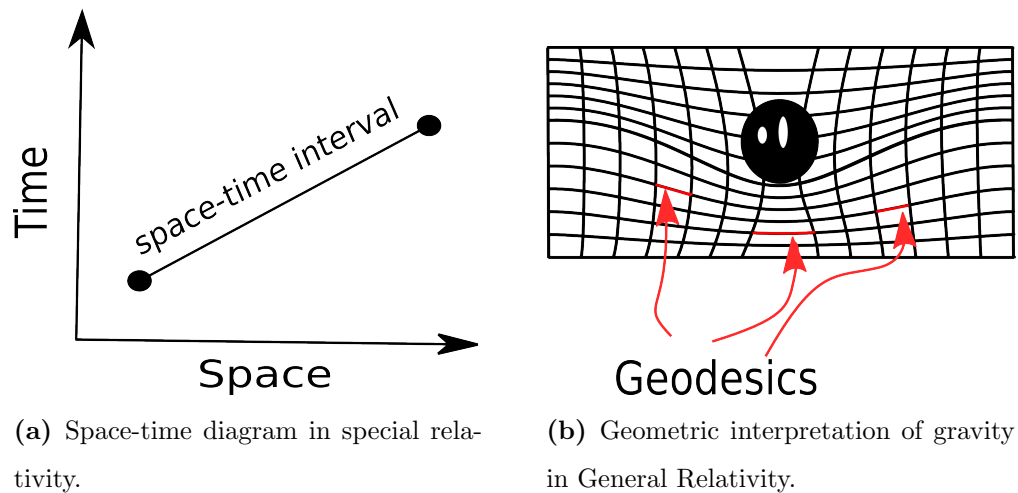
In the rest of the chapter a brief review of modern cosmology will be presented, and will set the basic background for the rest of this thesis. This is by no means an extensive review, and the intention is to only include those topics adequate to help ease the setting for the rest of the work.

1.1 Modern Cosmology

A more appropriate definition of cosmology would be *the study of the primary cosmic constituents, such as the origin and history of chemical elements, and space and time from the frame of an expanding universe* [47]. With this in mind, the following subsection will introduce some views of modern cosmology.

1.1.1 Relativity

The foundations of relativity were introduced at the beginning of the twentieth century by Albert Einstein. Before its formulation, the ideas of space and time were separated concepts, but with the introduction of the Special Theory of Relativity, they combined



(a) Space-time diagram in special relativity.

(b) Geometric interpretation of gravity in General Relativity.

Figure 1.2: a) Shows the simplest idea of space-time in special relativity and the concept of preservation of space-time interval. b) Shows in a simple manner an object with mass curving the space-time. The red arrows point to representation of “shortest paths” which defines the notion of geodesic.

to become a single concept, the space-time [47, 99]. Later on, Einstein expanded its validity by including the effects of gravity in his General Theory of Relativity.

Special Relativity

In Classical Mechanics, the ideas of time and space are considered independent variables, but special relativity combines them as a single space-time, and postulates [104]:

- The laws of physics are the same in every inertial frame.
- The speed of light in the vacuum is constant in every inertial frame,
 $c = 299792458 \text{ m/s}$.

It preserves the notion of inertial frame of reference where a test point mass thrown from the same point in different directions follows rectilinear paths each time it is thrown [52]. The existing distance between two space and time events becomes an invariant, the space-time interval. It extends the notion of a straight line from euclidean geometry. Nevertheless, the effects of gravity are not considered.

Equivalence principle

Special Relativity changed how space and time are described by combining them into a single space-time variable, but it does not consider how gravity affects it. An important property that defines an inertial frame of reference is that any particle at rest remains in this state if no force acts upon it. Nevertheless, trying to define an inertial frame on earth is not easily done because, in general, it is not possible to free particles from the effects of gravity. However, a freely falling frame of reference will satisfy this property, provided that the separation of the particles within it is not too large, and they will remain at rest unless acted upon by some other non-gravitational force. Under those circumstances, gravitational and inertial forces produce effects that are indistinguishable, this is the principle of equivalence [47]. This allowed Special Relativity to be applied in free falling systems as well as inertial frames.

General Relativity

The principle of equivalence allowed to expand the validity of Special Relativity; in combination with the realization that gravity and curved spaces have much in common, this led to the formulation of General Relativity. It is a theory of gravity with curved space where the Newtonian gravitational potential is replaced by the curvature of the geometry of the space-time. In short, it is a geometric interpretation of gravity [104]. Moreover, it generalizes the euclidean idea of “straight lines” to curved spaces; this shortest path is the basic notion of geodesic [104]. In essence, Wheeler described in a simple phrase the main concept of the theory: *Spacetime tells matter how to move; matter tells spacetime how to curve* [136].

The postulates of General Relativity are:

- The laws of physics must be written in the same mathematical form in all coordinated systems.
- Free falling particles follow geodesics of the space-time.

- The equivalence principle or local Lorentz invariance: The laws of Special Relativity apply to all local inertial observers.

The space-time continuum is described by a 4-dimensional manifold with metric g and space-time interval given by

$$ds^2 = g_{\mu\nu} dx^\mu dx^\nu. \quad (1.1)$$

But this is not complete without a relation with “matter” and energy; in this case, the term matter refers to all the forms of energy that have mass [47, 99]. This information is encapsulated in what is called the energy-momentum tensor, $T_{\mu\nu}$, and it is very important; doing an analogy with Newtonian theory, it is the equivalent to the mass density field ρ . For Einstein’s relativity the source of the gravitational field is the Energy-momentum tensor. Furthermore, the description of the gravitational interaction of matter in terms of the space-time curvature is given by the Einstein field equations [104, 99, 47],

$$G_{\mu\nu} = \frac{8\pi G}{c^4} T_{\mu\nu}. \quad (1.2)$$

1.1.2 The early universe

With the introduction of General Relativity, a new paradigm of the universe had to be developed. Its study led to the derivation that the cosmos had a beginning, and in the present, it should be expanding. This new model is known as the Big Bang model [47, 99, 60].

Before the introduction of the Big Bang model, the most dominant description was a static Newtonian universe; it was not expanding nor contracting. But according to General Relativity a static universe, finite or infinite, would only be achieved by a set of strict rules [47, 58]. It was the works of Alexander Friedmann, George Lemaitre, Arthur Eddington, Edwin Hubble, and other pioneers in the decade of 1920s that made an expanding universe a familiar idea [47, 58, 99].

The cosmic horizon

After the original publication, Einstein corrected his field equations to maintain the description of the universe as static, which is known today as the cosmological constant; however, this correction was proven to be wrong, by the evidence in the measurements of the recession velocity of galaxies of Edwin Hubble [47, 66, 99]. He used the concept of redshift, which is defined as the fractional increase in wavelength of a source:

$$z = \frac{\lambda_0 - \lambda}{\lambda}. \quad (1.3)$$

Here, λ_0 is the observed wavelength and λ is the emitted wavelength. Hubble used the relative velocities of galaxies with redshift given by the relation $V = cz$. Where V is the relative velocity and c being the speed of light. He found that the previous relation increased and was proportional with the galaxy distance. Generally speaking, it was the sign that the observable universe was expanding [47, 99, 66]. Then later a redshift-distance relation was derived, called the Hubble's Law,

$$V = HD. \quad (1.4)$$

V is the velocity, D is the distance, and H is called the Hubble term or parameter. This term changes in time, and will be discussed in later sections [47]. The measurement of a cosmic expansion set to rest the static universe. But if the universe expands, this meant that there was a beginning; therefore, the universe was finite in time and space.

When the speed of light, in the vacuum, was found to be a precise and fixed value, it transformed telescopes into time machines [66]. Light from distant stars observed in the night sky took a specific amount of time to reach observers on Earth; the introduction of a finite expanding universe created a barrier or cosmic horizon. The travel time of any light emitted in the distant past could not exceed the age of the universe, and due to the expansion it creates a region which expands with time known as the observable universe [60]. Anything that we are able to see today is inside this region. As time passes, more light from distant objects will arrive eventually. Nevertheless, as it has been found galaxies recede from each other due to the expansion, this affects the light

emitted, which produces redshift, if this recession is enough to equal the speed of light, any object satisfying this condition will remain hidden from us [47].

Before the first second

As mentioned earlier, the Big Bang model predicts a finite, expanding universe. This means that some time in the past there was a beginning. There is not an agreement of what happened during this time, but it was a time where the universe was extremely hot and dense with an average temperature of approximately 10^{32} Kelvin; quantum fluctuations plagued the whole universe [47, 58, 67]. At some point after about 10^{-36} second, it is believed that an abrupt and violent expansion of the universe happened, this is called inflation [68]. This allowed the universe to cool down and start forming the basic components needed for the formation of basic elementary particles, and the small fluctuations were enhanced with this abrupt change on size creating tiny but, with time, considerable irregularities. A slower expansion continued, and after the first second the temperature of the universe was approximately 10 billion kelvin and the density was 1 million gram per centimetre cubic dense [47].

First million years

The universe was a soup of particles for a while, and around 3 minutes of age, the first atomic nuclei was formed; the process is called Big Bang Nucleosynthesis. It was the time where the majority of the Hydrogen and Helium nuclei were formed. This era of cosmic history is called the radiation era, and lasted for approximately 100 000 years. In other words, the dominant component of the universe was radiation. Nevertheless, this would not last, as time passed the continuous expansion kept cooling the content and changing the densities. Therefore, it reached a point where the density of matter and radiation were equal [68]. As the expansion continued, matter started to become dominant. Even more, by the time the temperature dropped below 4000 Kelvin marked the start of the recombination epoch. During this epoch, the energy of the photons had dropped enough so that atomic nuclei and electrons could combine to

form neutral atoms, this process is referred as recombination. Before this, photons had enough energy to easily ionize any bound atom; this released a flood of electrons that previously kept constantly scattering in all directions impeding light from travelling long distances and maintaining the state of the universe as a plasma for approximately 300 000 years [66, 99]. Moreover, it started a process of decoupling with radiation. Photons were no longer able to ionize the neutral atoms which in turn allowed them to travel free through space; this was a slow process which lasted for more than 10 000 years and left an energetic imprint, this time of the early universe is known as the epoch of last scattering. Light from this fingerprint of the early universe was able to travel free from the young epochs, and we receive it in the present as what is known as the Cosmic Microwave Background Radiation (CMBR) [58, 99, 66, 67]. Eventually, freeing light to travel and the dominance of matter made the universe transparent; furthermore, at this point there was no stars to cover the sky, therefore, it started an cosmic period appropriately designated as dark ages [47, 66, 99].

Fourteen billion years later

After the epoch of decoupling and last scattering, the universe spent millions of years in darkness, and little or nothing is known about this era [47]. It was a time dominated by matter, but finally to end this epoch, at around 400 million years of age, the first stars was born. It was a time full of gas, mainly hydrogen and helium, but the density was a million times greater than what it is today, and this caused the stars formed at this point to be considerably bigger and short-lived compared to their modern counterparts. Their death, as the most accepted process [67], was the engine that started the formation of galaxies. It triggered the birth and death of countless stars with new galaxies being form. It was a very active period of the universe, and lasted for millions of years. At some point during this active time, matter lost dominance, and a component designated now as Dark Energy took the lead and started driving the expansion of the universe. Its composition is still unknown and being study, but for the Big Bang model it is represented by the cosmological constant. From galaxies, the continuous creation and

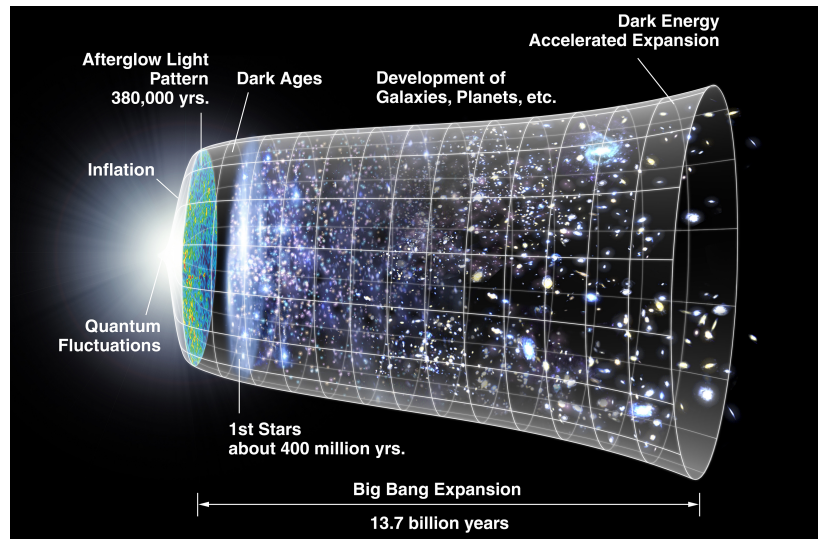


Figure 1.3: Impression of the evolution of the universe according to the hot Big Bang model by NASA/WMAP Science Team (Original version: NASA; modified by Ryan Kaldari) [Public domain], via Wikimedia Commons.

destruction of stars led to the formation of heavier elements, and new bounded objects like asteroids, planets, and so on. This process continues after almost fourteen billion years, and it is now being observed by telescopes on Earth.

As an illustration, the process of the history of the universe is presented in a representative manner in fig. 1.3.

1.2 Standard model of cosmology

1.2.1 Homogeneity and isotropy

The starting point in modern cosmology, and key component of the so-called Big Bang model is the Cosmological Principle [58, 99, 47, 66, 88]. This says that on large scales the universe is homogeneous and isotropic. This was presented originally as an intuitive property to reduce the mathematical analysis. The homogeneity of the universe can be observed on scales around 100 Mpc ($1 \text{ Mpc} \simeq 3.08 \times 10^{22} \text{ m}$) [79, 58, 99]. Below this scale the universe is observed to be lumpy due to the distribution of galaxies, clusters

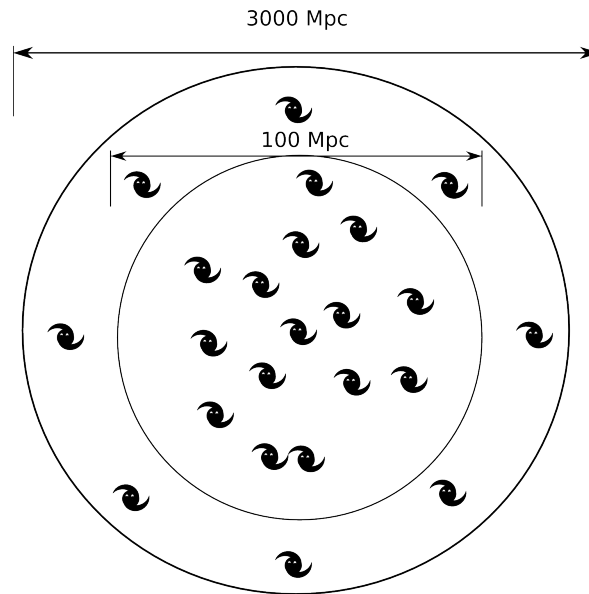


Figure 1.4: A simple sketch exemplifying the homogeneity at larger scales. Below 100 Mpc, the galactic distributions seems lumpy. Above this, the distribution becomes regular the universe seems homogeneous up to the limit of the observable universe.

and super-clusters. Nevertheless, this homogeneity is just observed to the maximum distance possible, the observable universe, around 3000 Mpc; this is sketched in fig. 1.4. This does not mean that the whole universe is in the same way. The best evidence for the cosmological principle comes from the Cosmic Microwave Background Radiation (CMBR), where it can be seen that there is high uniformity in the temperature, hence the density, of the early universe in all directions, as seen in Fig.1.5. If no homogeneity or isotropy were present, there would be different temperatures and bigger anisotropies at actual times. The uniformity of the CMBR suggests that at the epoch of last scattering, around 300,000 years after the Big Bang, the universe was very smooth. This raises the question about the local environment where it is possible to see significant anisotropy - i.e. what portion of the universe is similar to ours?. Without speculation, it is possible to use the evidence that the universe is homogeneous and isotropic at scales beyond 100 Mpc with well developed structures below this range. The expansion of the universe according to Hubble's law and the CMBR show a possible way for how the small fluctuations could grow. [66, 58, 88, 67, 99, 79]

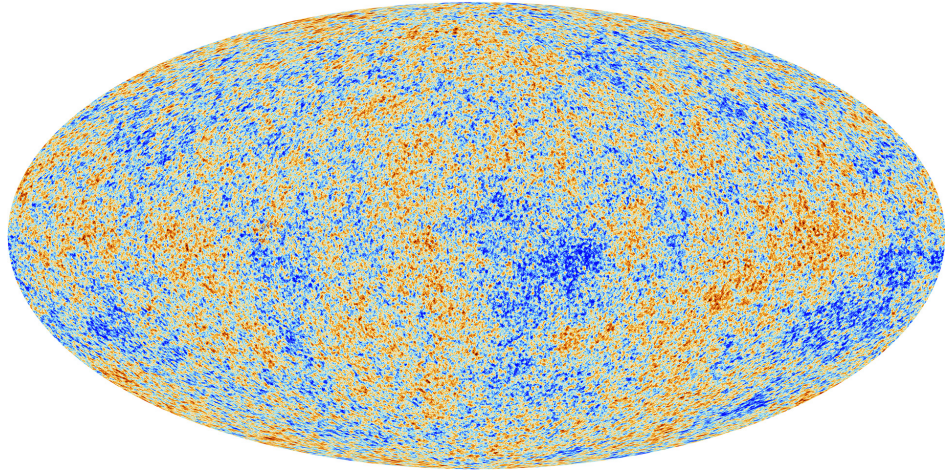


Figure 1.5: An all-sky map of temperatures from Planck mission of the CMBR [94]. Red and blue colours indicate warmer and cooler fluctuations with respect the mean temperature of 2.72 kelvin. These are extremely dim variations as they are just one part in 100,000. By ESA and the Planck Collaboration.

FRW Metric

General Relativity allows to describe matter moving at relativistic velocities or random pressures, and we know that radiation dominated the universe for the first 100 000 years after the Big Bang, but to understand other important epochs in the cosmic history, it is necessary to work with a complete relativistic theory.

The metric for a space-time with homogeneous and isotropic spatial sections is the maximally-symmetric Friedmann-Robertson-Walker (FRW), which can be written in the form [58, 79],

$$ds^2 = dt^2 - a^2(t) \left\{ \frac{dr^2}{1 - kr^2} + r^2 d\theta^2 + r^2 \sin^2 \theta d\phi^2 \right\}, \quad (1.5)$$

where (t, r, θ, ϕ) are the comoving coordinates, as perceived by an observer who is moving along with the expansion of the universes with a cosmic scale factor $a(t)$. As a convention eq. (1.5) is written considering natural units, this means $c = G = 1$. With appropriate choice of coordinates, k can be +1, -1 or 0. This describes the spatial curvature with positive, negative and zero respectively. The coordinate r in (1.5) do not have dimensions.

It is convenient to express the FRW metric in terms of τ or η , and defined by $d\tau = dt/a(t)$:

$$ds^2 = a^2(\tau) \left\{ d\tau^2 - \frac{dr^2}{1 - kr^2} - r^2 d\theta^2 - r^2 \sin^2 \theta d\phi^2 \right\}. \quad (1.6)$$

With this choice of coordinates, the metric can be written as a Minkowski line element with a conformal factor, $a(\tau)$, the scale factor in terms of the conformal time.

1.2.2 Friedmann Equation

In cosmology the most important equation describes the expansion of the universe according to its material content; this is the Friedmann equation. The standard way to state the equation by considering a universe with zero cosmological constant is [58],

$$H(t)^2 = \frac{8\pi G\rho(t)}{3} - \frac{kc^2}{a(t)^2}, \quad (1.7)$$

$a(t)$ is the scale factor of the universe, which describes the time dependence of the cosmic expansion. $H(t) = \dot{a}/a$ is the Hubble parameter and describes the rate of change of the expansion. $\rho(t)$ is the energy density of content of the universe, G is Newton's gravitational constant, c is the speed of light and k is the curvature of the universe.

In a universe with a FRW metric, it is possible to define a critical parameter, the value of which will determine the expansion or contraction in the future of the universe. This is the critical density, and it is defined by setting a flat universe ($k = 0$) in the Friedmann equation,

$$\rho_c(t) \equiv \frac{3c^2}{8\pi G} H(t)^2. \quad (1.8)$$

Any value of the density greater than this will produce a positively curved universe, and on the contrary values below it will produce a negatively curved universe. It is more convenient to work in terms relative to this critical density by defining a dimensionless density parameter

$$\Omega(t) \equiv \frac{\rho(t)}{\rho_c(t)}. \quad (1.9)$$

Ω_0 is defined as the value of this parameter in the present time, and it can be constrained from observations. The most conservative limits establish this parameter must lie in the range $0.1 < \Omega_0 < 2$ [99].

1.2.3 Λ CDM

The standard model in cosmology, which best fits the observational data while using as few free parameters as possible, is called Λ CDM. It is common to represent the parameters in terms of the dimensionless density parameter instead of the energy density. Therefore, the components of the Λ CDM are commonly presented in the Friedman equation in the following form [99].

$$H(a) = H_0 \sqrt{\Omega_m a^{-3} + \Omega_r a^{-4} + \Omega_\Lambda}. \quad (1.10)$$

Here $H(a)$ is the Hubble parameter in terms of the scale factor and H_0 is the Hubble constant at the present time. Ω_m , Ω_r , Ω_Λ are the dimensionless density parameters for matter, radiation and Dark Energy respectively.

In the model radiation is composed of relativistic particles, and the biggest constituents are photons and neutrinos, but they make less than 0.01% of the present-day content of the universe. Matter consist of two major groups, ordinary and Dark Matter; they constitute 4.86% and 25.89% content of the universe. In cosmology, it is common to refer to ordinary matter as baryonic matter. The term is used loosely to refer to any kind of matter made of atoms. This is due to the fact that the atomic nuclei, made of protons and neutrons which are baryons, represents the major mass percentage of the atom. Dark Matter is described as Cold Dark Matter.

The majority of the density of the universe is Dark Energy which represents 69.11% [93] and is described by the cosmological constant Λ . An illustrative pie chart of these proportions is in fig. 1.6.

The Hubble constant at the present time, H_0 , has been obtained by different techniques like gravitational lensing [19], Type Ia supernovae [31] and more recently gravitational waves [2]; nevertheless the most accepted value comes from the CMBR

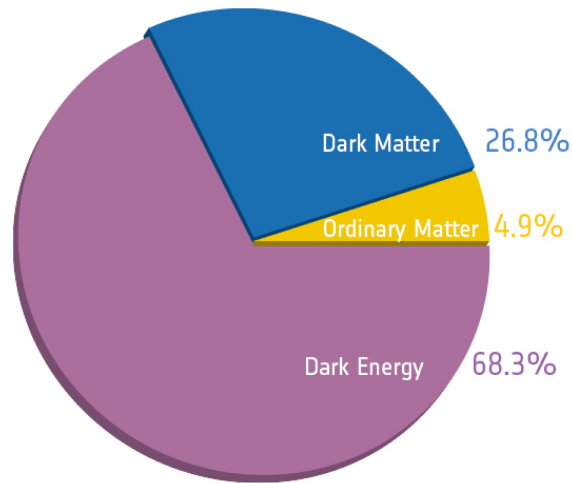


Figure 1.6: The relative amounts of the different constituents of the Universe. Image credit: ESA/Planck.

observations and has been measured to be $67.74 \pm 0.46 \text{ km}^{-1}\text{s}^{-1}\text{Mpc}^{-1}$ [94]. Furthermore, this value can be used to obtain a rough estimate to the scale for the age of the universe as,

$$t_{age} = 1/H_0 \approx 13.799 \pm 0.021 \times 10^9 \text{ years}. \quad (1.11)$$

A proper calculation needs to take into account the different epochs of the universe. For the purpose of this work, this value would be enough, and the important component will be the Dark Matter.

1.2.4 Dark Matter

It is accepted now in the standard model of cosmology that the universe is not comprised entirely by Baryonic Matter, but in contrast the main component of the material content of the universe is in the form of an elusive type of matter which only manifests itself by its gravitational interaction, which means it has weak interaction with the electromagnetic radiation, and hence light. In this fashion, it is appropriately named Dark Matter (DM). Indirect evidence can be traced back to the 1930s with the observation of the large velocity from the members of the Coma cluster [140, 113].

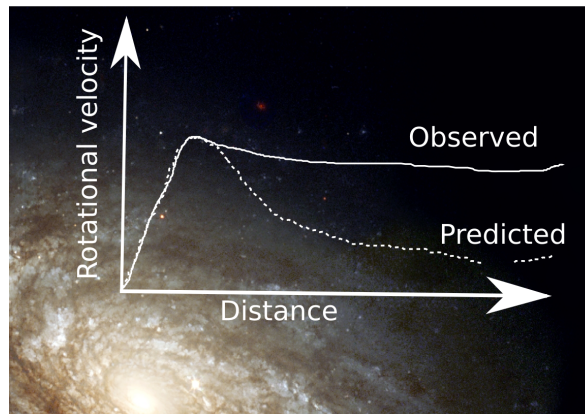


Figure 1.7: Representation of the observed comparison between the predicted rotation derived from Kepler’s Law and the observed velocity curves of galaxies.

It was observed that there was a great discrepancy between average mass of the galaxies obtained from the cluster observations and that derived from their rotation. This discrepancy was confirmed at the time by three independent detections [95, 140, 113, 15]. It took several years to accept the fact that the luminous mass was not the cause of these effects, and now the rotation curves of galaxies offer the most common observational evidence about the inferred existence of Dark Matter. If Individual stars were orbiting around galaxies following Kepler’s law, then beyond the visible part of the galaxy the rotational velocity should drop off as the square root of the star’s distance from its centre. However, the rotation velocity has been observed to remain approximately constant at large distance from the centre of galaxies. Figure 1.7 sketches this feature of observations. This observation implies that there is more mass that cannot be seen enveloping galaxies. This is what is called the galactic halo. It could be composed by matter which is too faint to be observed, like planets or black holes, or the evasive component of Dark Matter. The latter would then comprise a Dark Matter halo. For the purpose of the rest of this thesis when referring to the halo, it would be implied to be the Dark Matter halo [66, 58, 17, 56, 99, 3]. The Λ CDM model describes the dark matter as a particle weakly interacting with the electromagnetic force and massive enough, so it is slow compared to the speed of light, hence the cold part of the name. Nevertheless, as successful as the model has been it has had several problems

at the galactic level. The most common are [56, 16, 62, 63, 10, 29, 16, 89, 3] :

- Numerical simulations give much more satellite galaxies than observed, this is known as the missing satellite problem.
- The model predicts a cuspy central density in the halos while observations show that halos have approximately constant central densities. This is known as the cusp/core problem.
- Simulations predict Milky way subhalos, subset of halos within the larger galaxy halo, are massive enough so that they should not be able to host any of the bright satellites, but observations show that these have less dark matter than expected. This is the too big to fail problem.

It is now accepted that Dark Matter is a component of the universe, but still there is no agreement of the composition of such type of matter because it has not been directly detected yet. There are several proposals for the composition of Dark Matter and the most popular is Dark Matter being composed of Weakly Interactive Massive Particles (WIMPS) which might be a super-symmetric extension for the Standard Model of particles [45]. Primordial Black Holes is other possible candidate [24], but in particular the main focus of the thesis will be in a model described as Scalar Field Dark Matter (SFDM), which will be briefly introduced in the following section.

1.3 Scalar Field Dark Matter

The standard particle interaction for the conventional Cold Dark Matter interpretation still lacks laboratory support or observational evidence from e.g. dwarf galaxies. With this and other problems in mind [69, 56, 16], the use of bosonic fields, and especially scalar fields, is justified considering that these have the ability to mimic the behaviour of matter [129]. The SFDM model assumes that the dark matter is a scalar field of nature [72, 76, 77, 74]. The idea came around the 1980s with the proposal of the axion as candidate for the dark matter particle [129]. It was shown how an oscillating

homogeneous scalar field could mimic the behaviour of matter. During the following decade it was proposed the composition of the dark matter as a scalar field, similar to the introduction of the inflaton scalar field in the inflationary cosmological model [23]. During the following decade there were only a few groups working on this idea, but the lack of communication among them caused the model to receive several names, such as Bose-Einstein Condensate Dark Matter (BEC DM), scalar field Dark Matter (SFDM), fuzzy Dark Matter (FDM), ultra-light axion (ULA), Wave Dark Matter (WaveDM), ψ DM among others [62, 63]. For the rest of the work it will be referred in general as SFDM, unless specified otherwise.

The attractiveness of the SFDM models is that they have only one free parameter important for the theory, the mass of the scalar field. It has been calculated by comparing the de Broglie wavelength of DM to the typical galaxy size that this mass needs to be ultralight ($m \sim 10^{-22}$ eV) [118, 63]. With only this feature constrained, the SFDM model is able to produce:

1. The evolution of the cosmological densities in a similar manner to the standard Λ CDM model [75, 73].
2. The acoustic peaks of the CMBR [75].
3. The existence of a natural cut-off, which helps to agree with the scale of sub-structure seen by the observations of large scale structure [73].

Therefore, it can be seen why it is important to obtain techniques that allow to constraint the mass of the scalar field. This remarks the use of observations and different viable tools to give an insight about this vital property in the formulation of the model.

To point out, the tool selected for the purpose of exploring the constraints on the mass of the scalar field, regarded in the work as the axion mass, m_a , during the course of this work will be gravitational lensing, which will be introduced in the next chapter.

To address and emphasize the viability of the SFDM model as an alternative to the standard cosmological model, it should be able to adequately reproduce the successful results of CDM. For this reason, studying the behaviour of SFDM through gravitational

lensing gives insight on the requirements that it should fulfil, and likewise, study its own properties.

Chapter 2

Gravitational lensing

2.1 The bending of light

General Relativity describe how particles travel on geodesics, and this applies also to photons. Because of this effect, a ray of light passing close to a massive object is deflected from its original trajectory. To attain a notion of this, it is easier to describe the effect starting in the sense of Special Relativity.

In Special Relativity, the line element, ds , of a point particle moving along the x axis is given by [104]

$$ds^2 = c^2 dt^2 - dx^2. \quad (2.1)$$

If this particle is a photon, one of the postulates Relativity is the constancy of the speed of light, c . For this to be satisfied, the only line element a photon can take is $ds = 0$, reducing to

$$cdt = dx. \quad (2.2)$$

Therefore, light travels in a straight line. In this example, the space in consideration is flat which corresponds to a Euclidean geometry. The idea can be generalized to a curved space and be represented in General Relativity. Specifically, the light path defines the null geodesic. The expression in (2.2) for a curved space is obtained from eq. (1.1) as

$$g_{\mu\nu} dx^\mu dx^\nu = 0. \quad (2.3)$$

Solution of this equation requires knowledge of the metric, $g_{\mu\nu}$. In summary, light travels along the curvature of the space-time caused by matter, albeit, it does it without modifying the path. In the event a region is sufficiently flat, the results from Special Relativity are recovered.

For a spherically symmetric object describing a compact lens in an isolated region of space-time containing no other matter, the line element is the Schwarzschild metric. Furthermore, any ray of incident light towards and passing by the lens will be contained in the same plane defined by the mass location due to the spherical symmetry; therefore, it is useful to work in convenient coordinates, which in this case is done by choosing the plane defined by $\theta = \pi/2$. The line element is given by [78]

$$ds^2 = \left(1 - \frac{2MG}{rc^2}\right) c^2 dt^2 - \left(1 - \frac{2MG}{rc^2}\right)^{-1} dr^2 - r^2 d\phi^2. \quad (2.4)$$

This could be separated in radial and angular parts. The presence of the mass will curve the space surrounding it. For any light ray travelling close by, it will follow the curvature. Specifically, there will be a distance where the path will bend and allow the light continue travelling without colliding with the massive object; in other words, the ray will only be deflected. Considering the Schwarzschild metric, the deflection angle produced is given by [78]

$$\hat{\alpha} = \frac{4GM}{\xi c^2}, \quad (2.5)$$

where ξ is the radial distance from the closest point of the light path to the massive object; it is also known as the impact parameter [102].

2.2 Lens equation

Consider a massive object with a total mass, M , close to the line of sight to a source S . The angle β describes the unobservable angle between the line of sight to the actual object and the optical axis. The observed angle θ , which is the apparent angle to the source image I from the optical axis, is shown in figure 2.1. Due to the gravitational effect the ray of light is bent by the angle $\hat{\alpha}$. Considering that we observe the image I ,

the magnitude of the difference with the source position as shown in fig. 2.1 and the relation with the deflection angle is given by

$$I - \eta = D_{OS} \tan \theta - D_{OS} \tan \beta = D \frac{\sin \hat{\alpha}}{\cos \beta}, \quad (2.6)$$

where D is radial distance from the source to the deflection position given by ξ . The geometry expressed as this becomes complicated enough, but considering the distances involved in the effect, we can assume small deflections and the thin lens approximation can be used for the deflector; this makes possible to apply the small angle approximation to (2.6), which at the same time allows to approximate $D \approx D_{LS}$. The equation is rewritten in a simpler form as

$$\theta D_{OS} = \beta D_{OS} + \hat{\alpha} D_{LS}. \quad (2.7)$$

Introducing the reduced deflection angle

$$\alpha \equiv \hat{\alpha} \frac{D_{LS}}{D_{OS}}, \quad (2.8)$$

it is possible to define the so-called lens equation

$$\beta = \theta - \alpha. \quad (2.9)$$

This equation relates the observed and the actual position of the source. This equation holds true as long the distances, D_A , are sufficiently large compared with the individual sizes of source, lens and observer.

2.2.1 Point like lens

The simplest solution for the lens equation is the case when we have a ray of light being deflected by a point like mass, M . Using the derived deflection angle for a point mass from Eq. 2.5 and considering the radial distance $\xi = \theta D_{OL}$, the reduced deflection angle is given by

$$\alpha = \frac{D_{LS}}{D_{OS} D_{OL}} \frac{4GM}{\theta c^2}. \quad (2.10)$$

For this case, the equation can be solved analytically. Another key point is the angle subtended when the source and the lens are aligned, $\beta = 0$, which is a special case

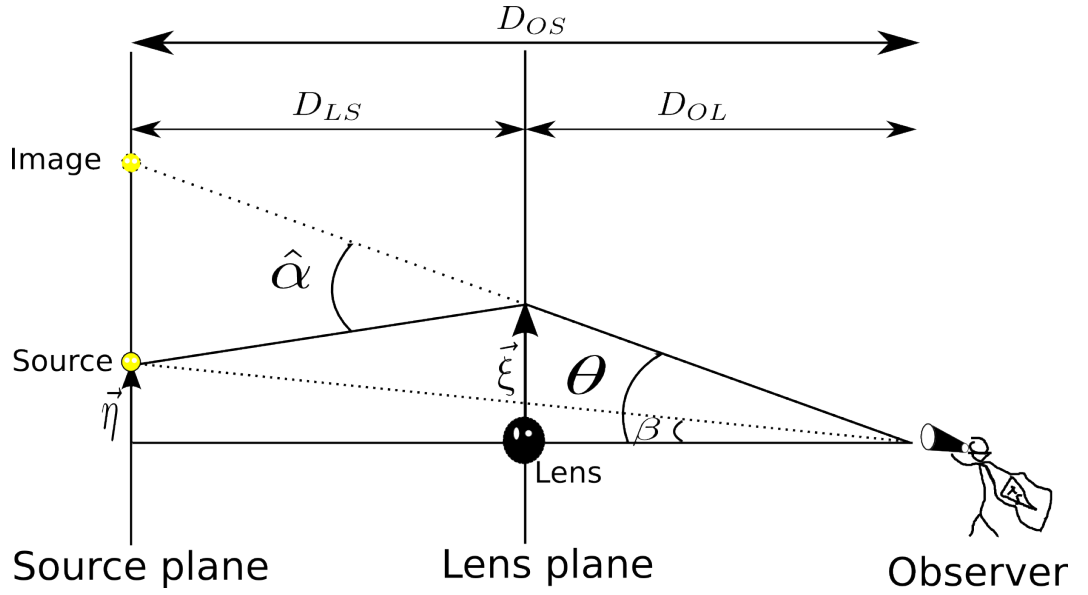


Figure 2.1: Diagram showing the light path from the source to the observer, deflected by a mass in the lens plane. The diagram shows a point-like lens, but a similar diagram can be used to represent light deflection by a symmetric extended distribution.

where the image forms a ring with an angular radius called the Einstein angle and commonly labelled as θ_E [78, 103]. In the case of the point like mass it is defined as

$$\theta_E = \sqrt{\frac{D_{LS}}{D_{OS}D_{OL}} \frac{4GM}{c^2}}. \quad (2.11)$$

The solution for a generic non-aligned source position, defined by angle β , generates two images with angular positions [78, 102]

$$\theta_{\pm} = \frac{\beta}{2} \pm \theta_E \sqrt{1 + \frac{\beta^2}{4\theta_E^2}}. \quad (2.12)$$

2.3 Time Delay

The time delay due to gravitational lensing arises from the difference in arrival time at the observer of light from the images, compared with the light travel time from the source in the absence of a lens. First the light deflection causes the light to travel along a different path, introducing geometrical time delay. For example, in eq. (2.12) by assuming θ_E and β positive, the θ_+ solution produces a bigger angle than θ_- , therefore,

the resulting distance to the observer is different; in general, the positive solution has the shortest travelling path. Moreover, because the light traverses the gravitational field of the lens, we can expect there to be another factor contributing to the time delay. This is known as the Shapiro delay [102].

Given the weak field metric, in the time coordinate and considering a Euclidean length dl ,

$$cdt \approx (1 - 2\Phi)dl, \quad (2.13)$$

where Φ denotes the Newtonian gravitational potential of the lens. Thus, not only is there a time delay due to the path difference but there is also a time delay due to the gravitational potential.

2.3.1 Lensing Potential and Fermat potential

We can describe the bending of light in terms of a lensing potential, which is related to the Newtonian potential with proper rescaling by [102]

$$\hat{\psi}(\boldsymbol{\xi}) = \frac{D_{LS}}{D_{OL}D_{OS}} \frac{2}{c^2} \int \Phi(\boldsymbol{\xi}, z) dz, \quad (2.14)$$

and it follows that the lensing potential is related to the bending angle by the equation

$$\nabla_x \hat{\psi} = \alpha. \quad (2.15)$$

2.3.2 Caustics and critical curves

The light deflection produced by the gravitational field is the reason for the gravitational lensing effect, and it is not connected to a process of absorption or emission of light. This means that the intensity of radiation produced by the source must be conserved as the light travels to the observer. Furthermore, considering the deflector is relatively static in the system, the surface brightness produced by the source remains constant.

The flux from an infinitesimal source is the product of the solid angle, $\Delta\omega$, and the surface brightness which varies along the light path. Therefore, by comparing the

lensed and unlensed fluxes, we can write a simple relation between both cases; given the conservation of surface brightness, the relation only depends on the solid angle. This comparison defines the magnification factor which is given by [102]

$$\mu \equiv \frac{\Delta\omega}{(\Delta\omega)_0}, \quad (2.16)$$

where $(\Delta\omega)_0$ corresponds to the solid angle for the unlensed case. In terms of the mapping between θ and β in eq. (2.9), the magnification factor for light is

$$\mu = \left\| \det \frac{\partial \beta}{\partial \theta} \right\|^{-1}. \quad (2.17)$$

This equation is the ratio of the flux of an image in the lensed versus the unlensed case [103]. Additionally, it is important to consider the particular case when the determinant vanishes. This condition sets a line known as a critical curve [78]. Along this curve the amplification diverges, but this is not a real feature from a finite source, but more a result from the approximation used to describe the lens, the geometrical optics, which is generally adequate for the treatment of light [102]. At the same time, the corresponding positions of the source which produce this critical curve are called the caustics [78, 102]. They are of interest because they define the divergence of the amplification factor, and can be traced through the mapping of the lens equation.

2.4 Extended mass distribution

The previous considerations are for a point-like mass distribution, but real objects are extended mass distributions with a density $\rho(\mathbf{x})$. In view of the distances considered which are much larger than the size of the deflector, it is adequate to use the so-called thin lens approximation, where the thickness of the lens is ignored by assuming that it has a much smaller physical length compared with the observer-to-lens and source-to-lens distances.

The surface mass density, $\Sigma(\boldsymbol{\xi})$, corresponds to the projection of the mass distribution on a plane passing through its centre of mass and orthogonal to the light ray

direction [78]. This is defined as

$$\Sigma(\boldsymbol{\xi}) = \int \rho(\boldsymbol{\xi}, z) dz. \quad (2.18)$$

The particular case which simplifies the calculations is when the mass distribution is spherically symmetric. In this case the surface mass density only depends on the modulus of the impact parameter $\xi = |\boldsymbol{\xi}|$. For this purpose, the deflection angle is

$$\hat{\alpha} = \frac{4GM(\xi)}{c^2\xi}, \quad (2.19)$$

with $M(\xi)$ as the mass enclosed inside a circle of radius ξ in the projected plane,

$$M(\xi) \equiv 2\pi \int_0^\xi d\xi' \xi' \Sigma(\xi'). \quad (2.20)$$

This is also called the reduced mass. Furthermore, by taking into consideration an extended distribution, the lens equation can be rewritten as

$$\beta = \theta - \frac{M(\theta)}{\pi D_{OL}^2 \theta \Sigma_{cr}}. \quad (2.21)$$

where $\Sigma_{cr} = c^2 D_{OS} / 4\pi G D_{OL} D_{LS}$, and it is called the critical surface density. In addition, disregarding the form of the mass distribution, the total mass enclosed inside the Einstein angle can always be obtained as

$$M(\theta_E) = \pi D_{OL}^2 \theta_E^2 \Sigma_{cr}. \quad (2.22)$$

2.5 Most common lensing profiles

2.5.1 SIS profile

Among the different symmetric mass distribution models for galaxies acting as a lens, the simplest and most widely used to reproduce the flat rotation curves is the Singular Isothermal Sphere (SIS) [17, 102, 78]. Here the profile is given by

$$\rho(r) = \frac{\sigma^2}{2\pi G r^2}. \quad (2.23)$$

The value of σ is the one dimensional velocity dispersion of stars orbiting around a gravitational bounded object such as a galaxy or a cluster. Equation (2.23) can be used as the profile in (2.18) and integrated analytically to obtain the surface mass density,

$$\Sigma(\xi) = \frac{\sigma^2}{2G\xi}. \quad (2.24)$$

From it, the reduced mass as expressed by eq. (2.20) is easily found by integration which gives

$$M(\xi) = \frac{\pi\sigma^2}{G}\xi. \quad (2.25)$$

The SIS is the simplest example for an extended mass distribution. Unfortunately, the density grows following the inverse square law, and it has a singularity at the centre of the distribution.

2.5.2 NFW profile

The standard paradigm of Dark Matter describes it as collisionless and cold, so this predicts a general structure from which there can be expected to exist a universal profile for the evolution of galaxies [83]. The most general profile to describe the mass distribution of galaxies dominated by Dark Matter is the Navarro, Frenk and White (NFW) profile [138, 90, 83]. The mathematical form of the profile is given by

$$\rho_{NFW}(r) = \frac{\rho_s}{r/r_s(1+r/r_s)^2}, \quad (2.26)$$

where ρ_s is the central density, and r_s is the characteristic scale radius of the profile.

The NFW profile suffers from a singularity at the centre. From (2.18), the surface mass density of an NFW lens is written as

$$\Sigma_{NFW}(x) = \begin{cases} \frac{2r_s\rho_s}{x^2-1} \left[1 - \frac{2}{\sqrt{1-x^2}} \operatorname{arctanh} \sqrt{\frac{1-x}{1+x}} \right], & x < 1, \\ \frac{2r_s\rho_s}{3}, & x = 1, \\ \frac{2r_s\rho_s}{x^2-1} \left[1 - \frac{2}{\sqrt{x^2-1}} \operatorname{arctan} \sqrt{\frac{x-1}{1+x}} \right], & x > 1, \end{cases} \quad (2.27)$$

considering the profile spherically symmetric, $x = \xi/r_s$ [7, 138]. The reduced mass of

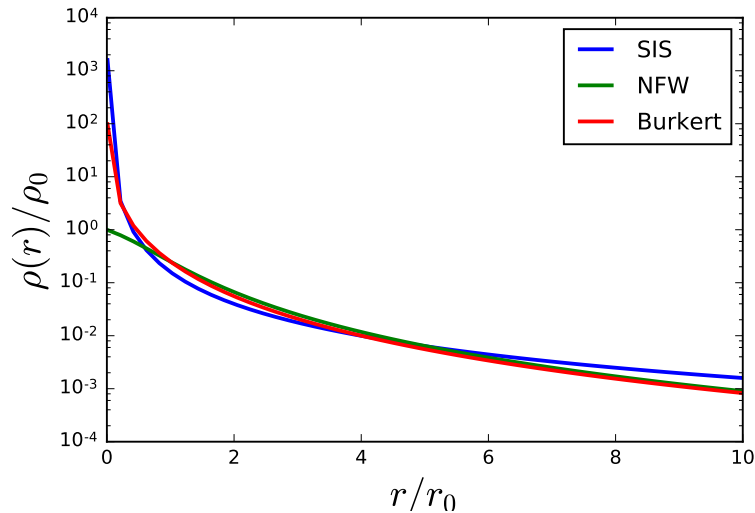


Figure 2.2: Comparison of the three example profiles by a central density, ρ_0 and normalization length, r_0 . For the case of the SIS, it was defined $\rho_0 = \sigma^2/Gr_0^2$. For NFW and Burkert profiles $r_0 = r_s$. It is clear that the SIS and NFW profiles diverge at the centre, meanwhile the Burkert and NFW are similar at large radii.

the lens is given by

$$M_{\text{NFW}}(x) = 4\pi r_s \rho_s \begin{cases} \left[\frac{2}{\sqrt{1-x^2}} \operatorname{arctanh} \sqrt{\frac{1-x}{1+x}} + \ln\left(\frac{x}{2}\right) \right], & x < 1, \\ \left[1 + \ln\left(\frac{1}{2}\right) \right], & x = 1, \\ \left[\frac{2}{\sqrt{x^2-1}} \operatorname{arctan} \sqrt{\frac{x-1}{1+x}} + \ln\left(\frac{x}{2}\right) \right], & x > 1, \end{cases} \quad (2.28)$$

where x was previously described [138]. A comparison of the profiles using similar central densities and normalization radius is seen in fig. 2.2.

2.5.3 Burkert profile

The previously considered profiles, while popular and precise for large radii, suffer from singularities closer to the centre of the mass distribution. There are several profiles which try to address this by having a density core. One of these is the Burkert profile, given by

$$\rho(r) = \frac{\rho_s}{(1 + r/r_s)(1 + (r/r_s)^2)}, \quad (2.29)$$

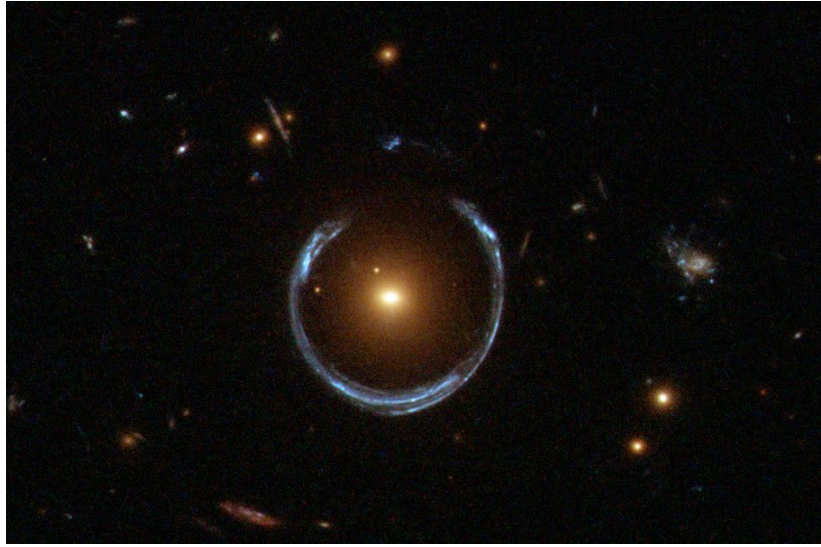


Figure 2.3: Example of strong lensing. A luminous red galaxy distorting a more distant blue galaxy. By ESA/Hubble & NASA derivative work: Bulwersator via Wikimedia Commons.

where ρ_s and r_s are the free parameters that represent the central Dark Matter density and the characteristic scale radius respectively. At large radii, it agrees with the NFW profile [90, 17] as seen in figure 2.2.

2.6 Types of lensing

The underlying principle for lensing comes from the bending of light, but depending of the situation of the system, it can be classified as one of the three main types which are strong lensing, weak lensing, and microlensing.

2.6.1 Strong lensing

All the derivation presented up until now can directly represent strong lensing. The effect is most commonly produced by extended lenses describing objects like galaxies or galaxy clusters. Furthermore, it can be formed by dark matter and baryons, and generally multiple images are observed [103]. The biggest feature found in strong lensing is the existence of huge arcs in the sky with a radius which corresponds to

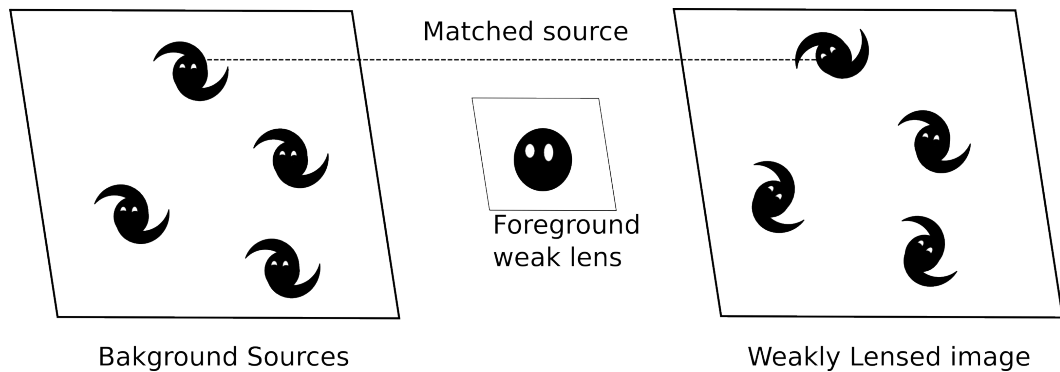


Figure 2.4: Representation of the process of weak lensing. The image of several background sources is slightly distorted by a lens. The aberration is so weak that the effect is found by identifying discernible patterns in the statistical distribution of sources.

the size of Einstein angle; this feature is called an Einstein ring. Furthermore, it is frequently observed the presence of multiple images. In fact, any mass distribution with a surface density bigger than the critical surface density of the lensing system, Σ_{crit} , will produce a discernible lensing effect.

An example of strong lensing can be observed in figure. 2.3. This is a galaxy-galaxy lens system where a far galaxy, with a blue colour, is lensed by another which is in the foreground, with a red hue, producing a big arc or Einstein ring. It is possible to observe that this “horse shoe” is formed by two images of the same galaxy which lie almost in perfect alignment following the Einstein ring. It is important to realize the aberration produced in the lensing is the result of the change of solid angle. The work presented in this thesis will be considering the effect of strong lensing.

2.6.2 Weak lensing

The presence of arcs and multiple images is in the domain of the strong lensing, but there is also the case when the magnification factor is very close to unity. In this case there are small distortions and relatively small amplifications, and the effect or distortion of sources cannot be identified individually, but they have to be treated statistically analysing large number of sources. This is done using source populations

observed e.g. in galaxy or clusters surveys taking into account a large solid angle on the sky [103]. The occurrence of weak lensing can be understood in terms of the surface mass density. When the mass contained inside a specific radius in a mass distribution possesses a surface mass density that is significantly smaller compared with the critical surface density of the lensing system, but contains enough mass to deflect the light of the source, it will produce a slight distortion, but this will not be enough to generate multiple images or discernible arcs compared with the strong case [103]. Weak lensing is generally detected by statistically analysing background sources, to identify the signature of small distortions caused by a foreground lens. Figure 2.4 presents the basic idea behind this.

2.6.3 Microlensing

There is another case where arcs and multiples images are produced, but the separations between them cannot be resolved and only the apparent brightness changes are observed; this is known as microlensing. Usually, it is produced by compact objects which are sufficiently distant in relation to the lens and source and which have low masses with a range of $M/M_{\odot} \leq 10^6$; they produce angular separations of the order of milli-arcseconds. Frequently, this is the case of objects lensed by stars or stellar mass black holes. [78, 103].

Chapter 3

Bayesian inference for data analysis

Some concepts of data analysis will be described in following chapters. For this reason, a short introduction to some of the techniques employed will be presented before hand. Instead of explaining each of the independent type analyses, a general approach will be described, with particular emphasis at the end of the chapter on nested sampling which will be used later.

Usually when the words probabilities and statistics are encountered, the first thought is related to a large representative number of events which will serve to represent or describe a phenomenon. This idea is related to the so-called “frequentist” approach to statistics. For this case, it is crucial to consider the collection of data from many repetitions of an experiment, from which statistics are constructed [110]. Sometimes, however, it is not possible to have the luxury to repeat the experiment, due for example to cost or time constraints, and it may be the case that only one experiment can be performed - as happens often in particular with astronomical events. This presents a challenge when trying to construct statistics and draw inferences about the phenomenon being studied. Such cases are well suited to an alternative, Bayesian approach [44].

Despite the foundations for Bayesian inference existing since the Eighteenth century, the extensive use of it as a tool for science did not happen until the 1990s, which was influenced by the development of computational power [30, 9]. Furthermore, the

last decade has seen an increase of its applications, especially in data analysis for astronomy [35, 108].

3.1 Bayesian inference

Before introducing how Bayesian inference works, it is worthwhile to explain the type of reasoning which is behind it. When dealing with the exact sciences, we can expect there to be an established set of rules which will lead to a definite conclusion. There is no other place where this is true as in pure mathematics, where it is possible to follow a set of well-defined axioms and reach a logical consequence [44]. By analogy, this also happens in everyday life when an event is experienced several times, and it is possible to work from the cause to its consequences. This is the idea of deductive logic or reasoning. Unfortunately, however, in several areas of science the above situations are not true. For these cases, it is necessary to work from the observed results and use the best of knowledge to try to describe the possible causes. This can be done by starting with simple models which could explain a selected number of cases; for example, to obtain the speed of a moving car, the problem can be simplified by considering the totality of the car as a single object and taking the average speed as a ratio of the distance over time. This serves as a good method to help to estimate how fast a driver travelled to a destination. However, nature is more complex, which makes necessary to adjust the underlying models accordingly. The complexity of the reasoning pushes us to assign the idea of a probability of an event, experiment or result to be obtained. From here, two distinct approaches to defining what we mean by probability can arise. The first will be in the sense of repetition. To explain more simply, if an experiment is designed and run several times, changing some of the variables, it is possible to assess some of the outcomes and study the relative frequency of produced results. This is the frequentist definition of probability [110].

In recent years, a second way to approach the problem has become popular [9]. This is by taking into account the "plausibility" given a set of parameters or model. This gives a more logical approach instead of dealing only with the repetition of a random

set of variables. This is the Bayesian probability theory [110, 44].

3.1.1 Bayes' theorem

Richard Cox constructed a set of quantitative rules which help to express the truth of our beliefs or how plausible they are [44]. First, we establish the amount of knowledge we know as "true" which will help to define what it is false. This can be stated by the sum rule of probability

$$p(A|B) + (\bar{A}|B) = 1, \quad (3.1)$$

where the symbol A stands for the proposition which is accepted as true while \bar{A} denotes it as false. At the end, the sum of both gives the complete probability, which is normalized as 1. On the other hand, the symbol B asserts a proposition as true. Thus the meaning of $p(A|B)$ reads as the probability of A being true given the truth of the information encoded in proposition B [44].

The second statement to establish is the amount of trust, or belief, that both, A and B , are true. This is done by the product rule, and it can be given by [110]

$$\begin{aligned} p(A, B|C) &= p(A|C) \times p(B|A, C) \\ &= p(B|C) \times p(A|B, C). \end{aligned} \quad (3.2)$$

where the coma reads as "and", indicating that both propositions A and B are true given the proposition C , and it is commonly referred as the joint probability. Following from here, it is easy to derive Bayes' Theorem; from the product rule, by arranging of the different parts of the formula, it can be read as follows [110, 44],

$$p(A|B, C) = \frac{p(A|C) \times p(B|A, C)}{p(B|C)}. \quad (3.3)$$

The use of the theorem becomes more apparent if we declare more concretely the meanings involved by rewriting it as

$$p(H_i|D, I) = \frac{p(H_i|I) \times p(D|H_i, I)}{p(D|I)}, \quad (3.4)$$

where we establish a better meaning by defining $H_i \equiv$ proposition of the hypothesis of interest, $I \equiv$ representing the prior information and $D \equiv$ the data. With this the

meaning of the several parts of eq. (3.4) reads as follows: $p(D|H_i, I)$ is the probability of obtaining data if the hypothesis and the prior information are true, which is also called the likelihood function $\mathcal{L}(H_i)$. $p(H_i|I)$ is the prior probability that hypothesis is true (i.e. prior to obtaining the data) often referred only as the prior. $p(H_i|D, I)$ represent the posterior probability of H_i referred only as the posterior. The last term which is the probability of the data to be true given the prior information acts as a normalization factor defined as $p(D|I) \equiv \sum_i p(H_i|I) \times p(D|H_i, I)$ which ensures $\sum_i p(H_i|D, I) = 1$.

3.1.2 Hypothesis space

It is important to notice that during the Bayesian analysis it is desired to establish some certainty about the hypothesis, H_i . Therefore, the complete set of possible values to assess regarding our hypothesis is considered the hypothesis space [44]. The problem could be as simple as having some very well defined values for which the total number could be counted. In this sense, it would be an example of a discrete hypothesis space, where we obtain the totality of the posterior space, normalized, by adding each one of the probabilities as [44]

$$\sum_{i=1}^N p(H_i|D, I) = 1. \quad (3.5)$$

Here N is the total number of considered discrete hypotheses.

Possessing a discrete space is not the only possibility. There could instead be the case where the hypothesis space is continuous. This is more common given that the number of propositions are generally considered to be arbitrarily large, and it would produce a space where the number of outcomes cannot be discretely counted. As a general example, it is possible to consider a parameter H_a , which is related with some data D . If the estimation of this arbitrary parameter is in the continuous case then we must consider the probability that the parameter lies in an interval h to $h + dh$. This translates to our posterior by being a “probability density function” (pdf) for which [44]

$$p(H_a|D, I) \equiv \lim_{\delta h \rightarrow 0} \frac{p(h \leq H_a < h + \delta h|D, I)}{\delta h}. \quad (3.6)$$

It is clear that the continuous pdf is simply the infinitesimal component of the posterior probability. Taking this into account, it is meaningful to define the probability that the parameter lies in a specific range, $h1$ to $h2$, by taking the integral [44]

$$p(h1 < H < h2|D, I) = \int_{h1}^{h2} p(H_a|D, I)dH. \quad (3.7)$$

Following the same normalization as for the discrete case, the condition now reads as

$$\int_{\Delta H} p(H|D, I)dH = 1, \quad (3.8)$$

where ΔH is a range of integration appropriate to the problem being considered and which will be designated as the corresponding hypothesis space of interest.

3.1.3 Marginalization

Depending on the model, there are cases where there are one or more parameters which are not of interest for the analysis we desired to realize; these are commonly referred as nuisance parameters [44]. In Bayesian inference, there is a clever way to deal with these parameters. First, it is necessary to introduce two logic statements which will be very useful.

Following from the product rule and the sum rule, it is possible to state a general sum rule; nevertheless, for clarity, an example of only two parameters is as follows. Considering the total probability

$$p(A + B|C) + p(\overline{A + B}|C) = 1, \quad (3.9)$$

by use of the sum rule and the product rule, it is straightforward to derive [44, 110]

$$p(A + B|C) = p(A|C) + p(B|C) - p(A, B|C), \quad (3.10)$$

where the logical property $\overline{A + B} = \bar{A}, \bar{B}$ was used. As stated before the comma is the logical AND. It must be remarked that $p(A, B|C)$ is the probability of both A and B given C . Now, for illustrative purposes of the usefulness of marginalization we are going to consider a simple case with only 3 parameters, θ , A_1 and A_2 . For this

example, A_1 and A_2 represent the complete discrete space of A , and they will act as our nuisance parameters. Following from (3.10),

$$p(A_1 + A_2|I) = p(A_1|I) + p(A_2|I) = 1. \quad (3.11)$$

Here I represents our prior information which establishes that only one of the two states A_1 and A_2 is true - i.e. they are mutually exclusive. This agrees with the definition of the hypothesis space from (3.5). We now want to obtain the posterior on our desired parameter, θ , which do not contain the nuisance parameters; first, we derive an expression for it in terms of the joint distribution of θ and nuisance parameters, i.e. $p(\theta, [A_1 + A_2]|D, I)$ [44]. Using the product rule

$$\begin{aligned} p(\theta, [A_1 + A_2]|D, I) &= p([A_1 + A_2]|D, I) \times p(\theta|[A_1 + A_2], D, I) \\ &= p(\theta|D, I). \end{aligned} \quad (3.12)$$

To go from the first to the second line on the right hand side, the general sum rule and (3.11) establish the relation with the prior information, I . The first term is equated to 1, as shown in eq. (3.11). The second term contains the sum of the combination $[A_1 + A_2]$, which as said earlier, they are the complete space of A ; therefore, as this sum must be true, they do not need to be written. The left hand side of eq. (3.12) can be expanded by considering the distributive property of Boolean algebra as

$$\begin{aligned} p(\theta, [A_1 + A_2]|D, I) &= p(\{\theta, A_1\} + \{\theta, A_2\}|D, I) \\ &= p(\theta, A_1|D, I) + p(\theta, A_2|D, I). \end{aligned} \quad (3.13)$$

The second line of the right hand side is obtained from the mutual exclusivity between A_1 and A_2 . Finally, combining the results from (3.12) and (3.13) gives

$$p(\theta|D, I) = \sum_{i=1}^2 p(\theta, A_i|D, I). \quad (3.14)$$

Hence we obtain at the end a posterior probability which does not utilize the nuisance parameters. For this reason, the procedure of adding up and getting rid of the nuisance parameters is called marginalization. For the discrete case, it is possible to extend to

N elements and not just the considered in the example. In the continuous case the sum is replaced by an integral as [44]

$$p(\theta|D, M) = \int d\phi p(\theta, \phi|D, M) \quad (3.15)$$

where ϕ represent the nuisance parameters and M is the model under study. In this case, $p(\theta|D, M)$ is also called the marginal posterior pdf for θ . In fact, it is easy to observe that the global likelihood is a special case of marginalization which considers all of the parameters, and they are marginalized out from the joint prior distribution. As well, it is important to emphasize this advantage of Bayesian inference over the frequentist approach because in the latter there is no general procedure to deal with this nuisance of parameters [44].

The following sections will describe the two main problems found in statistical analysis: the parameters estimation and the model comparison.

3.2 Parameter estimation

Frequently a particular model may have more than one parameter which describes its behaviour or properties. This would be uninteresting if specific values of these parameters were known before hand, and there would be no need to determine them at all, but of course in general this is not true, and the best we can do in the majority of cases is to have some knowledge of the range that these parameters can obtain [44, 110]; this is encapsulated in the prior information of the model, M , which can be assigned a probability $p(\theta_i|M)$ for the parameters θ_i . This prior probability could be discrete, but it is more common to have a continuous space where the parameters can lie in an interval $[\theta_i, \theta_i + d\theta_i]$ therefore the probability is given by the prior density $p(\theta_i|M)d\theta_i$. As mentioned in the previous section, this describes a probability density function or pdf. As an example, if we have only one parameter, the global likelihood is [44]

$$p(D|M) = \int d\theta p(\theta|M)p(D|\theta, M) = \mathcal{L}(M). \quad (3.16)$$

In the previous section it was mentioned that this is a special case of marginalization. Here can be seen that the posterior is simply the product of the prior and the likelihood

pdf. From here, it becomes clear how Bayes' theorem can give information about the values of the parameters. Rather than explicitly giving a specific solution, it gives a probability in the parameter space as a solution. This is the posterior pdf $p(\theta|D, M)$. The idea is to use the prior probability, which corresponds to any knowledge or constraint we know, and multiply this by the likelihood probability, which describes in this case how likely the parameters fit the data to the model. The likelihood is also called the sampling probability [44, 110]. Using Bayes' theorem to obtain information about the parameters from the data is called parameter estimation [44, 110].

3.3 Model comparison

Before a solid experimental description is achieved, a phenomenon is explained through a model, but it is not always so easy to relate the output of these two directly, and several models can help to explain the same phenomenon. In such cases it is desired to use Bayes' theorem to compare the models and obtain the probability of each one. This procedure is usually called model comparison, and it is the second most common application of Bayesian inference [44].

One excellent analogy of how this is achieved is the Occam's razor [44, 110]. This is usually stated as "The simplest explanation it is always the correct one" [44]. In the same sense, Bayesian analysis incorporates this idea naturally in its formulation. To explain this, it is ideal to consider two or more specific alternative models, M_i , which try to explain the same phenomena. The prior information assumes that one of these models is true; this is stated as $I = M_1 + M_2 + M_3 + \dots + M_N$, where the "+" is the logical disjunction "or" [44]. For the different models there is a posterior $p(M_i|D, I)$. In an analogous way to parameter estimation, the posterior probability gives us information regarding each model. To compare this, instead of using the probabilities directly, it is more useful to consider the ratio

$$O_{ij} = p(M_i|D, I)/p(M_j|D, I), \quad (3.17)$$

which is called the odds ratio in favour of model M_i over M_j . By applying equa-

tion (3.4),

$$\begin{aligned} O_{ij} &= \frac{p(M_i|I) p(D|M_i, I)}{p(M_j|I) p(D|M_j, I)} \\ &= \frac{p(M_i|I)}{p(M_j|I)} B_{ij}, \end{aligned} \quad (3.18)$$

where the first ratio at the right is the odds ratio in favour, and B_{ij} is called the Bayes factor. It can be seen how this simplifies the computation, and helps by dropping the normalization factor. Likewise, the odds ratio considers the prior information ratio regarding each of the models to analyse, but usually it is possible to simplify it by assuming the same prior information for both models which is a good consideration because this prevents some bias when there is not much previous information [44, 110]. For the following example this will be the case.

Consider two models, M_1 with a single free parameter, θ , and M_0 with a fixed value θ_0 and no free parameters. Assuming that the prior information is the same for both, this reduces the odds ratio to only calculate the Bayes factor, B . The objective is to calculate $p(D|M_1, I) = \mathcal{L}(M_1)$. The first assumption is that for both models the prior is a flat prior which will have a width $\Delta\theta$, and no dependence on the parameters, so the normalization for the prior reads,

$$\int_{\Delta\theta} d\theta p(\theta|M_1, I) = p(\theta|M_1, I)\Delta\theta = 1, \quad (3.19)$$

and therefore

$$p(\theta|M_1, I) = \frac{1}{\Delta\theta}. \quad (3.20)$$

Assuming that the data is confident enough, this will lead to expect the likelihood function for the parameter θ to be more concentrated in a region around the best-fit value, $\hat{\theta}$ [44]. Taking a simplification, the region around this value, can be represented by a characteristic width defined by

$$\int_{\Delta\theta} d\theta p(D|\theta, M_1, I) \approx \mathcal{L}(\hat{\theta}) \times \delta\theta, \quad (3.21)$$

and the global likelihood can be approximated as

$$\begin{aligned} p(D|M_1, I) &= \int d\theta p(\theta|M_1, I)p(D|\theta, M_1, I) = \mathcal{L}(M_1) \\ &\approx \mathcal{L}(\hat{\theta}) \frac{\delta\theta}{\Delta\theta}. \end{aligned} \quad (3.22)$$

Because the second model has no free parameters, the global likelihood corresponds exactly to the equivalent of the probability for the likelihood of the model M_1 on the value θ_0 ,

$$p(D|M_0, I) = p(D|\theta_0, M_1, I) = \mathcal{L}(\theta_0). \quad (3.23)$$

The Bayes factor is obtained as

$$B \approx \frac{\mathcal{L}(\hat{\theta})}{\mathcal{L}(\theta_0)} \frac{\delta\theta}{\Delta\theta}. \quad (3.24)$$

It is now clearer to understand how Occam's razor works in Bayesian inference. The Bayes factor is comprised by two ratios: a ratio of likelihood and a ratio of widths [44]. From the first the simpler model would never be favoured due to being a special case, but from the posterior width $\delta\theta$ is narrower than the prior width $\Delta\theta$, so the second factor acts as a penalty for the complicated model. If the likelihood ratio is able to overcome the penalization by justifying the amount of parameter space for the extra parameter, then the more complicated will be preferred [44, 110]. From the previous example, it can be seen that the global likelihood can be written as the maximum value of the likelihood of a parameter times some factor,

$$p(D|M, I) \equiv \mathcal{L}_{max}\Omega_\theta. \quad (3.25)$$

The second factor is called the Occam factor, and it contains information for the quantitative function behind the notion of Occam's razor.

3.4 Markov Chain Monte Carlo (MCMC)

For Bayesian analysis, the desired quantity to obtain is the posterior probability $p(M|D, I)$, and this is done by calculating the likelihood function and multiplying

by the prior [44]. But in general, this cannot be obtained from an analytical function, instead, it could be obtained by the generation of a grid in the parameter space; nevertheless, this is not the most efficient way to approach the problem, due to the increase in dimensionality. For example, by placing 10 points for each dimension, the total number of grid points will increase up to 10^N , where N is the total number of dimensions, so it is clear how this strategy becomes quickly inefficient. A more clever approach to the problem would be by the implementation of a stochastic sampler [43].

The most widely used method is Markov Chain Monte Carlo (MCMC) [43, 44]. The idea behind it, comes by the combination of two techniques: a Monte Carlo sampler and a Markov Chain [132]. In practice, instead of obtaining the likelihood from the analytical function, the properties would be analysed by taking random samples; this idea comes close in analogy to the Monte Carlo integration schemes. Using the random samples obtained from the Monte Carlo sampling, as X_1, \dots, X_n , these samples describe the present state, and they can be used to determine the future, or posterior, distribution. The relation between them can be stated as [132]

$$p(X_{n+1} = x | X_1 = x_1, X_2 = x_2, \dots, X_n = x_n) = p(X_{n+1} = x | X_n = x_n). \quad (3.26)$$

This means that the posterior distribution only depends on the present state or collection of samples. Depending on the situation this could be a discrete or continuous space, but in this case it becomes a transition probability which is usually defined as $K(x, y) = p(X_{n+1} = y | X_n = x_n)$. Following from this, there is a corresponding proposal density

$$\pi(y) = \int dx \pi(x) K(x, y), \quad (3.27)$$

where $\pi(x)$ and $\pi(y)$ correspond to the prior and posterior distributions respectively. In fact, given that after the application of the transition probability $K(x, y)$ to the prior probability in state x , and it is desired to remain with the same probability at the posterior in state y ; the distribution is, in this case, invariant. For this reason, the previous requirement in eq. (3.27) defines a stationary distribution [132, 108].

In principle, the objective is to randomly sample towards this distribution until

convergence is achieved. For this goal, the sampler must satisfy the following properties [132]:

- Irreducible - The sampler should be able to obtain a positive probability, in a finite number of steps. This means the stationary distribution is unique.
- Aperiodic - There should be no oscillations in between finite states.
- Positive recurrent - it means that there should exist a stationary distribution.

A stationary distribution could have another property where you could go forward or backwards in the distribution, $p(X_n, X_{n+1}) = p(X_{n+1}, X_n)$, then it is said to be reversible [43]. For the transition kernel it reads,

$$\pi(X_n)K(X_n, X_{n+1}) = \pi(X_{n+1})K(X_{n+1}, X_n), \quad (3.28)$$

which is known as the condition of detailed balance. This is not necessary, but it guarantees the convergence of a stationary distribution [43, 108]. To apply the MCMC, several algorithms exist, but the most famous is The Metropolis-Hastings [132]. In the next section, a different approach to that of MCMC is presented, which is the one used later for analysis in this work.

3.5 Nested sampling

The strategy used for MCMC is not the only one. There are others, and one of those is nested sampling [111]. As mentioned earlier, the main goal of the Bayesian analysis is to obtain the posterior probability by the use of the prior and the likelihood. One probability which usually is disregarded because it only acts as a normalization factor is $p(D|I)$. For nested sampling, this factor is going to become an evidence, and it is usually defined as

$$Z = \text{evidence} = \int \mathcal{L}dX, \quad (3.29)$$

where $\mathcal{L} = \mathcal{L}(\theta)$ is the likelihood function, $dX = \pi(\theta)d\theta$ is the element of prior mass and θ represents the unknown parameter(s) [111]. The prior mass can be understood

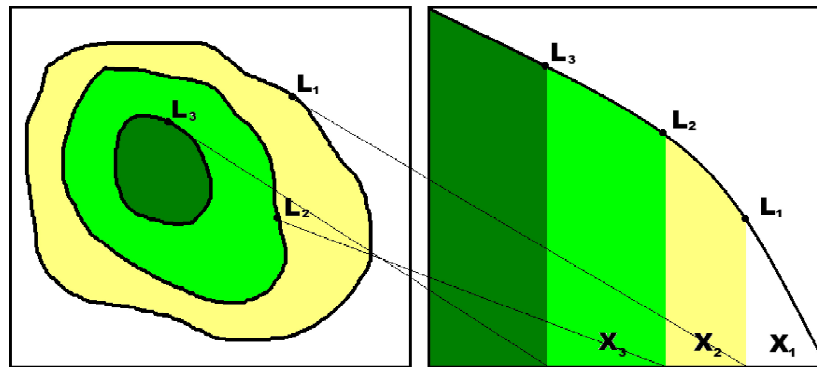


Figure 3.1: Sketch representing the mapping from the prior mass curve $X(L)$, at the right to the parameter space, at the left, which describes the boundaries of equivalent likelihood \mathcal{L} .

as the prior integrated over an hyper-volume of the parameter space bounded by a maximum likelihood [64]. From the Bayes' theorem, and to be able to relate with the previous nomenclature, it is rewritten as

$$p(D|\theta, I)p(\theta, I) = p(D|I)p(\theta|D, I)$$

$$\mathcal{L}(\theta) \times \pi(\theta)d\theta = Z \times p(\theta)d\theta. \quad (3.30)$$

From here, the idea can become clearer. In the standard MCMC strategy, the desired product is the posterior, and it is obtained by sampling through the likelihood and prior. In nested sampling the desired quantity is the evidence Z , and therefore, the posterior is a by-product of the process. Before explaining how the posterior is obtained, first consider how the evidence is determined [111]. As mentioned before this is not an easy task, especially when it is done for a higher number of parameters, the number of dimensions increases. For this purpose the first objective is avoid this problem, and it is done by taking into account that it is possible to do a transformation so that, instead of integrating over the space of all parameters, the problem is reduced to a one-dimensional case by performing the integral using the prior mass X , which in turn is a decreasing function from 1 to 0 [111]. Therefore, the evidence is defined as

$$Z = \int_0^1 \mathcal{L}(X)dX. \quad (3.31)$$

This transformation accomplishes a simplification of the problem of dimensionality, and the strategy becomes from reducing the prior mass into smaller elements and sorting them by likelihood. Then, the only thing left is to perform the integral which considering the smoothness of the transformation can be done by assuming a weighted sum

$$Z \leftarrow \sum_{i=1}^m \omega_i L_i, \quad (3.32)$$

where $L_i = \mathcal{L}(X_i)$, and this represents the integral by an approximated sum of columns of width ω . The nested sampling idea comes in place, by taking random steps i of a point X_i where $X_i < X_{i-1}$ starting at $X_0 = 1$. From this point, the next step could be to obtain the corresponding value of θ . But this can be simplified by taking directly the value of θ_i , and sampling considering the similar constraint $L(\theta) < L_{i-1}$, with the initial value L_0 [111]. This takes a random sample in the same way, but it has the advantage to bypass the need to sort the values of X . In other words, the selection of prior mass is mapped into a region of similar likelihood in the parameter space which is compared and delimits a likelihood boundary, as exemplified in fig. 3.1. The random sampling will search and compare the different likelihoods to reduce the area until the highest likelihood is found. For the case of model selection, the evidence is more important to obtain, but for the case of parameter estimation, it is desired to obtain a posterior which is the prior weighted by the likelihood [37]. During the nested sampling process, which is done under the area of the one dimensional curve $\mathcal{L}(X)$, the posterior is obtained as a by-product. The evidence is already decomposed by the integral in $\sum L_i \omega_i$, which is exactly desired values to calculate the posterior, if it is properly normalized by Z ,

$$p_i = L_i \omega_i / Z. \quad (3.33)$$

The evaluation of the different sampling points is done by Monte Carlo methods. As well as with other techniques, there are different codes available to perform the process. The code used for the analysis in later chapters is described in the following subsection.

3.5.1 Multinest

There is a common problem which is shared by several stochastic samplers. Wherever there is a region of high likelihood, the samplers tend to find it, but there are several problems where there is the case of more than one of these regions. However, in principle, there will exist a highest region and what is needed is an intelligent strategy to find the correct region, and avoid the sampler to get trapped in the smaller regions.

Multinest is a code which treats this problem by using an ellipsoidal approximation to the sampling process, and afterwards it reduces the region of analysis [36]. The advantage is that it proposes an algorithm which can efficiently sample new points within the active region. Using this approach the method becomes efficient in scenarios when multiple such regions appear. For this reason, this is the code used to obtain the results from the analysis described in a later chapter.

Chapter 4

Lensing of scalar field dark matter

This chapter introduces the use of a scalar field dark matter profile as a lens model. It includes a description of the mathematical expression of the lens equation to be appropriate to work with the model. It also has a brief review of previous work done with other scalar field models. Starting from section 4.4, it is presented for the first time the derivation of the analytical lensing functions necessary to work with the particular WaveDM model as a lens which were carried out as part of the work of this thesis.

4.1 The reduced lens equation

In chapter 2, the basic concepts for gravitational lensing were introduced, specially eq. (2.9) which describes the relation between the source and the apparent images. From the lens equation, the important distances are between observer and lens, D_{OL} , lens and the source, D_{LS} , and from observer to source, D_{OS} . Recalling eq. (2.21), the lens equation for an extended distribution as [102],

$$\beta = \theta - \frac{M(\theta)}{\pi D_{OL}^2 \theta \Sigma_{cr}}. \quad (4.1)$$

The value $\Sigma_{cr} = c^2 D_{OS} / 4\pi G D_{OL} D_{LS}$ is the critical surface density. Although this form is the most popular form of the expression, it is not so convenient to use because it contains several constants dependent of the geometry of the system, and the explicit parameters which is not convenient for handling the equations. Therefore, normalizing

the equation into a more comfortable form is possible by using the density and radius of the profile. The normalization for the surface mass density is then

$$\Sigma_*(\xi_*) = \frac{\Sigma(\xi_*)}{\rho_c r_c} = 2 \int_0^\infty \frac{\rho(\xi, z_*)}{\rho_c} dz_*, \quad (4.2)$$

This define the dimensionless variables, $r/r_c = \sqrt{\xi_*^2 + z_*^2}$, $z_* = z/r_c$ and $\xi_* = \xi/r_c$. ρ_c is the central density for the profile and r_c is the characteristic radius or another normalization radius. Similarly, the reduced mass is normalized accordingly,

$$m_*(\theta_*) = \frac{M(\xi_*)}{\rho_c r_c^3} = 2\pi \int_0^{\xi_*} d\xi'_* \xi'_* \Sigma_*(\xi'_*). \quad (4.3)$$

As a result, it is possible to rewrite it as a dimensionless lens equation,

$$\beta_*(\theta_*) = \theta_* - \lambda \frac{m_*(\theta_*)}{\theta_*}. \quad (4.4)$$

In this manner, the different distances are normalized in terms of r_c : $\beta_* = D_{OL}\beta/r_c$, $\theta_* = D_{OL}\theta/r_c$, and this relates $\xi_* = \xi/r_c = \theta_*$. With this definition ξ_* and θ_* are interchangeable. As seen in eq. (4.4), we referred to a parameter λ which is defined as

$$\lambda \equiv \frac{\rho_c r_c}{\pi \Sigma_{cr}} = 0.57 \times 10^3 \left(\frac{1}{h} \right) \left(\frac{\rho_c r_c}{M_\odot \text{ pc}^{-2}} \right) \frac{d_{OL} d_{LS}}{d_{OS}}, \quad (4.5)$$

which is done to contains the distances and characteristic parameters and from it obtain the lensing information of the system and the model. The reduced angular distances are introduced as $d_A \equiv D_A H_0 / c$ where the sub-index A can refer to sub-indexes OL , LS or OS in the equation. The Hubble constant $H_0 \equiv 100h(\text{km/s})/\text{Mpc}$ is properly worked with the units, so only the dimensionless h appears explicitly in the parameter λ , and it only has two values with proper units, which are ρ_c and r_c . The parameter λ defined in (4.5) differs from the one used in [90] by a factor of $1/4\pi$.

When we have the case of a perfect alignment between the source and the lens system, this corresponds to $\beta_*(\theta_{*E}) = 0$; this defines the Einstein angle $\theta_{*E} = R_E/r_c$. Here R_E is more properly referred as the Einstein radius expressed in distance units. This is usually obtained from the Einstein angle as $R_E = D_{OL}\theta_E$ [78]. Using eq. (4.4) is possible to write eq. (4.5) as a function of θ_{*E} ,

$$\lambda = \frac{\theta_{*E}^2}{m_*(\theta_{*E})}. \quad (4.6)$$

Comparing with eq. (4.5), it is possible to observe how the information of the system can be obtained from or parametrised only by the density profile and a particular Einstein radius. Moreover, this indicates an independence of any a priori knowledge of the geometry of the system or of the scaling parameters, namely ρ_c and r_c , and it is only necessary a perfect alignment. A more detailed look of (4.6) and (4.4) indicate the existence of a minimum value $\lambda_{cr} = \lambda(0)$ different from zero. Nevertheless, this value has a divergence, which can be avoided by the use of L'Hôpital rule,

$$\lambda_{cr} = \frac{d(\theta_{*E}^2)}{d\theta_{*E}} \left(\frac{d(m(\theta_{*E}))}{d\theta_{*E}} \right)^{-1} \Big|_{\theta_{*E}=0}. \quad (4.7)$$

This defines the minimum value as

$$\lambda_{cr}^{-1} \equiv \pi \Sigma_*(0), \quad (4.8)$$

where

$$\Sigma_*(0) = 2 \int_0^\infty \frac{\rho(z_*)}{\rho_c} dz_*. \quad (4.9)$$

This gives the minimum parameter λ that a particular profile will require to produce strong lensing. $\Sigma_*(0)$ represents the central value of the surface mass density, and it depends of the profile chosen. A comparison of the effect with the different density profiles is shown in table 4.1. The dimensionless lens equation and λ will be chosen option for the derivation of the equations and analysis described in the rest of the chapter.

4.2 Ultra light Dark Matter profiles

The same underlying principle applies among the different SFDM models [63], but it is possible to find several different formulations for the density profile of galaxies depending in the approximation considered. Here are introduced two of those models. The first is the most generic profile involving the Dark Matter as a Bose-Einstein Condensate (BEC) as presented in [10], and the second is a recently published profile obtained by solving the Shrödinger-Poisson system in [100, 101].

4.2.1 BEC or general SFDM profile

One of the most generic considerations when describing a SFDM model is to consider the galaxy Dark Matter halo as a Bose-Einstein Condensate (BEC) and to use this to describe the density profile of galaxies. The basic idea is to consider an static BEC where the dark matter particles are in a very large ground state [97]. This case, in particular, considers a complex, massive, self-interacting scalar field satisfying the Klein-Gordon equation [73]. A simple example of a solution admits the expression [10, 42],

$$\rho(r) = \begin{cases} \rho_c \frac{\sin(\pi r/r_{\max})}{\pi r/r_{\max}} & \text{for } r < r_{\max}, \\ 0 & \text{for } r > r_{\max}. \end{cases} \quad (4.10)$$

Here $r_{\max} \equiv \sqrt{\pi^2 \Lambda / 2} (\hbar / mc)$ is a constant which gives the Compton wavelength of the scalar particle, \hbar / mc , scaled by a factor of $\Lambda^{1/2}$, and ρ_c is the density at the centre of the configuration. The value of r_{\max} , apart of representing the size where the BEC can be described more classically, indicates the point, where the density and the strong repulsive interactions between the photons drop to zero [46].

4.2.2 ψ DM soliton profile

The description and evolution of small perturbations from the early universe is not an easy task to do. Large Scale Simulations are the default way to deal with this problem, and the N-body simulations for the CDM have been really successful to represent the cosmological scales [83, 79]. For scalar field Dark Matter, this has been approached by many others in several occasions in the last decade [117, 130, 131].

In contrast with CDM, simulations of SFDM with high enough resolution to comparable with latter were not possible until recent years with the results from [100, 101]. The wave mechanical properties of the fields can be solved using the Schrödinger equation and can be coupled to gravity by means of Poisson's equation. This idea and the use of a graphic processing unit accelerated adaptive-mesh-refinement code permitted to realize an evolution of the ψ DM with enough resolution to compare with usual simulations of CDM [101]. With this, it was possible to fit and approximate an analytical

profile for the core of a galaxy, given as [100],

$$\rho_c(r) = \frac{\rho_{sol}}{[1 + \alpha(r/r_{sol})^2]^8}, \quad \alpha = 9.1 \times 10^{-2}. \quad (4.11)$$

where ρ_{sol} represents the central density, and r_{sol} is the characteristic radius of the profile. This solution provides a more precise description of the behaviour of the galaxy core and a better agreement with the size and formation for the dwarf galaxies [96, 116].

4.3 Gravitational lensing with a SFDM profile

The profile presented in eq. (4.10) can be used to represent the extended distribution of a lens. Therefore, to obtain the surface mass density, from eq. (4.2),

$$\Sigma_{*SFDM}(\xi_*) = \frac{2}{\pi} \int_0^{z_{max}} \frac{\sin(\pi \sqrt{\xi_*^2 + z_*^2})}{\sqrt{\xi_*^2 + z_*^2}} dz_*, \quad (4.12)$$

with $0 \leq \xi_* \leq 1$, $z_{max} \equiv \sqrt{1 - \xi_*^2}$, $r_c = r_{max}$, and the normalized projected mass is given by eq. (4.3). Unfortunately, this profile does not have an analytical form, but can be worked numerically [42]. Furthermore, it is possible to estimate the minimum value of parametrization to produce strong lensing which is given by $\lambda_{cr} = 0.27$.

Plotting eq. (4.4) gives a clearer view of the effect for changing the parameter λ can bring to the solution. In figure 4.1, it can be seen different λ for the lens equation in the case of this profile. Because it is normalized, from eq. (4.12) it can be seen there is no dependence in the density or characteristic radius whose information is concealed in λ . The remarkable feature is the different shapes it produces.

The multiple images for strong lensing are produced at the zero crossing of $\beta_*(\theta_*) = 0$ which defines the Einstein radius, $\theta_* = \theta_{*E}$. For a value which is below the critical, the only image would be if the apparent image and the source were aligned, which in this case corresponds to an alignment with the lens which blocks this possibility. Values above this critical value are able to produce a visible strong lensing. Taking a step forward, it is possible to establish a minimum combination of the parameters ρ_c and r_{max} which will produce strong lensing. Combining λ_{cr} and eq. (4.5), the condition for

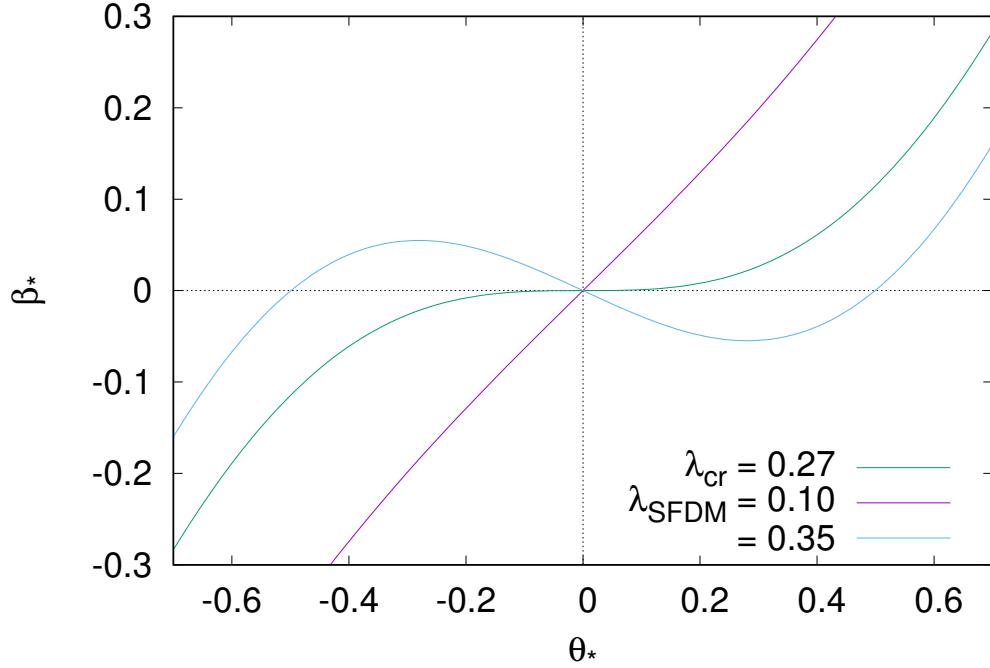


Figure 4.1: The plot of the reduced lens equation for SFDM profile gives the basic idea of the effect that different values of λ produce for the generation of strong lensing. Multiple images, and at the same time the effect of lensing, are created when there is a zero crossing which corresponds to the value of the Einstein radius, θ_{*E} .

strong lensing

$$\rho_c r_{max} [M_\odot \text{pc}^{-2}] \gtrsim 473.68 f_{\text{dist}}, \quad (4.13)$$

with $f_{\text{dist}} \equiv d_{OS}/d_{OL}d_{LS}$. This establishes a condition for the production of strong lensing and hence multiple images. The geometry of the system will set a lower value that will need to be satisfied by the combination of density and characteristic radius. In general these values are not known a priori, but with this, if by other means it is possible to establish any of the two, there will be a minimum combination allowed. This can be used with any data available to constrain the actual values, and one of the most effective is to use the Einstein radius. This idea will be carried over to the next sections and taken advantage for the analysis and conditions to determine the existing relation of this unknown parameters in the different models.

4.4 Gravitational lensing with a WaveDM profile

The profile (4.11) describes a single galactic object which comprises a soliton core, and its advantages are described in section 1.3. The profile was first introduced in [100], but for convenience, it will be much simpler to follow the nomenclature adopted in [70] which satisfy the same Schrödinger-Poisson system [46, 98].

The profile to describe a halo core as a gravitational lens will be

$$\rho_{sol}(r) = \frac{\rho_s}{[1 + (r/r_s)^2]^8}. \quad (4.14)$$

As stated before, ρ_s is the central density and r_s is the characteristic radius which differs from eq. (4.11) by $r_s = r_{sol}/\alpha_{sol}^2$. The plot of the profile can be seen in fig. 4.2. From the equation and plot, it is possible to observe the steep decrease, and when r reaches the characteristic radius, r_s , the density has dropped to ~ 0.004 of the central density. For higher radii this means the contribution of the density, in practice, is negligible or zero. The properties of the profile (4.14) mean it obeys a scaling property as described in [46]. If we have a constant parameter μ , the central density, and radius are described by [96, 41]

$$\rho_s = \mu^4 m_\alpha^2 m_{\text{Pl}}^2, \quad r_s = (\mu \alpha_{sol} m_\alpha)^{-1}. \quad (4.15)$$

As stated in [70], they found a best fit of $\alpha_{sol} = 0.23$ which adjusts the simulations, and agrees with the results given by [100]. This property helps to write the central density in terms of the axion mass and the characteristic radius as

$$\frac{\rho_s}{M_\odot \text{pc}^{-3}} = 2.4 \times 10^{12} \left(\frac{r_s}{\text{pc}}\right)^{-4} \left(\frac{m_a}{10^{-22} \text{eV}}\right)^{-2}. \quad (4.16)$$

This helps to reduce the free parameters of the profile to only two: the characteristic radius and the boson mass. Even more, it establishes an important correlation; by fixing the value of the axion mass, relates the central density and the soliton size. By setting the latter, it will help to constrain the mass of the boson. This relation will become important in the following chapter when attempting to constrain the parameters.

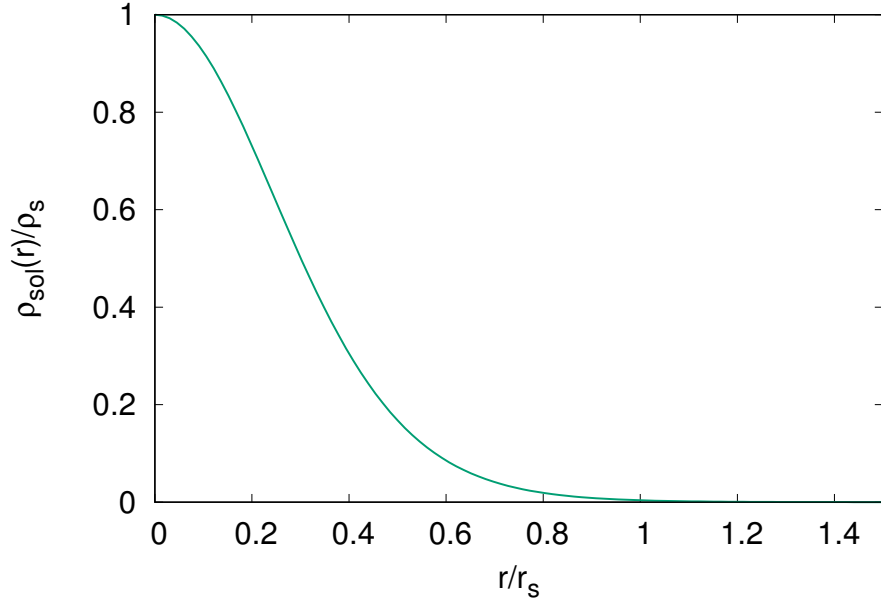


Figure 4.2: Plot of the WaveDM profile (4.14), which shows the steep decrease with radius. The profile is normalized by the central density, ρ_s , and the radius by the characteristic radius, r_s .

To use the profile for lensing, the first step is to obtain the surface mass density; this could be done numerically, but for this case, it can be done analytically by performing eq. (4.2) which is normalized by ρ_s and r_s . In the literature when considering a soliton, it is usually defined with a maximum radius [26, 106, 109], but for the purpose of the lens, it will be treated as an extended object; furthermore, as shown in fig. 4.2, the density drops steeply after it reaches the radius r_s , so further contribution is minimal and is only for mathematical convenience. Using eq.(4.2), the solution to find is,

$$\Sigma_*(\xi_*) = 2 \int_0^{z_{max}} \frac{dz}{[1 + r_*^2]^8} \quad (4.17)$$

where $z_{max} \rightarrow \infty$, and we have introduced another normalized parameter, $r_* = r/r_s$.

The general solution is given by

$$\int_0^{z_{max}} \frac{dz}{[1 + r_*^2]^8} = \frac{1}{(1 + \xi_*^2)^{15/2}} \int_0^x \cos^{14} u \, du, \quad \tan x = \left(\frac{z_{max}^2}{1 + \xi_*^2} \right)^{1/2}, \quad (4.18)$$

Name	Density profile $f(r)$	λ_{cr}
NFW	$[(r/r_s)(1 + r/r_s)^2]^{-1}$	0
Burkert	$[(1 + r/r_s)(1 + r^2/r_s^2)]^{-1}$	$2/\pi^2 \simeq 0.203$
SFDM	$\sin(\pi r/r_s)/(\pi r/r_s)$	0.27
WaveDM	$(1 + r^2/r_s^2)^{-8}$	$\frac{2048}{429\pi^2} \simeq 0.484$

Table 4.1: A comparison of λ_{cr} for several profiles [90, 138, 42]. They are obtained by eq. (4.7).

where $z = \sqrt{r_{\epsilon_*}^2 - \xi_*^2}$, and

$$\int_0^x \cos^{14}(u) du = \frac{\sin x}{14} \left\{ \cos^{13} x + \sum_{k=1}^6 \frac{(13)(11) \dots (14 - 2k + 1)}{2^k(6)(5) \dots (7 - k)} \cos^{14-2k-1} x \right\} + \frac{(13)!!}{2^7 7!} x . \quad (4.19)$$

Applying $z_{max} \rightarrow \infty$, the solution reduces to

$$\Sigma_*(\xi_*) = \frac{429\pi}{2048} (1 + \xi_*^2)^{-15/2} . \quad (4.20)$$

The normalized projected mass is easily found by eq. (4.3),

$$m_*(\theta_*) = \frac{2}{13\lambda_{crit}} \frac{(1 + \theta_*^2)^{13/2} - 1}{(1 + \theta_*^2)^{13/2}} . \quad (4.21)$$

The value of λ_{crit} is the critical value obtained for the profile by the use of the definition in eq. (4.7) which corresponds to

$$\lambda_{crit} \equiv (\pi \Sigma_*(0))^{-1} = \frac{2048}{429\pi^2} \approx 0.484 . \quad (4.22)$$

This value which represents the condition for λ is the combination of physical parameters of the lensing system to produce strong lensing. Table 4.1 compares it with other profiles.

The first observation is that a NFW profile can produce lensing with any combination of parameters, because the minimum is 0. The case of WaveDM is the worst for all presented when only considering the soliton alone, but this will be addressed later by completing the profile with a tail.

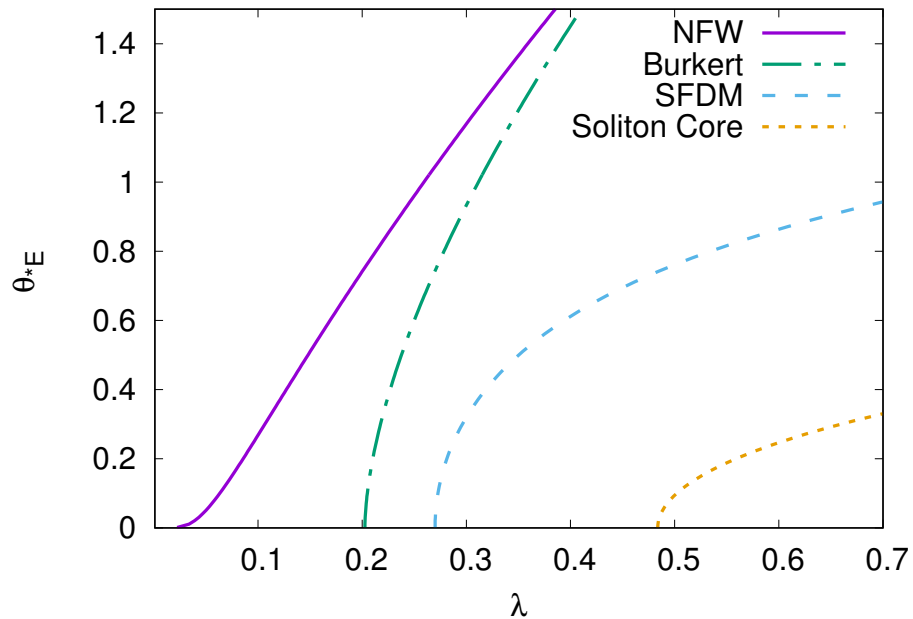


Figure 4.3: Einstein radius as a function of λ . This shows the relation between the different profiles and the values of λ necessary to produce an specific Einstein radius. The minimum value of λ is the corresponding λ_{cr} .

It is possible to establish a relation between the Einstein radius and the necessary parameters of the lensing system through λ . This is shown in fig. 4.3. The value of λ which corresponds with the minimum Einstein radius is λ_{cr} . Here is possible to see the relation between different profiles, as mentioned before, the NFW profile is the most capable to produce strong lensing for any configuration. Meanwhile, the WaveDM profile under-performs in comparison because it needs a minimum configuration to produce strong lensing. This does not mean that this profile is inappropriate, just that the necessary conditions for the lensing are stricter. The next section will address this issue by adding an NFW tail to the inner soliton core.

4.5 A more complete density profile

As mentioned earlier, large scale simulations have been always a useful way to observe the evolution of structure in the universe. One of the results observed was that the majority of dark matter in halos is composed of two parts, and inner and external region [38, 83, 47]. With this intention and considering the approach of SFDM, the first is going to be described by a halo density profile for ultra light scalar dark matter, ψ DM, as described in [100]. The second part is a NFW-like profile which describes the outer part [138]. Both profiles are matched following the procedure shown in [70] because the transitions observed on the simulations are sharp; for this reason, they preferred to use a simple function to connect both. The complete profile is constructed by a simple step function as [70]

$$\rho(r) = \Theta(r_\epsilon - r)\rho_{\text{sol}}(r) + \Theta(r - r_\epsilon)\rho_{\text{NFW}}(r), \quad (4.23)$$

where the r_ϵ is the matching radius, which is where the transition between the profiles happen. Although the combination is done with a simple function, it does not guarantee that the profile will be continuous because there is no theoretical technique to predict where the transition will happen. Therefore, to achieve continuity of the function it is necessary to establish a condition between the two different models. To accomplish this, the only requirement is that $\rho(r_\epsilon) = \rho_{\text{sol}}(r_\epsilon) = \rho_{\text{NFW}}(r_\epsilon)$. This condition is satisfied by choosing the natural transition at a radius between the two different profiles which satisfies the relation

$$\rho_{\text{sol}}(r_\epsilon) = \epsilon\rho_s = \rho_{\text{NFW}}(r_\epsilon). \quad (4.24)$$

This defines the value of the transition radius r_ϵ . Unfortunately, ϵ and r_ϵ are taken as free parameters of the theory. The NFW profile give by

$$\rho_{\text{NFW}}(r) = \frac{\rho_{\text{NFW}}}{(r/r_{\text{NFW}})(1 + (r/r_{\text{NFW}}))^2}, \quad (4.25)$$

where r_{NFW} and ρ_{NFW} are the characteristic radius and the central density.

With the idea of reducing the number of free parameters, it can be defined a relation between the soliton and NFW radius by $r_{\text{NFW}} \equiv r_s\alpha_{\text{NFW}}^{-1}$. This can be contrasted

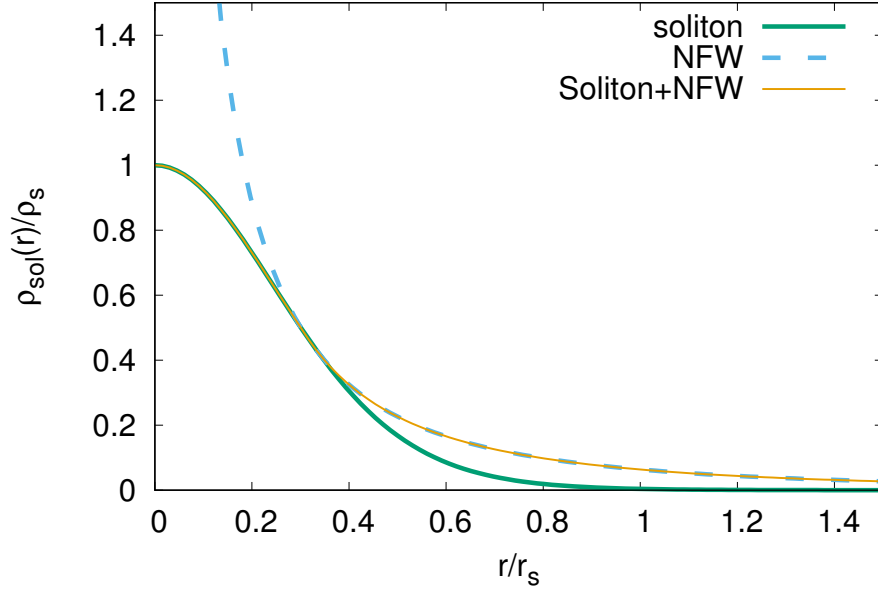


Figure 4.4: Comparison between the complete profile and the individual densities with $r_{\epsilon^*} = 0.300845$ and $\alpha_{\text{NFW}} = 1$. The initial value for the complete profile is normalized to the soliton density and the radii to r_s , so the transition happens at $\epsilon = 0.5$. This was chosen arbitrarily. It can be seen how the individual profiles intersect, and the transition happens. The effect of the soliton section helps to eliminate the divergence present in the NFW profile.

with [70] and in [100] by noticing how the values of this radius are defined. Using this parametrisation allows to redefine the NFW profile in terms of the soliton profile as,

$$\rho_{\text{NFW}}(r) = \frac{\rho_s \rho_{\text{NFW}^*}}{(\alpha_{\text{NFW}} r/r_s)(1 + (\alpha_{\text{NFW}} r/r_s))^2}, \quad (4.26)$$

where $\rho_{\text{NFW}} = \rho_s \rho_{\text{NFW}^*}$. This increases the number of parameters, so it is necessary to reduce them somehow. First, it is important to notice the condition established by eq. (4.24), which can be combined with the profile in eq. (4.14) and used to describe a direct relation between ϵ and r_{ϵ} ,

$$r_{\epsilon^*} = (\epsilon^{-1/8} - 1)^{1/2}. \quad (4.27a)$$

This helps to define the dimensionless matching radius as $r_{\epsilon^*} \equiv r_{\epsilon}/r_s$, and establishes the interchangeability with the parameter ϵ .

Second, it is possible to apply the same condition to the NFW profile to produce a relation

$$(r_{\epsilon^*} \alpha_{\text{NFW}})(1 + r_{\epsilon^*} \alpha_{\text{NFW}})^2 = \epsilon^{-1} \rho_{\text{NFW}*}. \quad (4.27b)$$

We can use eq. (4.27a) to get rid of the dependence in ϵ , and rewrite as

$$\rho_{\text{NFW}*} = \frac{\alpha_{\text{NFW}} r_{\epsilon^*} (1 + \alpha_{\text{NFW}} r_{\epsilon^*})^2}{(1 + r_{\epsilon^*}^2)^8}. \quad (4.27c)$$

The important remark about eq. (4.27c) is that it describes the normalized density needed to match the soliton profile at the transition radius once the parameters α_{NFW} and r_{ϵ^*} are given. In fig. 4.4 is shown a comparison between the complete profile and the individual parts for an arbitrary value of ϵ .

In total for the complete profile there are 7 free parameters: $m_a, r_s, r_\epsilon, r_{\text{NFW}}, \rho_s, \rho_{\text{NFW}}$ and ϵ . But with the parametrisation chosen, they are replaced by 5 parameters: $(m_a, r_{\epsilon^*}, \alpha_{\text{NFW}}, \epsilon, \rho_{\text{NFW}*})$. Nevertheless, by means of eq. (4.27), it is possible to describe 2 of those free parameters in terms of the rest, so the total number is reduced to only 3: $(m_a, r_{\epsilon^*}, \alpha_{\text{NFW}})$. Because the actual mass of the axion, m_a , it is an important quantity of the SFDM models and is desired to confirm its range of value in conjunction to other analysis as done in [21], it is better to fix it to particular set of chosen representative values for the testing purposes of this work. The meaning of this is that only 2 free parameters are considered to be of interest for lensing purposes.

4.5.1 Surface mass density

One of the important steps in being able to analyse the effects of gravitational lensing comes from the lens equation. For this reason, profiles are generally assumed symmetric unless they have clear dependence of the direction of light [102]. Therefore, considering the symmetric distribution, the lens equation in polar coordinates can be obtained just with the radial vector. In this case, the deflection angle defined for an extended mass distribution is obtained from the surface mass density as in eq. (2.19). Therefore, it is necessary to derive the equation for $m(\xi_*)$. Using the definition of the profile from (4.23), the next step is to obtain the surface mass density as defined in eq. (2.18).

The integral is done along the line of sight on the variable z , and it encloses a circle of radius ξ_* , so it is necessary to integrate over this, cylindrical coordinates, and perform the change of variable $r = \sqrt{\xi^2 + z^2}$. Because the distribution is an even function, it reduces to twice the integral from zero to infinity. Including the profile (4.23), the surface mass density to derive will be

$$\Sigma(\xi) = 2 \int_0^\infty [\Theta(r_\epsilon - r)\rho_{sol}(r) + \Theta(r - r_\epsilon)\rho_{NFW}(r)] dz. \quad (4.28)$$

It should be noticed that only the amplitude $|\boldsymbol{\xi}| = \xi$ is necessary due to the symmetry. To apply correctly the separation of the integral, the radius is considered as $r = \sqrt{\xi^2 + z^2}$. This implies there is a separation in terms of z when evaluating at $r = r_\epsilon$.

The first case to consider is $\xi < r_\epsilon$; both of these values are constant in the integral, but set the limits at a fixed value of z and gives an intuitive separation of the integral as

$$\Sigma(\xi) = 2 \int_0^{\sqrt{r_\epsilon^2 - \xi}} \rho_{sol}(r) + 2 \int_{\sqrt{r_\epsilon^2 - \xi}}^\infty \rho_{NFW}(r) dz. \quad (4.29)$$

The second case corresponds to $\xi \geq r_\epsilon$, and from the relation of r and z , this case will only give real numbers when $r \geq r_\epsilon$. This means that only ρ_{NFW} will contribute to the integral, and the minimum value at which to consider $r_\epsilon = \xi$ corresponds to $z = 0$. For this case, the integral is

$$\Sigma(\xi) = 2 \int_0^\infty \rho_{NFW}(r) dz, \quad (4.30)$$

which curiously reduces to the surface mass density of a NFW profile. This separation can be understood by considering that the integral is done along the line of sight for different values of the impact parameter, ξ , and there is a region where only the NFW tail contributes to the density. Therefore, this defines the normalized surface mass

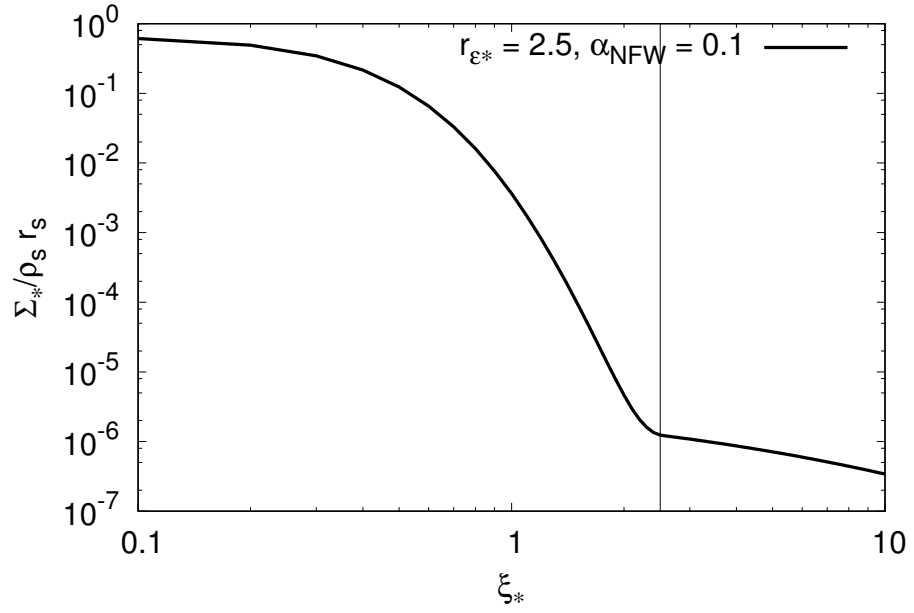


Figure 4.5: Plot of the surface mass density as a function of arbitrarily selected values of $r_{\epsilon^*} = 2.5$ and $\alpha_{\text{NFW}} = 1$. The vertical line shows the transition between the branches for the density. There is a minimum value which is obtained at $\xi_* = 0$.

density as

$$\Sigma_*(\xi_*, r_{\epsilon^*}, \alpha_{\text{NFW}}) = \begin{cases} \int_0^{\sqrt{r_{\epsilon^*}^2 - \xi_*^2}} \frac{dz}{(1+r_*^2)^8} + \frac{r_{\epsilon^*}(1+\alpha_{\text{NFW}}r_{\epsilon^*})^2}{(1+r_{\epsilon^*}^2)^8} \int_{\sqrt{r_{\epsilon^*}^2 - \xi_*^2}}^{\infty} \frac{dz_*}{r_*(1+\alpha_{\text{NFW}}r_*)^2}, & \xi_* < r_{\epsilon^*}, \\ \frac{r_{\epsilon^*}(1+\alpha_{\text{NFW}}r_{\epsilon^*})^2}{(1+r_{\epsilon^*}^2)^8} \int_0^{\infty} \frac{dz_*}{r_*(1+\alpha_{\text{NFW}}r_*)^2} & \xi_* \geq r_{\epsilon^*}, \end{cases} \quad (4.31)$$

where $z_* = \sqrt{r_*^2 - \xi_*^2}$. A plot of the surface mass density for the arbitrarily selected values of $r_{\epsilon^*} = 2.5$ and $\alpha_{\text{NFW}} = 1$ is shown in fig. 4.5. The vertical line shows where the transition happens, and it is clear from the figure the existence of a minimum value given by $\xi_* = 0$. Fortunately, both integrals can be solved analytically to ease the calculations.

For the first branch of eq. (4.31), the soliton profile part of the integral is solved by

following eq. (4.19) with $z_{max} = \sqrt{r_*^2 - \xi_*^2}$

$$\int_0^{\sqrt{r_{\epsilon_*}^2 - \xi_*^2}} \frac{dz}{(1 + r_*^2)^8} = \frac{1}{(1 + \xi_*^2)^{15/2}} \int_0^x \cos^{14} u \, du, \quad (4.32)$$

where

$$\tan x = \left(\frac{r_{\epsilon_*}^2 - \xi_*^2}{1 + \xi_*^2} \right)^{1/2}.$$

The solution of the integral is

$$\int_0^x \cos^{14} u \, du = \frac{429}{2048} x + \frac{1001}{16384} \left[3 \sin(2x) + \sin(4x) + \frac{1}{3} \sin(6x) + \frac{1}{11} \sin(8x) \right. \\ \left. + \frac{1}{55} \sin(10x) + \frac{1}{429} \sin(12x) + \frac{1}{7007} \sin(14x) \right]. \quad (4.33)$$

Taking the case of $r_{\epsilon_*} \rightarrow \infty$ recovers the soliton solution. The NFW part could be solved as it is, but a short-cut can be taken by rearranging the integral by the considering $z_* = r_* \cos \theta$ and $\xi_* = r_* \sin \theta$ as

$$\int_0^{\arcsin x/y} \sin \theta (\sin \theta + x)^{-2} d\theta, \quad (4.34)$$

where $x = \alpha_{\text{NFW}} \xi_*$ and $y = \alpha_{\text{NFW}} r_{\epsilon_*}$. The solution is

$$\int_{\sqrt{r_{\epsilon_*}^2 - \xi_*^2}}^{\infty} \frac{dz}{r_* (1 + \alpha_{\text{NFW}} r_*)^2} = \begin{cases} \frac{1}{x^2 - 1} \left(1 - \frac{\sqrt{y^2 - x^2}}{1 + y} - \frac{2 \operatorname{arctanh} \left[\frac{\sqrt{1 - x^2}}{1 + y + \sqrt{y^2 - x^2}} \right]}{\sqrt{1 - x^2}} \right) & x < 1, \\ \frac{1}{3} \left(1 - \frac{y + 2}{y + 1} \sqrt{\frac{y - 1}{y + 1}} \right) & x = 1, \\ \frac{1}{x^2 - 1} \left(1 - \frac{\sqrt{y^2 - x^2}}{1 + y} - \frac{2 \operatorname{arctan} \left[\frac{\sqrt{x^2 - 1}}{1 + y + \sqrt{y^2 - x^2}} \right]}{\sqrt{x^2 - 1}} \right) & x > 1. \end{cases} \quad (4.35)$$

By setting $x = y$, the NFW solution is recovered.

The second branch of eq. (4.31) is the case of (4.35) with $r_{\epsilon^*} = \xi_*$. with solution

$$\int_0^{\infty} \frac{dz}{r_* (1 + \alpha_{\text{NFW}} r_*)^2} = \begin{cases} \frac{1}{x^2 - 1} \left(1 - \frac{2 \operatorname{arctanh} \sqrt{\frac{1-x}{x+1}}}{\sqrt{1-x^2}} \right) & x < 1, \\ \frac{1}{3} & x = 1, \\ \frac{1}{x^2 - 1} \left(1 - \frac{2 \operatorname{arctan} \sqrt{\frac{x-1}{x+1}}}{\sqrt{x^2-1}} \right) & x > 1. \end{cases} \quad (4.36)$$

Which is the solution given by [7, 122].

The special case of $\xi_* = 0$ can be obtained from the solutions or directly from the integral by just considering $2 \operatorname{arctanh} x = \ln(1+x) - \ln(1-x)$ which gives

$$\int_{r_{\epsilon^*}}^{\infty} \frac{dz}{z (1 + \alpha_{\text{NFW}} z)^2} = \ln \frac{(1 + \alpha_{\text{NFW}} r_{\epsilon^*})}{\alpha_{\text{NFW}} r_{\epsilon^*}} - \frac{1}{(1 + \alpha_{\text{NFW}} r_{\epsilon^*})}. \quad (4.37)$$

This value is important because it allows us to find λ_{cr} for any r_{ϵ} , which helps to establish the minimum condition for strong lensing.

4.5.2 Gravitational Lensing Mass

The mass enclosed inside a cylinder along the line of sight with a radius of the size of the Einstein radius, which is projected to the lens plane, is called the projected mass. This is the mass used for the deflection angle, and except for special cases, it is obtained by numerical integration, but in the case of Wave Dark Matter can be done analytically.

The integral is along the line of sight on the variable z , so it is necessary to integrate over and perform the change of variable $r_* = \sqrt{\xi_*^2 + z_*^2}$. Using the definition of the normalized projected mass which is given by (4.3) and the definition of the surface mass density (4.31), the normalized projected mass is calculated in two different ways. The first case is when $\xi_* < r_{\epsilon^*}$,

$$m(\xi_*) = 4\pi \left[\int_0^{\xi_*} \xi'_* \left(\int_0^{\sqrt{r_{\epsilon^*}^2 - \xi_*'^2}} \frac{dz_*}{(1 + r_*^2)^8} + \int_{\sqrt{r_{\epsilon^*}^2 - \xi_*'^2}}^{\infty} \frac{\rho_{\text{NFW}*} dz_*}{\alpha_{\text{NFW}} r_* (1 + \alpha_{\text{NFW}} r_*)^2} \right) d\xi'_* \right]. \quad (4.38)$$

This gives the following solution,

$$m(\xi_*) = 4\pi \left\{ \frac{1}{14} \left[B(\arctan r_{\epsilon*}) - \frac{B(\arctan q1)}{(1 + \xi_*^2)^{13/2}} + \frac{\sqrt{r_{\epsilon*}^2 - \xi_*^2} - r_{\epsilon}}{(1 + r_{\epsilon}^2)^7} \right] + \frac{\rho_{\text{NFW}*}}{\alpha_{\text{NFW}}^3} \left[\ln \left(\frac{y + \sqrt{y^2 - x^2}}{2(y + 1)} \right) + \frac{y - \sqrt{y^2 - x^2}}{y + 1} + f(x, y) \right] \right\} \quad \xi_* < r_{\epsilon*}, \quad (4.39)$$

were $q1 = \sqrt{(r_{\epsilon*}^2 - \xi_*^2)/(1 + \xi_*^2)}$, $x = \alpha_{\text{NFW}}\xi_*$ and $y = \alpha_{\text{NFW}}r_{\epsilon*}$. whereas that $B(u)$ is the solution of the following integral

$$B(u) \equiv \int_0^u \cos^{12} u' du' = \frac{1}{122880} [27720u + 23760 \sin(2u) + 7425 \sin(4u) + 2200 \sin(6u) + 495 \sin(8u) + 72 \sin(10u) + 5 \sin(12u)], \quad (4.40)$$

and

$$f(x, y) = \begin{cases} \frac{2}{\sqrt{1-x^2}} \operatorname{arctanh} \sqrt{\frac{1-x^2}{1+y+\sqrt{y^2-x^2}}} & x < 1, \\ 1 - \sqrt{\frac{y-1}{y+1}} & x = 1, \\ \frac{2}{\sqrt{x^2-1}} \operatorname{arctan} \sqrt{\frac{x^2-1}{1+y+\sqrt{y^2-x^2}}} & x > 1. \end{cases} \quad (4.41)$$

The second case $\xi_* > r_{\epsilon*}$ has a more complicated arrangement, but the solution is simpler. Considering the condition of ξ_* , the integral is separated as

$$m(\xi_*) = 4\pi \left[\int_0^{r_{\epsilon*}} \xi' \left(\int_0^{\sqrt{r_{\epsilon}^2 - \xi_*^2}} \frac{dz_*}{(1 + r_*^2)^8} + \int_{\sqrt{r_{\epsilon}^2 - \xi_*^2}}^{\infty} \frac{\rho_{\text{NFW}*} dz_*}{\alpha_{\text{NFW}} r_* (1 + \alpha_{\text{NFW}} r_*)^2} \right) d\xi' \right] + 4\pi \left[\int_{r_{\epsilon*}}^{\xi_*} \xi' \left(\int_0^{\infty} \frac{\rho_{\text{NFW}*} dz_*}{\alpha_{\text{NFW}} r_* (1 + \alpha_{\text{NFW}} r_*)^2} \right) d\xi' \right]. \quad (4.42)$$

Changing the order of integration appropriately and performing only the inner integral, it can be rearranged to be

$$m(\xi_*) = 4\pi \left\{ \int_0^{r_{\epsilon*}} \left[\frac{1}{(1 + z_*^2)^7} - \frac{1}{(1 + r_{\epsilon*}^2)^7} \right] dz_* \right\} + 4\pi \left\{ \int_0^{\pi/2} \left[\ln \frac{\sin \theta + x}{\sin \theta (1 + y)} + \frac{y}{1 + y} - \frac{x}{\sin \theta + x} \right] \sin \theta d\theta \right\}. \quad (4.43)$$

were $x = \alpha_{\text{NFW}}\xi_*$, $y = \alpha_{\text{NFW}}r_{\epsilon^*}$ and $\alpha_{\text{NFW}}z_* = x \cot \theta$. The mass for this case is

$$m(\xi_*) = 4\pi \left\{ \frac{1}{14} \left[B(\arctan r_{\epsilon^*}) - \frac{r_{\epsilon^*}}{(1+r_{\epsilon^*})^7} \right] + \frac{\rho_{\text{NFW}^*}}{\alpha_{\text{NFW}}^3} \left[\ln \left(\frac{1}{(y+1)} \right) + \frac{y}{y+1} + m_{\text{NFW}}(x) \right] \right\} \quad \xi_* > r_{\epsilon^*}, \quad (4.44)$$

where the definition of $B(u)$ is given in (4.40), and

$$m_{\text{NFW}}(x) = \begin{cases} \frac{2}{\sqrt{1-x^2}} \operatorname{arctanh} \sqrt{\frac{1-x}{1+x}} + \ln \left(\frac{x}{2} \right) & x < 1, \\ 1 + \ln \left(\frac{1}{2} \right) & x = 1, \\ \frac{2}{\sqrt{x^2-1}} \arctan \sqrt{\frac{x-1}{1+x}} + \ln \left(\frac{x}{2} \right) & x > 1, \end{cases} \quad (4.45)$$

which is the normalized solution of the NFW profile as can be compared with (2.28).

Figures showing hypothetical sources being lensed using the previous lens masses are left for appendix B. As mentioned at the beginning of the chapter the lensing functions for Wave Dark Matter are derived for the first time for this work, as known at the time of writing, and their analysis as an introduction for their use to describing the model as a lens is in the next chapter.

Chapter 5

Galaxy analysis

The chapter describes some properties of the WaveDM model as a lensing system, and it helps to set some characteristic through analysis of a selected number of galaxies which are presented in the SLACS surveys [40, 4, 12, 128, 59, 39, 40, 40, 13, 5], to compare how the model can represent or describe observed properties of strong lenses. The parameters to fit in the analysis will be different considering the parts of the model. In the case of the soliton, the parameter will be r_s through its relation with θ_{*E} . The full profile will fit the parameters r_{ϵ^*} and α_{NFW} . For the rest of the chapter the dependence of the parameters will be made more explicit by properly representing $\Sigma_*(\xi_*) \rightarrow \Sigma_*(\xi_*, r_{\epsilon^*}, \alpha_{\text{NFW}})$ and $m(\xi_*) \rightarrow m(\xi_*, r_{\epsilon^*}, \alpha_{\text{NFW}})$.

5.1 Matching properties

In the previous chapter was presented the WaveDM model for lensing were it was made clear that it is composed of two components: the soliton core and a NFW tail. Now several properties of this model will be presented that will help us to use it for characterization of WaveDM.

It is first important to notice from eq. (4.27) that it is a quadratic function, so the profile intersection could happen in two values of the matching radius, r_{ϵ^*} . The second point is that there is a possibility for a certain combination of parameters where neither

profile touch. This can be appreciated in fig. 5.1. The figure shows several values of ρ_{NFW^*} for the fixed value of $\alpha_{\text{NFW}} = 1$. This means that the matching radius is different in each case. It is clear from the figure that there are some combinations of parameters which make the transition discontinuous, so to avoid this problem it is necessary ensure the continuity. Figure 5.2 shows ρ_{NFW^*} as a function of r_{ϵ^*} considering

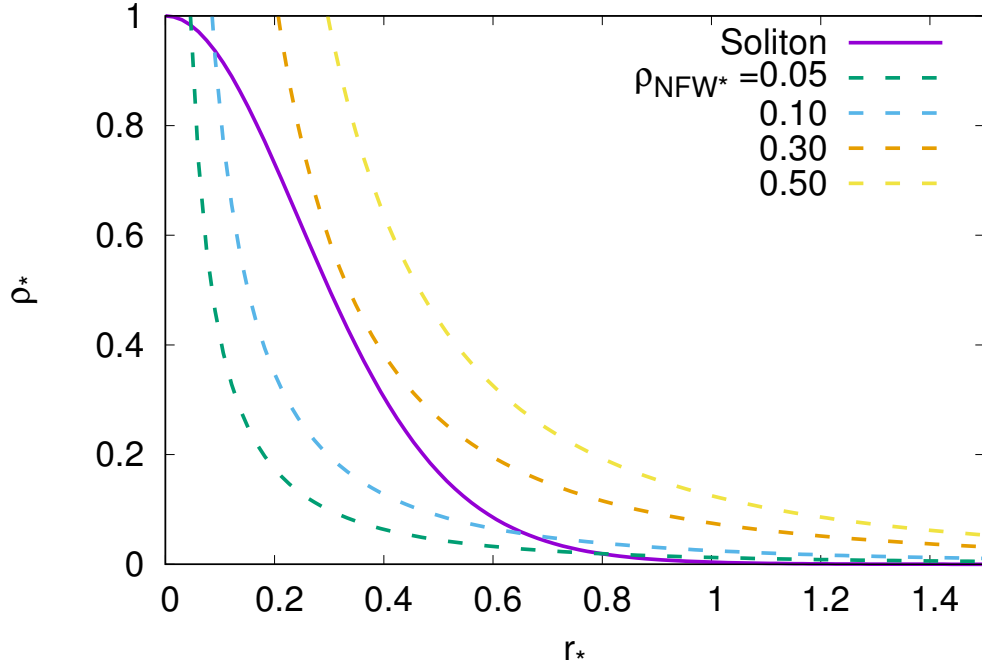


Figure 5.1: The normalized density profile of the soliton together with different examples of the normalized NFW profile. It is shown here that there are at most two values of the matching radius r_{ϵ^*} , which depend on the given values of the normalized density ρ_{NFW^*} and α_{NFW} (here $\alpha_{\text{NFW}} = 1$ is taken).

continuity through eq. (4.27c); it is clear the existence of a peak value which can be used to break the hidden degeneracy of eq. (4.27); this will be called $r_{\epsilon^*,\text{max}}$. To find this maximum, makes it necessary to evaluate the derivative of eq. (4.27c) and find the value which makes it zero,

$$\left. \frac{\partial \rho_{\text{NFW}^*}}{\partial r_{\epsilon^*}} \right|_{r_{\epsilon^*,\text{max}}} = 0. \quad (5.1)$$

This straight forward calculation shows that $r_{\epsilon^*,\max}$ is a root of the cubic equation

$$13\alpha_{\text{NFW}}r_{\epsilon^*,\max}^3 + 15r_{\epsilon^*,\max}^2 - 3\alpha_{\text{NFW}}r_{\epsilon^*,\max} = 1. \quad (5.2)$$

The exact solution depends of the value of α_{NFW} , which makes necessary to calculate it every time it changes. Nevertheless, it is possible to find a range by setting the limiting values of $0 \leq \alpha_{\text{NFW}} \leq \infty$. The solutions of these limits are

$$\lim_{\alpha_{\text{NFW}} \rightarrow 0} r_{\epsilon^*,\max} = (1/\sqrt{15}), \quad (5.3a)$$

$$\lim_{\alpha_{\text{NFW}} \rightarrow \infty} r_{\epsilon^*,\max} = (\sqrt{3/13}). \quad (5.3b)$$

In fig. 5.2, ρ_{NFW^*} is shown as a function of r_{ϵ^*} for several values of α_{NFW} . The limiting range $0.25 < r_{\epsilon^*,\max} < 0.48$ can be seen by the two vertical lines.

Because the purpose of using the WaveDM model is to compose the majority of the content of the dark matter, it is reasonable to choose the soliton component to form the majority of the inner part of the profile. This makes a clear choice to the place for matching the profiles. As stated before, there are two possible values for the matching. By the previous reasoning, it is preferable to choose the farthest radius possible; this is done by setting the constraint $r_{\epsilon^*} \geq r_{\epsilon^*,\max}$.

There is a second consideration for the combination of α_{NFW} and r_{ϵ^*} and their relation with λ_{cr} . Following its definition in eq. (4.8), the value we need to search is

$$\Sigma_*(0, r_{\epsilon^*}, \alpha_{\text{NFW}}) = 2 \left[\int_0^{r_{\epsilon^*}} \frac{dz}{(1+z^2)^8} + \frac{r_{\epsilon^*}(1+\alpha_{\text{NFW}}r_{\epsilon^*})^2}{(1+r_{\epsilon^*}^2)^8} \int_{r_{\epsilon^*}}^{\infty} \frac{dz}{z(1+\alpha_{\text{NFW}}z)^2} \right], \quad (5.4)$$

where the solutions for both integrals can be found in eqs. (4.33) and (4.37). A comparison between the soliton and the combination of several α_{NFW} can be seen in fig. 5.3. It is clear from the figure how λ_{cr} decreases by changing the value of α_{NFW} , nevertheless, this only happens for lower values of r_{ϵ^*} and as the transition point increases there is a moment where it returns to the case of the soliton limit $r_{\epsilon^*} \rightarrow \infty$, $\lambda_{\text{cr}} \simeq 0.48$. This can be understood very clearly by realizing how increasing the transition radius affects the contribution of the NFW tail by reducing it, and the behaviour of the complete profile is dominated by the soliton, so its properties will match this case. Having this

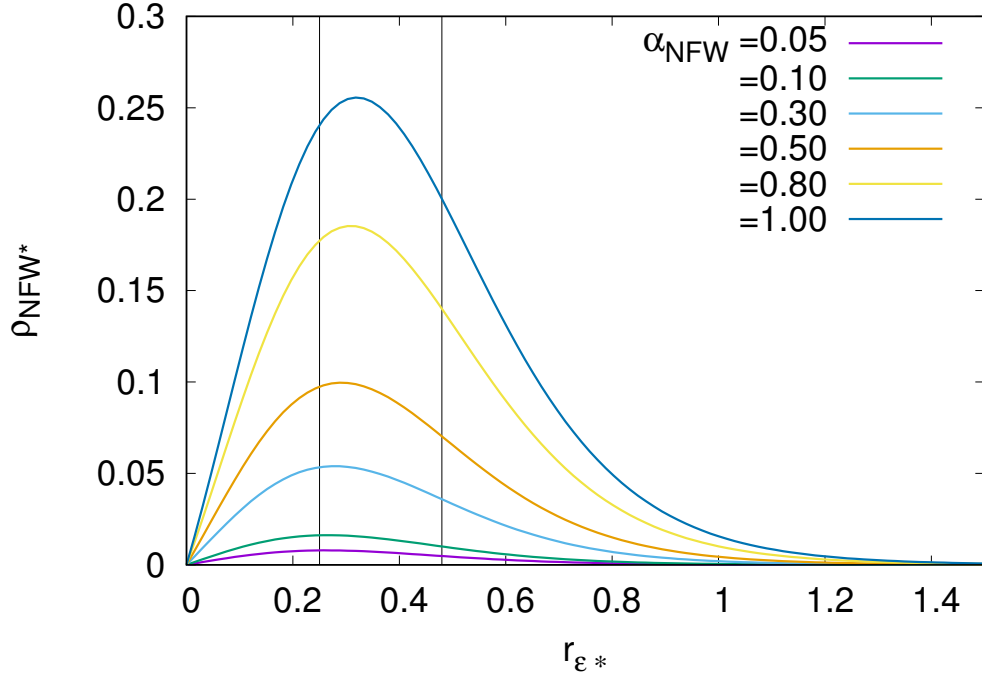


Figure 5.2: The normalized density ρ_{NFW} as a function of the matching radius r_{ϵ^*} , for different values of α_{NFW} , as indicated by eq. (4.27c). Notice that there are two possible values of r_{ϵ^*} for any given value of ρ_{NFW^*} , except for the maximum value of the latter. The vertical lines represent the minimum and maximum possible values for the peak of ρ_{NFW^*} for the range $0 \leq \alpha_{\text{NFW}} \leq \infty$.

in mind will help to realize that once the transition happens at large radii the soliton will be enough to describe adequately the lens. This explains why λ_{cr} agrees with the value of the soliton at a high r_{ϵ^*} . The constraint $r_{\epsilon^*} \geq r_{\epsilon^*\text{max}}$ is taken into account when plotting the different valued lines, and the value $r_{\epsilon^*} = 1$ is emphasized because it represents a decrease in the profile where the overall contribution of the NFW tail becomes minimal and possibly overlook. This will be discussed in the following section. The last point to emphasize is that the total mass enclosed inside a sphere of radius r is given by

$$M(r) = c(m_a, r_s) \times \left[\int_0^{r_{\epsilon^*}} \frac{dx x^2}{(1+x^2)^8} + \frac{r_{\epsilon^*} (1 + \alpha_{\text{NFW}} r_{\epsilon^*})^2}{(1+r_{\epsilon^*}^2)^8} \int_{r_{\epsilon^*}}^{r^*} \frac{dx x}{(1 + \alpha_{\text{NFW}} x)^2} \right], \quad (5.5)$$

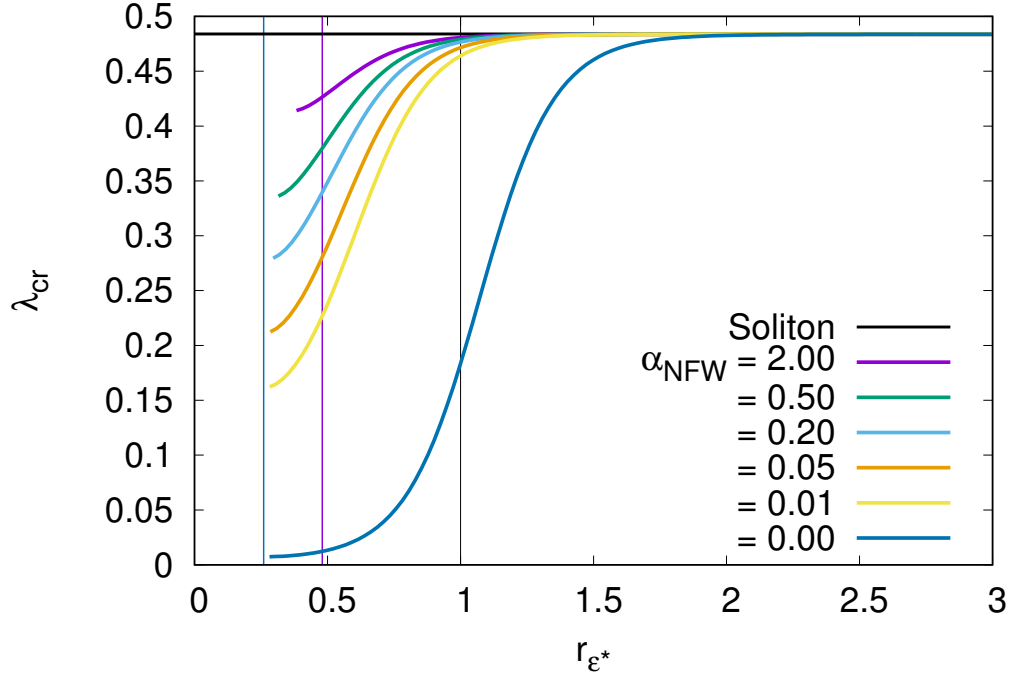


Figure 5.3: The critical value λ_{cr} as a function of r_{ϵ^*} . for different values of α_{NFW} . The soliton alone value of $\lambda_{\text{cr}} \simeq 0.48$ is compared with several different α_{NFW} . The constraint $r_{\epsilon^*} \geq r_{\epsilon^*\text{max}}$ is considered.

where

$$c(m_a, r_s) = 3 \times 10^{13} M_{\odot} \left(\frac{m_a}{10^{-22} \text{ eV}} \right)^{-2} \left(\frac{r_s}{\text{pc}} \right)^{-1} \quad (5.6)$$

is a constant which depends of the particle mass, m_a , and the characteristic radius of the soliton, r_s . In general, the mass should increase as $r \rightarrow \infty$, but if we consider the soliton case where $r_{\epsilon^*} \rightarrow \infty$, the total mass contribution M_s is [46, 70, 22]

$$\frac{M_s}{10^{11} M_{\odot}} = 7.7 \left(\frac{m_a}{10^{-22} \text{ eV}} \right)^{-2} \left(\frac{r_s}{\text{pc}} \right)^{-1}. \quad (5.7)$$

It should be understood that the total mass $M(r)$ which is the combined profile and M_s do not need to agree and in principle they should satisfy $M(r) \geq M_s$. Nevertheless, the contribution of the soliton to the complete profile should be expected to be $M(r_{\epsilon^*}) \simeq M_s$ in the majority of the cases.

From here onwards it will be important to differentiate between two meanings. In referring to the total mass of the soliton, or soliton mass, this will be related to the value

obtained in eq.(5.7). Referring to the particle mass or boson mass will mean m_a . This statement is to avoid differences during the description and clear possible confusions. The different definitions stated in this section will an important consideration at the moment of choosing limits for the analysis of some lenses.

5.2 Data analysis

The following section will describe the parameter estimation done using the selected sub-sample of galaxies for particular conditions in order to assess how well the soliton profile and properly WaveDM characterize the Dark Matter component within a the selected galaxies. This is done in order to obtain some insight about the properties of the model, and its usefulness for lensing.

5.2.1 Galaxy sample

For simplicity, a selection of galaxies is taken from the Sloan Lens ACS Survey(SLACS) compilation of papers [12, 128, 59, 40, 11, 39, 13, 4, 5, 84]. To take a simple approach the criteria for selection were to consider only galaxies which had less than 50% fractional luminous matter. This is to just take into consideration galaxies in which the content of Dark Matter is more prominent. The selected galaxies and their important characteristics were taken from [40, 11, 4] and the data used are presented in table 5.1. It is important to notice that, while there are several values in the table, the only parameter that we take in consideration into the model is the Einstein radius R_E because the only interest is to study strong lensing cases. Nevertheless, the actual observable is Einstein angle θ_E , which is obtained by matching caustic lines to the observed image, this process has been proven to be model independent [57]. Afterwards, the physical distance is obtained by $R_E = D_{OL}\theta_E$, where D_{OL} is the angular diameter distance from the observer to the lens, and it is dependent of the cosmology [48]. The values in table 5.1 are obtained using the same cosmology as the for the SLACS papers which is a Friedmann-Robertson-Walker (FRW) cosmology with matter-density

Name	$f_{*,\text{Ein}}^{\text{Salp}}$	z_{lens}	z_{source}	$d_{OS}/(d_{OL}d_{LS})$	R_E
J0008-0004	0.50 ± 0.16	0.44	1.192	6.609565	6.59
J0935-0003	0.35 ± 0.05	0.347	0.467	18.04391	4.26
J0946+1006	0.46 ± 0.13	0.222	0.609	9.700301	4.95
J1143-0144	0.46 ± 0.10	0.106	0.402	14.9161	3.27
J1306+0600	0.47 ± 0.08	0.173	0.472	11.66306	3.87
J1318-0313	0.42 ± 0.08	0.24	1.3	7.215974	6.01

Table 5.1: List of selected galaxies from SLACS. These were selected because they have a fraction of luminous matter of 0.5 or less; see the values in the second column. Column (1) gives the label of the galaxies within the SDSS catalog, column (2) indicates the fraction of luminous matter and dark matter. Column (6) lists the measured Einstein radius in units of kpc.

parameter $\Omega_M = 0.3$, vacuum energy-density parameter $\Omega_\Lambda = 0.7$, and Hubble parameter $H_0 = 70 \text{ km s}^{-1} \text{ Mpc}^{-1}$ [11]. An error of 5% on the measured value of θ_E is adopted for all the galaxies [40].

5.2.2 Soliton core

Before analysing the complete WaveDM profile, it is recommendable to take as a first approach the soliton core alone because this will give some insight on the behaviour of the core which is much simpler in its description. This approach could be considered

the special case of the limit $r_{\epsilon^*} \rightarrow \infty$. The opposite limit $r_{\epsilon^*} \rightarrow 0$ does not need to be considered because this represents the case of an NFW profile which has been studied extensively previously [138, 7, 122]. The majority of the equations to be used are already obtained in section 4.4.

Following (4.21), it is possible to notice there are the special cases $m_*(0) = 0$ and the other is the limit $m_*(\infty) = 2/(13\lambda_{\text{crit}})$. This is a clear indication that for a sufficiently large angle the surface mass could be considered almost a constant. Before doing any analysis, it is useful to rewrite some equations in a clearer form. If we combine eqs. (4.4), (4.5), (4.16) and taking into account that the value to search is going to be the Einstein angle, which is defined by $\theta_{*E} \equiv R_E/r_s$, the lens equation can be recast as

$$m_{a22}^{-2} \theta_{*E} m_*(\theta_{*E}, \alpha_{\text{NFW}}, r_{\epsilon^*}) = \frac{1}{2.4 \times 0.57} \frac{d_{OS}}{d_{OL}d_{LS}} h \left(\frac{R_E}{\text{kpc}} \right)^3, \quad (5.8)$$

where $m_{a22} \equiv m_a/10^{-22}\text{eV}$ is set for convenience.

This representation of the lens equation has several advantages. First, it makes a clear distinction between the parameters of the model, on the left-hand side, and the information from the observables, on the right-hand side. The second advantage is the dependence of the parameters ρ_s and r_s is clearly hidden in the normalization. Another, which might not be so clear, is that it takes into account the minimum value of λ by setting directly the information of the geometry of the system. This helps to avoid searching first for λ values which satisfy the system because it is already integrated into the equation. In the case of the soliton, there is no dependence of α_{NFW} nor r_{ϵ^*} .

Now, it is important to have a mention for the axion or boson mass m_a . While in principle it is possible to determine the range of values which satisfy the data while considering m_a as a free parameter, it must be recalled that the boson mass is a fundamental physical parameter of the model and should be common among the different galaxies. Therefore, it should not be allowed to vary freely, and during the parameter estimation, it will be fixed beforehand considering an expected range from previous estimations of other studies [96, 105, 130].

Before presenting the analysis for the galaxies of the selected sample, it will be

convenient to have a basic understanding of how the solutions are going to be obtained. By means of eq. (5.8), the right-hand side is going to be compared for the parameters of each galaxy with the solution given for different values of θ_{*E} . An example of the procedure can be seen in fig. 5.4. The dashed lines represent the inferred values from the observations which correspond to the right-hand side of the equation, and do not vary with the angle. The crossing points will give the allowed range of values as the example for $m_{a22} \approx 0.02$, this has an angular Einstein radius range of $5 < \theta_{*E} < 10$. It can be later translated into an allowed range for the soliton radius, r_s , by applying the definition of θ_{*E} .

It must be noted that it is always possible to find a solution that matches, of course, this comes by selecting larger values of θ_{*E} . Nevertheless, careful consideration needs to be taken for this statement. For the selected sample of values, there will be a value of boson mass for which the Einstein angle will be significantly too large and another too small. These two cases will in theory satisfy the equation, but for practical considerations should be inadequate. This gives another reason to not allow the value of m_a to vary freely.

Summarizing, given the only observable constraint, the boson mass is fixed, and the parameter θ_{*E} is searched to give a consistent value for the best-fit for r_s , and from it, ρ_s can be obtained.

The information on the parameters is obtained by introducing the equations and required information into the Multinest code [36] to carry out the parameter search for each individual galaxy of the sample. For the case of the soliton only one parameter is used on the search, and an example for the translated r_s output for galaxy J0008-0004 is shown in fig. 5.5. The final choice of values for the boson mass were $m_{a22} = 0.1, 1, 10$ by considering the constraints found in other works with $m_a < 1 \times 10^{-21} \text{eV}$ [70, 51]. The figures show the constraint only over one parameter, θ_{*E} , which is the only free parameter in eq. (5.8) where the mass is given by eq. (4.21); it is translated to the corresponding value of r_s by $\theta_{*E} \equiv R_E/r_s$. The comparison of the results obtained from the selected sample of galaxies are summarized in table 5.2.

From the results it is important to notice the consistency in the soliton mass which

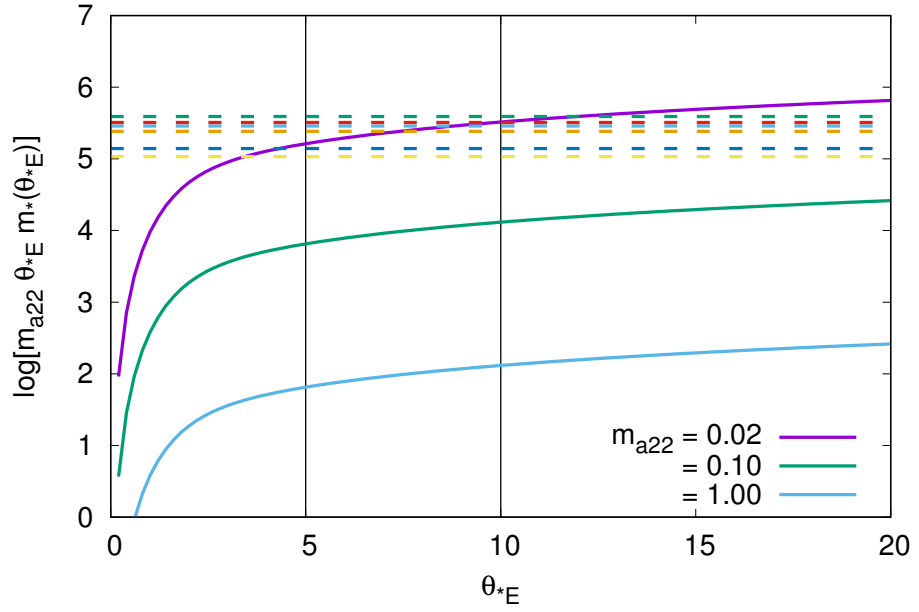


Figure 5.4: Illustration of the use of eq. 5.8 to constrain the parameters for the soliton. The curves are shown for selected values of m_{a22} and how the left-hand side varies as a function of the Einstein angle. The vertical lines represent the range of values which satisfy the different samples.

is conserved along the different values. This is not a surprise given that the mass contained inside of the Einstein radius is fixed by the observable, R_E , and does not change for a galaxy. This only means that for a specific Einstein radius, every combination of possible parameters will share the same soliton mass. Keeping J0008-0004 as an example, its average soliton mass which is defined by eq. (5.7) is $M_s \simeq 3.44 \times 10^{11}$. As mentioned before, the value is conserved regardless of the different parameters. This is not the true in the case of the density, given by eq. (4.16). The conservation of the soliton mass implies a change of density according to the different characteristic radii, which is observed in table 5.2. There is clearly an inverse relation between r_s and ρ_s .

Considering the results obtained, and comparing the radius and the total mass, it is possible to notice that the soliton is a very compact object, even though it is possible to satisfy the conditions for lensing and is consistent with the observables. This is not necessarily a problem by itself, but taking into account the expected size of the galaxy

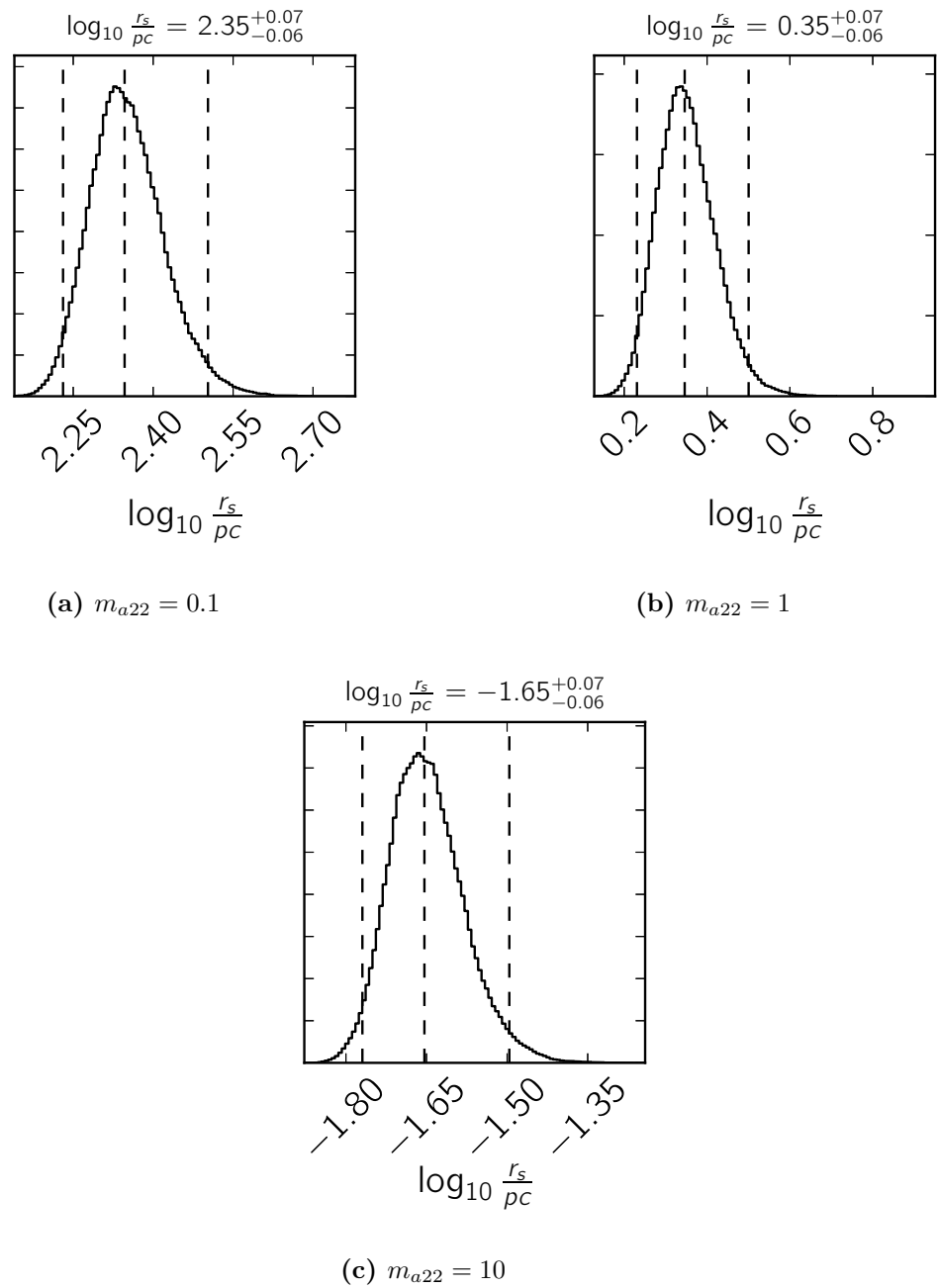


Figure 5.5: Parameter constraint for the soliton case of galaxy J0008-0004. Only one parameter is represented, for the three selected values of boson mass.

it is a feature that is not desirable. The problem arises from the combination of the high density and the small radius. The rotation curves of spiral galaxies can give some insight about distribution of Dark Matter which is dominant as the radius increases,

	$m_{a22} = 10$	$m_{a22} = 1$	$m_{a22} = 0.1$
Galaxy	$\log_{10}(r_s/\text{pc})$		
J0008-0004	$-1.65^{+0.07}_{-0.06}$	$0.35^{+0.07}_{-0.06}$	$2.35^{+0.07}_{-0.06}$
J0935-0003	$-1.71^{+0.07}_{-0.06}$	$0.29^{+0.07}_{-0.06}$	$2.29^{+0.07}_{-0.06}$
J0946+1006	$-1.57^{+0.07}_{-0.06}$	$0.43^{+0.07}_{-0.06}$	$2.43^{+0.07}_{-0.06}$
J1143-0144	$-1.40^{+0.07}_{-0.06}$	$0.60^{+0.07}_{-0.06}$	$2.60^{+0.07}_{-0.06}$
J1306+0600	$-1.44^{+0.07}_{-0.06}$	$0.56^{+0.07}_{-0.06}$	$2.56^{+0.07}_{-0.06}$
J1318-0313	$-1.61^{+0.07}_{-0.06}$	$0.39^{+0.07}_{-0.06}$	$2.39^{+0.07}_{-0.06}$

Table 5.2: The values of the soliton radius in the logarithmic scale $\log_{10}(r_s/\text{pc})$ obtained from the fits to the indicated galaxies, for three different values of the boson mass m_a .

but in our case we have elliptical galaxies. Even that they are not directly comparable, it would be expected to have a similar or close distribution of Dark Matter, but in the our case the majority of the values presented in table 5.2 there is a big contrast with the biggest amount of mass in the galaxy enclosed inside a small radius. This would be an unexpected concentration of mass, if several of the values for the soliton are considered. To give a point of reference, for the case of galaxy J0008-0004 the mass inside the Einstein radius is $M_{\text{Eins}} \approx 3.1 \times 10^{11} M_{\odot}$, and according to table 5.1 the ratio between luminous and dark matter is 0.5, so they share the same amount of mass, but if we compare both radii, the effective radius for the luminous part is $r_e \approx 9.6\text{kpc}$ [11, 5], and the soliton would have, in the case of $m_{a22} = 1$, a radius of $r_s \approx 2.4\text{pc}$. This implies a extremely dense centre, and this is not usually observed in galaxies.

Anyway, because the only measurement to satisfy is the Einstein radius, it is possible to find a solution for the lens. But considering that the lens equation can be solved by a point particle, it is not surprising to find the soliton to be this compact. This gives

	$m_{a22} = 10$	$m_{a22} = 1$	$m_{a22} = 0.1$
Galaxy	$\log_{10}(\rho_s/M_{\odot}\text{pc}^{-3})$		
J0008-0004	$16.98^{+0.28}_{-0.24}$	$10.98^{+0.28}_{-0.24}$	$4.98^{+0.28}_{-0.24}$
J0935-0003	$17.22^{+0.28}_{-0.24}$	$11.22^{+0.28}_{-0.24}$	$5.22^{+0.28}_{-0.24}$
J0946+1006	$16.66^{+0.28}_{-0.24}$	$10.66^{+0.28}_{-0.24}$	$4.66^{+0.28}_{-0.24}$
J1143-0144	$15.98^{+0.28}_{-0.24}$	$9.98^{+0.28}_{-0.24}$	$3.98^{+0.28}_{-0.24}$
J1306+0600	$16.14^{+0.28}_{-0.24}$	$0.14^{+0.28}_{-0.24}$	$4.14^{+0.28}_{-0.24}$
J1318-0313	$16.82^{+0.28}_{-0.24}$	$10.82^{+0.28}_{-0.24}$	$4.82^{+0.28}_{-0.24}$

Table 5.3: The values of the soliton density in the logarithmic scale $\log_{10}(\rho_s/M_{\odot}\text{pc}^{-3})$ obtained from the results of the radius from the different galaxy fits. The inverse relationship between the radius and density is clear, as for the largest radii, they possess smallest density, which preserves the soliton mass constant for the galaxy.

a valuable lesson. The soliton can fulfil the lensing requirements, formally speaking, even though it is not completely adequate when taking into account other observed properties that the galaxies may have. In the next section, this will be addressed by considering the complete profile which includes a NFW outskirts, which will relax the distribution of dark matter.

5.2.3 Complete profile

The consideration of the soliton core being the complete contribution for the dark matter content of the galaxy is a reasonable one, but it comes with several inconsistencies between the density and the size of the possible object. This means that it needs a way to alleviate the problem. This is done by considering a complete profile which includes a soliton core + NFW outskirts as presented in eq. (4.23).

Taking into account the normalization used in section 4.5, there are three free parameters: $(m_a, r_{\epsilon^*}, \alpha_{\text{NFW}})$. Unfortunately, the parametrization used helps to simplify

the derivations, but hides the dependence in r_s . For the soliton case, there was a simple relation with the Einstein angle θ_E , but now this is not so simple because it is desired to avoid the soliton completely filling the dark matter of the halo, which will produce a case similar to just having a soliton. To avoid this, the approach will be by

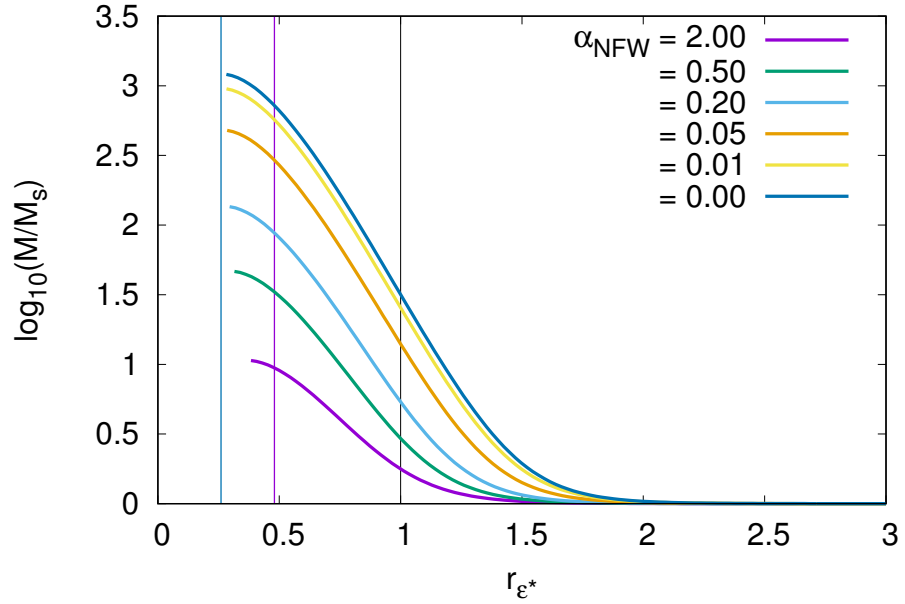


Figure 5.6: Total mass M normalized by terms of the soliton mass M_s . It is important to notice that M can be up to three orders of magnitude compared with the the soliton mass. This is obtained just by integration of eq. (5.5) with an upper limit of $r_* = 20$. The black line represents $r_{e*} = 1$, and the blue and purple lines are set as the range $0.25 < r_{e*,max} < 0.48$.

controlling the soliton mass contribution given by M_s in the analysis. As well as with the soliton only case, the axion mass is set for three particular values of $m_{a22} = 0.1, 1, 10$, and using the relation established by eq. (5.7), it is possible to set the values of r_s by controlling the total amount of mass the soliton will contribute. Then it will be set $\log(M_s/M_\odot) = 11.5, 10.5, 9.5, 8.5, 7.5$, and from this set all the values of r_s will be obtained. This should avoid the overcompensation of the soliton. This only leaves to set the priors for the values of r_{e*} and α_{NFW} .

An uniform prior for the parameter is chosen between the following ranges: $\alpha_{\text{NFW}} = [0 : 10]$ where the lower limit is simply the lowest value possible by the way it was defined. The upper limit is suggested by figures 5.1, 5.2, and 5.3. and $r_{\epsilon^*} = [r_{\epsilon^*,max} : 10]$. The value of $r_{\epsilon^*,max}$ is found by solving the cubic equation (5.2) and the upper limit is suggested by the same figures as α_{NFW} . An important difference is the sampled value for θ_{*E} , which in the soliton case was used directly due to only existing dependence of r_s ; nevertheless, for the complete profile, there are more parameters involved, due to this and to avoid the possibility of using the information twice, its values will be obtained by sampling from a Gaussian distribution defined by

$$\theta_{*E}(p) = \theta_{*Em} + \sigma\sqrt{2}\text{erf}^{-1}(2p - 1), \quad p \in (0, 1), \quad (5.9)$$

where $\theta_{*Em} \equiv R_E/r_s$ corresponds to the mean of the distribution by the use of the observed value for the Einstein radius, and the previously determined value of r_s . The error is defined as $\sigma = 0.05 * \theta_{*Em}$. The value of p is a random number generated from a an uniform distribution inside the interval $[0, 1]$ which is used as a seed for the Gaussian. The implementation of the inverse error function is described in [137] as

$$\text{erf}^{-1} \approx \left[-\frac{2}{\pi a} - \frac{\ln(1 - x^2)}{2} + \sqrt{\left(\frac{2}{\pi a} + \frac{\ln(1 - x^2)}{2} \right)^2 - \frac{1}{a} \ln(1 - x^2)} \right], \quad (5.10)$$

where $a = 0.14$. Through this Gaussian sampling will be the only way θ_{*E} will be used for the actual fitting during the analysis.

The contribution of the soliton mass is fixed inside the Einstein radius, but this could produce a saturation of the NFW outskirts due to the need to provide almost 3 orders of magnitude compared with the soliton. This feature can be observed in fig. 5.6. This is the total mass enclosed inside the radius, $r_* = 20$, which is obtained by directly integrating eq. (5.5), but with the normalization of M_s . The blue and purple vertical lines represent the range of solutions for $r_{\epsilon^*,max}$. Every minimum value for r_{ϵ^*} will lie in between these lines. The black line corresponds to $r_{\epsilon^*} = 1$. It is possible to observe the range $0 \leq \alpha_{\text{NFW}} < 2$. The lower limit corresponds to the maximum ratio the total halo will have compared with the soliton core, meanwhile the upper limit, it is a set

value establishing the condition that the mass of the halo should not be smaller than the soliton core mass.

This excess in order of magnitude, it is a feature completely desired, so to alleviate this problem, it would be reasonable to include a first order approximation of the luminous or baryonic matter as a constant quantity. This can be done by modelling it as a point mass included in the projected mass. This is done in eq. (4.1) by adding the extra mass as

$$m'(\theta) = M(\theta) + M', \quad (5.11)$$

where $M(\theta)$ corresponds to the dark matter component represented by complete profile soliton core + NFW given by eq. (4.23), and the constant value $M' = f_{*,\text{Ein}} M_{\text{Ein}}$ is simply the baryonic contribution inside the Einstein radius. $f_{*,\text{Ein}}$ is the fraction of luminous matter inside the Einstein radius, and M_{Ein} is the mass enclosed inside the Einstein radius. These two values are obtained from the data in table 5.1.

The new projected mass needs to be properly normalized to be used to obtain the best fit. This gives the new dimensionless projected mass as

$$m'_*(\theta_*, \alpha_{\text{NFW}}, r_{\epsilon*}) = m_*(\theta_*, \alpha_{\text{NFW}}, r_{\epsilon*}) + M'_*, \quad (5.12)$$

where

$$M'_* = 0.3208 f_{*,\text{Ein}} \left(\frac{M_{\text{Ein}}}{M_s} \right). \quad (5.13)$$

Introducing the mass in eq. (5.8) and using M_s instead by means of eq. (5.7), the form to be used for the analysis will be

$$\frac{M_s}{M_\odot} m'_*(\theta_{*E}, \alpha_{\text{NFW}}, r_{\epsilon*}) = \frac{7.7 \times 10^8}{2.4 \times 0.57} \frac{d_{OS}}{d_{OL} d_{LS}} h \left(\frac{R_E}{\text{kpc}} \right)^2. \quad (5.14)$$

This will be the main equation to solve. The interesting feature from the arrangement comes from the separation from observables and theoretical values. The left hand side of the equation only considers all the theoretical values from the model while the right hand side are the observables, which includes the distances from the lens system, the Hubble parameter and the measured Einstein radius.

The parameter estimation for several galaxies will be carried out using the Multinest code, which as mentioned in section 3.5, is a nested sampling algorithm. The original

reason to choose this code was due to the model having in total 5 parameters, but due to the normalization it was reduced to only search for 2, and the implementation was already done, so it was simpler to use it.

The implementation for the complete profile is done with the following procedure:

1. Priors are set as $\alpha_{\text{NFW}} = [0 : 10]$, and the value of $r_{\epsilon^*, \text{max}}$ is calculated from equation (5.2) which sets the lower limit of $r_{\epsilon^*} = [r_{\epsilon^*, \text{max}} : 10]$; as mentioned previously, the range would be $0.25 < r_{\epsilon^*, \text{max}} < 0.48$.
2. The right hand side of eq. (5.14) is calculated with the data from the galaxies found in table 5.1 an assigned to a variable x_{data} .
3. The left hand side of eq. (5.14) is obtained by using the prior values; the soliton mass can be assigned directly or obtained from eq. (5.7). This is assigned to x_{model}
4. The previous values are used for the likelihood function:

$$\mathcal{L} = \frac{1}{\sqrt{2\pi}\sigma} \exp \left[-\frac{1}{2} \frac{(x_{\text{data}} - x_{\text{model}})^2}{\sigma^2} \right] \quad (5.15)$$

which is used by Multinest for the estimation.

5. The process is repeated until the parameters α_{NFW} and r_{ϵ^*} are best-fitted.

The main results can be summarized by observing the posteriors obtained from two of the galaxies, J0008-0004 and J0935-0003. Although the results for the other galaxies will also be shown, these two were selected in particular due to them containing the smallest and largest fraction of dark matter respectively.

To begin with the description of the results, it is adequate to start with a selected value, $\log(M_s/M_\odot) = 11.5$. This particular choice is a free one for the soliton. In other words, this value has the peculiarity that by observing the point 2 on the procedure list, it is close related to allow free of choice to variables of eq. (5.7). Furthermore, this means that almost the totality of the Dark Matter contribution is proportioned by the

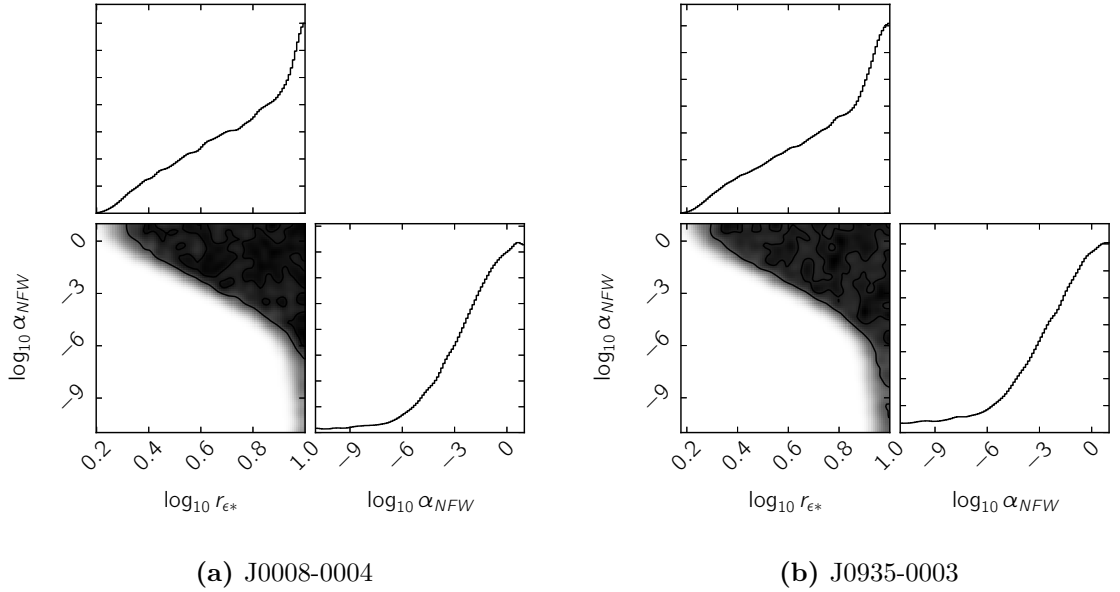


Figure 5.7: Posteriors for galaxies J0008-0004 and J0935-0003. On the graph there is a clear delimitation of the area which the parameters can obtain to satisfy the lens mass given for the galaxies. The clear line shows where the soliton dominates and the rest gray area are the values for the NFW tail whose contribution is negligible.

soliton mass as $M_s \approx M(r)$. For lower values of soliton mass this is totally selected as mentioned previously.

In principle, it is allowed to cover almost the entirety of the mass in the profile, but it is not restricted to it, nevertheless the result from the parameter estimation tells that not only it is allowed, but it is preferred.

In figure 5.7, it can be seen the posteriors for galaxies J0008-0004 and J0935-0003 for a selected axion mass of $m_{a22} = 10$ where it is easy to appreciate that there is a clear limit of the allowed values to be taken. The shaded region shows the area allowed to take values that will represent the mass of the lens, this region nevertheless does not give a definite constraint on the values, but it gives an understanding of the reason for this.

Looking carefully, the minimum region allowed starts from $r_{\epsilon^*} > 1$, taking from figures 5.1 and 5.2, this shows values where the dominant part of the profile is the

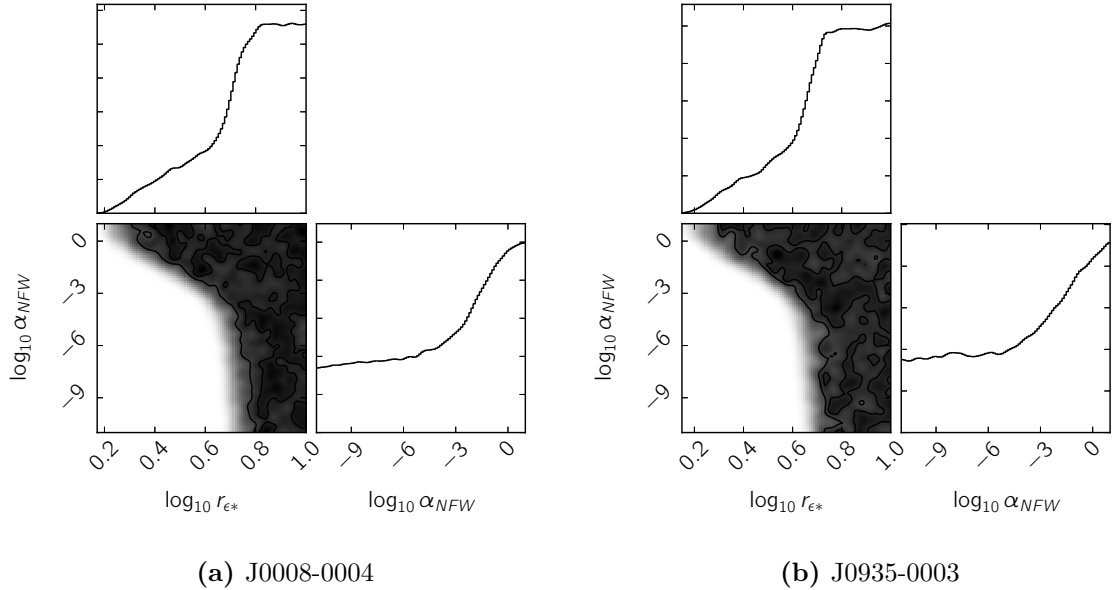


Figure 5.8: Posteriors for a configuration of $m_{a22} = 1$ and $\log(M_s/M_\odot) = 11.5$. The larger radii show a flat prior, which turns out to be a reasonable explanation considering that at these values the contribution of the tail is negligible.

soliton having a minimal contribution from the NFW tail. Particularly, looking for values where $\alpha_{\text{NFW}} < 1$ reduces the value of $\rho_{\text{NFW}*}$ to be taken into account. This translates into the need of a bigger radius $r_{\epsilon*}$ to allow any tail to be accounted for. Furthermore, after this region is crossed, the contribution of the tail is minimal that it does not matter how much of it is taken, the majority of the lens mass is given by the soliton alone. In other words, for an allowed soliton mass of $\log(M_s/M_\odot) = 11.5$, the soliton part is preferred and allowed to represent the complete contribution of the lens, and the NFW tail does not give any important addition which is why there is no clear constraint of the values. This corresponds to the soliton-only case which was analysed in the previous section.

The posterior plots for the rest of the galaxies are shown in figure A.1. They present the same behaviour of the soliton dominating the contribution of the lens mass. The conclusion obtained for $m_{a22} = 10$ can be extended for the other two selected axion masses. For comparison, figures 5.8 and 5.9 show the same selection of soliton masses,

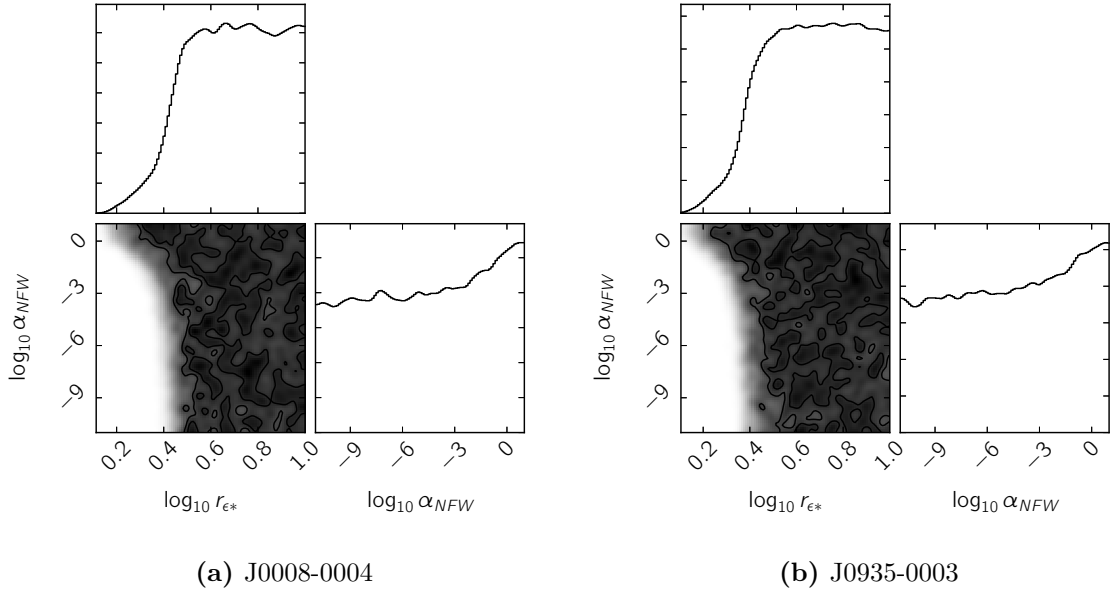


Figure 5.9: Posteriors for a configuration of $m_{a22} = 0.1$ and $\log(M_s/M_\odot) = 11.5$. The output is almost flat, and it only describes a minimum accepted value of radii.

with the only difference being that the results are shown for axion masses $m_{a22} = 1, 0.1$. The previous conclusion does hold as seen in the figures. The same definite limit is present, but for these masses there is a clear difference which consolidates the result. Previously it was stated that at higher radii the NFW tail does not have an important value, and for $m_{a22} = 1, 0.1$, this is even more true. It can be seen in figure 5.8 that after above a definite value of r_{ϵ^*} the posterior becomes flat and uniform, which means that there is no preference for any of the values. This is even more obvious by considering figure 5.9 where the posterior is almost uniform.

The conclusion is seen consistently for several axion masses: when the soliton is allowed to contribute the majority of mass for the lens, this will be represented by the soliton-only configuration having a negligible and almost null contribution from the NFW tail. A word of caution regarding the comparison, however. While the qualitative behaviour is the same, the physical values are not. The values are normalized by r_s which in turn depends of the value of the Soliton and Axion masses. For example, for J0008-0004 for $\log(M_s/M_\odot) = 11.5$ the corresponding radii for $m_{a22} = 1$ and $m_{a22} = 10$

are $r_s = 2.435$ pc and $r_s = 0.02435$ pc respectively. Using the previously mentioned characteristic radii and choosing the same value of normalized transition radius, for example $r_{\epsilon^*} = 0.8$, the physical values are 15.364 pc and 0.15364 pc for the axions masses, m_{a22} , 1 and 10 respectively. Similar to the soliton-only case, this means the actual size of soliton core is different, so it maintains the same properties and problems as the soliton-case, which means this configuration also not favoured. In turn, the soliton should be restricted to a lower contribution to the total lens mass.

The next part is to compare the cases where the restriction of the soliton mass is bigger, so the situation of the density exposed for the soliton case could be alleviated. As before the same two galaxies are selected as examples, and the rest of the galaxy posteriors can be found in appendix A. Now the case of importance, it is when there is an actual constraint of parameters that could say something related to the profile. Therefore, the next set of posteriors do not include the mass $\log(M_s/M_\odot) = 11.5$. Similar to the previous case, the two main galaxies are J0008-0004 and J0935-0003, which have their posteriors shown in figures 5.10 and 5.11. The first point, it is possible to notice the constraint of several values. Second, there is a clear tendency for the constrained region to shift to closer radii as the soliton mass is reduced. Of course, this has a mixed effect. As mentioned before, reducing the soliton mass, shifts the constraint region which is pushed even further by also by reducing the axion mass. It is straight forward to realize by means of eq. (5.7), that this effect is due to the relation between the soliton and axion masses. Nevertheless, while it is possible to constrain the parameters, there is long flat allowed region for α_{NFW} , and a double peak that can be clearly observed in both a) and b) sub-figures for 5.10 and 5.11. A clear reason for the second peak is not easy to find, but by the general behaviour the most feasible explanation comes from the previous problem, the soliton gives enough contribution to completely fill the required lens mass, which needs to not be confused with the total spherical mass, and this means that the soliton is almost dominating the total contribution, but in this case, due to the restrictions applied, it needs a minimum from the NFW tail.

By looking at figure 5.2, it is possible to complete the picture. The first "bump" it

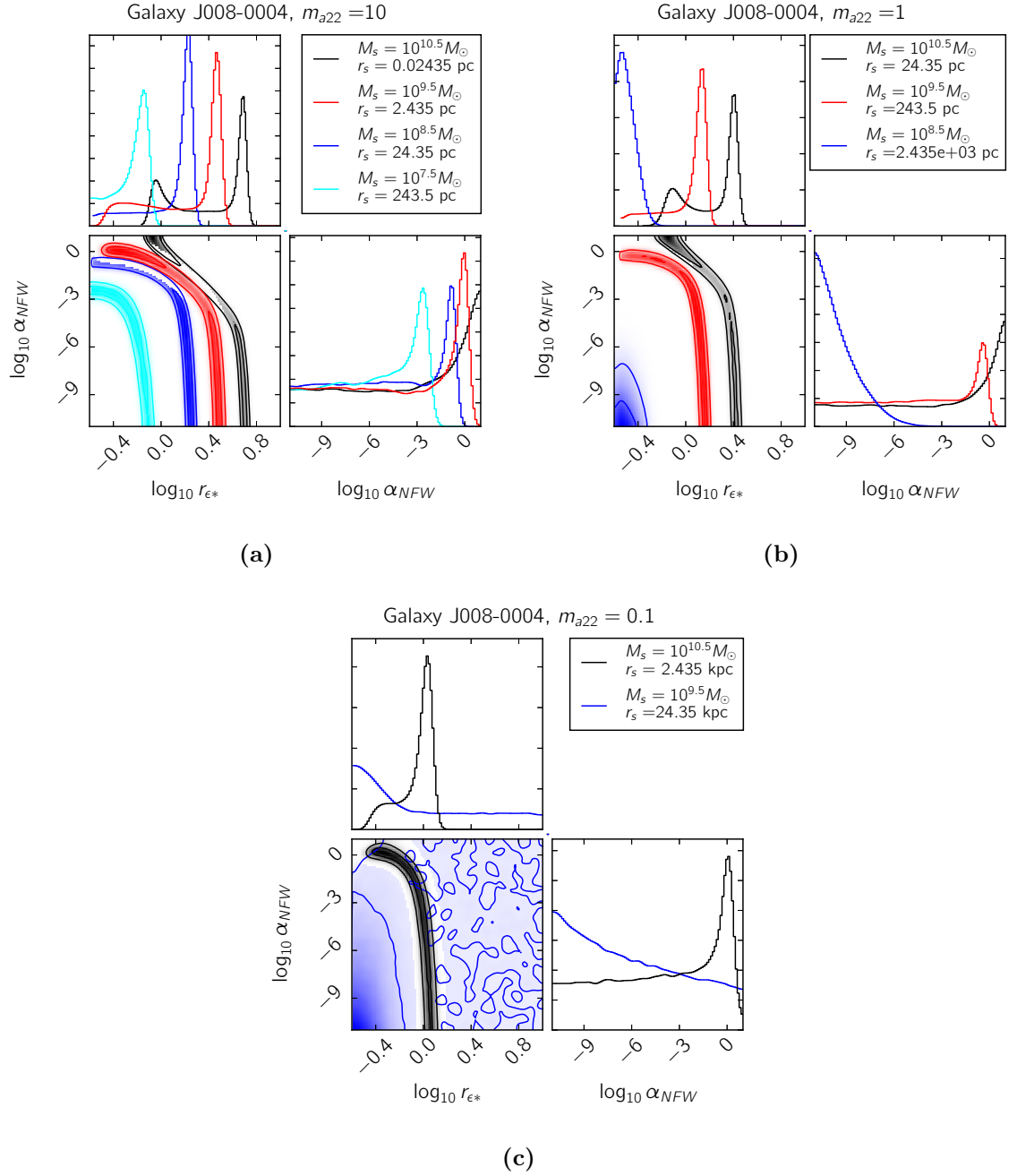


Figure 5.10: Posterior for galaxy J008-0004. Description is found in text.

is the minimum contribution to complete the lens mass, but this corresponds to the marginalized posterior of α_{NFW} for a corresponding peak. This is due to the value of lambda being high enough so the density of the tail contributes substantially, but as the radius increases the contribution drops, until it reaches the maximum possible

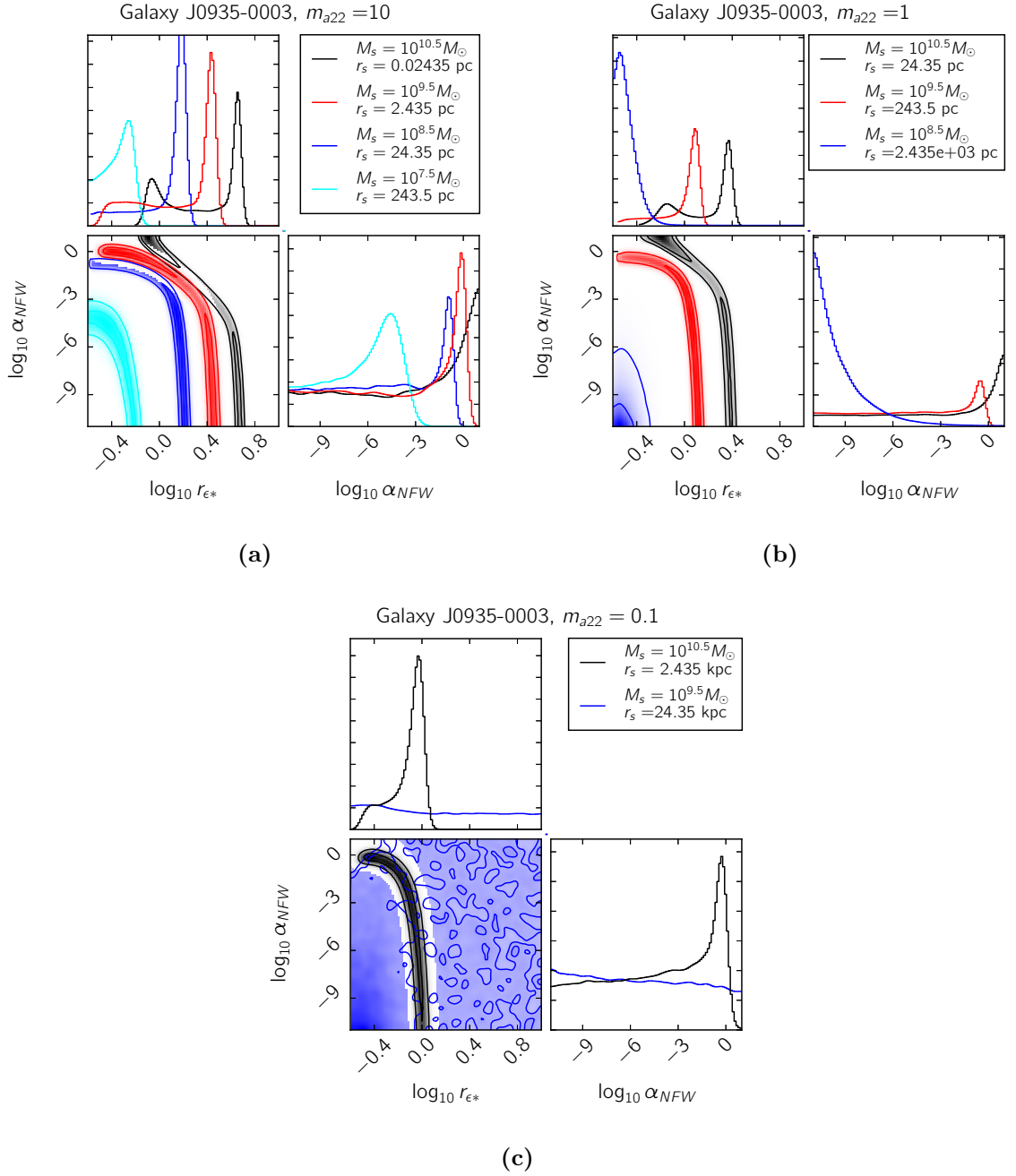


Figure 5.11: Posterior for galaxy J0935-0003. Description is found in text.

mass for the soliton and tail enough to complete the minimum required lens mass.

The second issue, is the flat region. This region, by observing the definition of α_{NFW} , it is possible to appreciate how the characteristic radius of the NFW tail extends. As an example, $\log(M_s/M_\odot) = 10.5$ has a transition radius of $r_s = 0.02435$ pc which by

choosing a value of $r_{\epsilon^*} \approx 0.7$ translates to a range of $24 \text{ pc} \lesssim r_{\text{NFW}} < \infty$. In other words, it is possible to constraint the value of the transition radius, but this only sets a minimum value for the NFW characteristic radius. The result can be observed in any other configuration, and it is strongly enforced on lower masses where there is a fixed minimum value of α_{NFW} . This effectively sets a true constraint or limits that can be taken. For Galaxy J0935-0003 with a selected $m_{a22} = 1$, in red, there is the constraint which has means that only values $\alpha_{\text{NFW}} < 1$ are able to contribute to the lens mass. In this case, the soliton at lower transition radii is not able to give enough contribution, but it is satisfied as the radius increases.

It should be noted that as the possible soliton mass is reduced, the response is to transition as soon as possible, and the NFW tail extends as long as much as it can, almost to infinity. This can be seen on the values for both galaxies for the selected masses of $\log(M_s/M_\odot) = 8.5$ and $m_{a22} = 1$. In both plots is represented in the b) by the blue line. The concentrated area constrains the value to be close to the border of the allowed $r_{\epsilon^*, \text{max}}$ and the value of $\alpha_{\text{NFW}} \rightarrow 0$. The lower masses are then not allowed, and as it can be seen for the cases of $m_{a22} = 0.1$, the lower masses are not really constrained. Posteriors in for the other galaxies can be found in appendix A. They possess the same features mentioned before, so the different results are shared among the sample of galaxies.

5.2.4 Summary of results

It is possible to described through a brief summary of the main characteristics found are:

- Allowing the soliton mass to be almost unrestricted, gives the majority of the contribution to the lens mass, and it produces results similar to having only a soliton profile, which means that the transition and characteristic radii are of a similar order as the previous case.
- Restricting the mass contribution of the soliton allows to have an actual restriction on the transition radius; nevertheless, for the case of the value of α_{NFW} only

a lower limit can be established. This restriction becomes even more obvious when mass contribution is reduced even further.

- In turn, as the soliton mass is reduced, the established inverse relation with the characteristic radius indicates an increase in the latter, which in turns helps to alleviate the problem of having a very dense soliton core.

From the three main results previously stated, the last one is the solution that was expected by adding the NFW tail. This shows that it is possible to represent a gravitational lens described by a wave dark matter profile and have a reasonable size for the soliton core without compromising it by having a high density core. As shown, the preference is to have lower axion masses for which the parameters of the model have a better defined constrained regions. Even so, it is not possible to precisely fix a value for the free parameters just by the lensing radius alone due to only the main contribution being the Einstein radius, R_E . More data is necessary if it is desired to have an extra constraint on the soliton or axion mass. On the positive side, it can be seen that the preferences keep the lower bound of the axion mass as $m_a > 10^{-24}$ eV which agrees with other works [134, 72, 130, 131, 62, 63, 33]. But the objective of showing that it is possible to use a soliton core + NFW tail to represent a a gravitational lens is met. However, further studies including other information about the nature of the galaxies will be required to obtain solid constraints of the different parameters. The subsequent chapters will change the approach from the traditional case of lensing of light to focus in the case of lensing of gravitational waves, to consider whether future observations of the latter phenomenon might provide useful additional insight into the nature of WaveDM.

Chapter 6

Wave optics for gravitational lensing

The lensing of light is a powerful tool in cosmology, and it is common to be treated from the point of view of the geometrical optics limit, but there is another treatment by using the wave approximation; this allows to not only consider the lensing for light but other wave phenomena [102]. Even more importantly in an astrophysical context, this creates the possibility to not only work with the lensing effect affecting light sources in the visible part of the spectrum, but also, other wavelengths with lower frequencies; furthermore, it allows to apply the phenomena not only to electromagnetic sources, but it can treat other type of emissions which can be affected by gravity: gravitational waves. In the past, A couple of examples for the wave approximation have been worked out for scalar, electromagnetic and gravitational waves by a point mass [91]. From this motivation, interesting results were obtained for the case of gravitational waves [126, 123, 119, 81] for several basic types of lens that could be expected to occur in real astrophysical systems; this work could be used in the future as a possible probe to discriminate between different halo models - e.g. between SFDM and standard CDM halos - and their potential effect on gravitational wave signals.

Throughout this chapter it will be assumed $G = c = 1$.

6.1 Diffraction integral

6.1.1 The lensing system

Gravitational lensing can be described, as with classical lenses, in a wave approximation. In principle, the treatment can be done considering a general wave, and it should not necessarily consider only the visible window of the electromagnetic spectrum, nor to be required that we are able to "see" an actual image [86, 91], which is done by solving the wave equation [81, 82] where the lens will act in a similar manner to the double slit and create a diffraction effect.

To help to determine where these effects become important, it is easy to consider the Schwarzschild radius of the lens as $r_E \sim M_L$, which defines the Einstein radius as $\xi \sim (r_E D)^{1/2} \sim (M_L D)^{1/2}$, and the source signal has a wavelength λ .

In fig. 6.1, it is possible to observe a basic description of the system, by representing the wavelengths as being of a size similar to the lens Einstein radius, and the distances analogous to the standard geometric approximation. The central peak of the interference pattern will be located at $x_p \sim (D_L/\xi)\lambda$ [126].

The maximum magnification of the incoming wave due to the diffraction will be of order $\sim \xi/x_p \sim M_L/\lambda$ [14, 80, 126]. From this it can be deduced that for a set Einstein radius, smaller wavelengths have a bigger amplification. This relation acts as a discriminator for wave or geometric optics approximation. In fig. 6.1, the dashed region represents the volume where the wave equation is solved. In this region the wave is diffracted and there is an amplification of the original (unlensed) signal produced by the source. A complete description for the different approaches to solve the wave equation in this case can be found in [102, 80, 91, 14, 135, 81, 80, 119]. Because an amplification on the phase is not considered, it is only present in the amplitude, even though the diffraction creates an oscillatory pattern on the phase; the comparison with an unlensed wave defines an amplification factor [126, 81, 123]. The following subsections will describe briefly the amplification factor for the wave and geometric approximations.

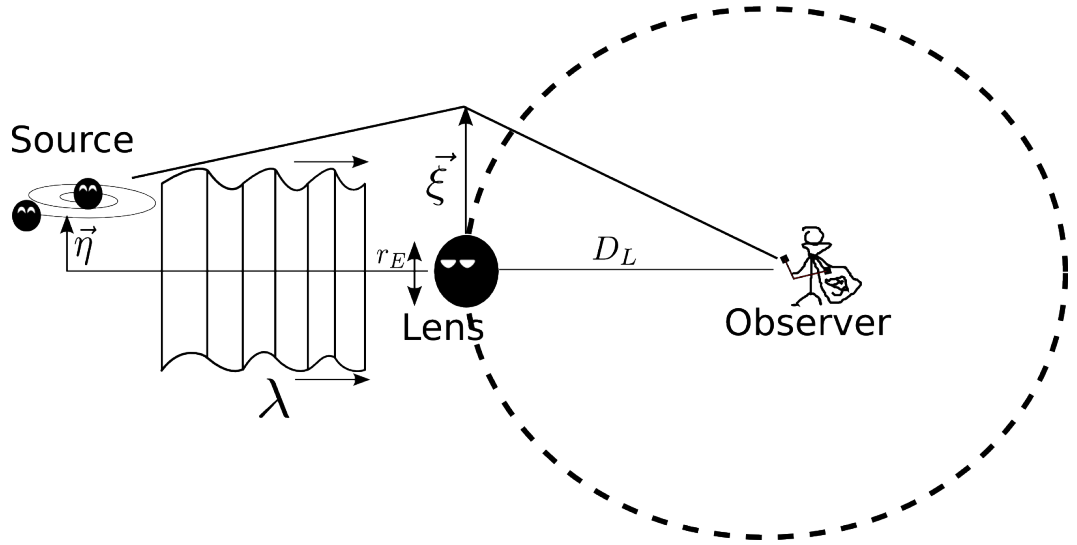


Figure 6.1: The lensing system considering a wave emitted by a source which passes close to a gravitational lens. A wavelength comparable with the Schwarzschild radius of the lens will produce a diffraction effect.

6.1.2 The amplification factor

In chapter 2, it was introduced the concept of magnification, which was produced by the difference in brightness between the lensed image and the unlensed source. In the case of waves, this concept is expanded, and the wave amplitudes are used instead. This defines a more general amplification factor as,

$$F(w, \boldsymbol{\eta}) = \frac{\phi_{obs}^L(w, \boldsymbol{\eta})}{\phi_{obs}(w, \boldsymbol{\eta})}, \quad (6.1)$$

where $\phi_{obs}^L(w, \boldsymbol{\eta})$ and $\phi_{obs}(w, \boldsymbol{\eta})$ are the lensed and unlensed wave amplitudes at the observer position, respectively. The unlensed case is characterized by the lack of the gravitational field of the lens. The amplification factor F is normalized such that $|F| = 1$ in the no lens limit.

The simplest lensing models are the axially-symmetric lens, and the amplification factor for them is given by [126, 81]

$$F(w, y) = -iwe^{iwy^2/2} \int_0^\infty dx x J_0(wxy) \times \exp \left[iw \left(\frac{1}{2}x^2 - \psi(x) + \phi_m(y) \right) \right], \quad (6.2)$$

were we define the dimensionless frequency w as,

$$w = \frac{D_S}{D_{LS}D_L} \xi_0^2 (1 + z_L) \omega. \quad (6.3)$$

The lensing produces a time delay of the signal which is defined as [102]

$$t_d(\boldsymbol{\xi}, \boldsymbol{\eta}) = \frac{D_L D_S}{2D_{LS}} \left(\frac{\boldsymbol{\xi}}{D_L} - \frac{\boldsymbol{\eta}}{D_S} \right)^2 - \hat{\psi}(\boldsymbol{\xi}) + \hat{\phi}_m(\boldsymbol{\eta}). \quad (6.4)$$

The variables relating the impact parameter $\xi \equiv |\boldsymbol{\xi}|$ and the source position $\eta \equiv |\boldsymbol{\eta}|$ are [102]

$$x = |\mathbf{x}| = \frac{\xi}{\xi_0}; \quad y = |\mathbf{y}| = \frac{D_L}{\xi_0 D_S} \eta, \quad (6.5)$$

with usually corresponds to the dimensionless time delay given by,

$$\begin{aligned} T(\mathbf{x}, \mathbf{y}) &= \frac{D_L D_{LS}}{D_S} \xi_0^{-2} t_d(\xi, \eta) \\ &= \frac{1}{2} |\mathbf{x} - \mathbf{y}|^2 - \psi(\mathbf{x}) + \phi_m(\mathbf{y}). \end{aligned} \quad (6.6)$$

Here D_S, D_{LS} and D_L are the distance from the observer to the source, between the lens and the source and from the observer to the lens respectively, and ξ_0 is a normalization constant of the length. $\psi(x) = \psi(|\mathbf{x}|)$ is the potential produced by the source, and $\phi_m(y) = \phi_m(|\mathbf{y}|)$ is a phase constant which is used to obtain a minimum time delay of zero in eq. (6.6), which usually corresponds to time delay of the "image" which travels the shortest geometric path to the observer [80]. It should be mentioned that when the lensing parameters allow multiple images of the source, it results in an interference pattern between the images in addition to the diffraction produced by the lens [78]. For the case of $w \gg 1$, the geometrical approximation would be sufficient [86, 80, 126, 122].

6.1.3 Geometrical optics approximation

From eq. (6.2), it is possible to recover the geometrical optics amplification factor by considering the case $w \gg 1$ [86, 80, 126, 122]. For this case, the integrand of eq. (6.2) is a rapidly oscillating function and only the stationary points, \mathbf{x}_j give a contribution to the integral which implies $\nabla_{\mathbf{x}} T(\mathbf{x}, \mathbf{y}) = 0$. This is simply the Fermat's principle of least time. Starting from the lens equation

$$\mathbf{y} = \mathbf{x} - \nabla_{\mathbf{x}} \psi(\mathbf{x}). \quad (6.7)$$

The positions \mathbf{x}_j are directly obtained from the lens equation. We expand the time delay around the j^{th} image as

$$T(\mathbf{x}, \mathbf{y}) = T(\mathbf{x}_j, \mathbf{y}) + \sum_a \partial T(\mathbf{x}_j, \mathbf{y}) \tilde{x}_a + \frac{1}{2} \sum_{a,b} \partial_a \partial_b T(\mathbf{x}_j, \mathbf{y}) \tilde{x}_a \tilde{x}_b + \mathcal{O}(\tilde{x}^3). \quad (6.8)$$

where $\tilde{\mathbf{x}} = \mathbf{x} - \mathbf{x}_j$, and the indices for a, b, \dots run from 1 to 2. The first order term vanishes because \mathbf{x}_j is an stationary point. Taking into account the approximation and all the contributions of the stationary points in eq. (6.2) leads to

$$F(w, \mathbf{y}) = \sum_j \frac{w}{2\pi i} \int d^2 \tilde{\mathbf{x}} \exp[iwT(\mathbf{x}_j, \mathbf{y}) + \frac{1}{2} \sum_{a,b} \partial_a \partial_b T(\mathbf{x}_j, \mathbf{y}) \tilde{x}_a \tilde{x}_b]. \quad (6.9)$$

Considering now the system in Cartesian coordinates with only diagonal components, which means having \tilde{x}_1 and \tilde{x}_2 vectors having no cross derivatives, it is possible to express the integral as

$$F(w, \mathbf{y}) = \sum_j \frac{w e^{iwT(\mathbf{x}_j, \mathbf{y})}}{2\pi i} \int d^2 \tilde{\mathbf{x}} \exp[\frac{iw}{2} (\partial_1^2 T(\mathbf{x}_j, \mathbf{y}) \tilde{x}_1^2 + \partial_2^2 T(\mathbf{x}_j, \mathbf{y}) \tilde{x}_2^2)]. \quad (6.10)$$

The remaining terms can be solved using the Gaussian integral ¹. This leads to the amplification factor in the geometrical optics approximation [81],

$$F_{geo}(w, \mathbf{y}) = \sum_j |\mu_j^{1/2}| \exp[iwT_j - i\pi n_j], \quad (6.11)$$

where the magnification of j^{th} image is $\mu_j = 1/\det(\partial \mathbf{y} / \partial \mathbf{x}_j)$, $T_j = T(\mathbf{x}_j, \mathbf{y})$ and $n_j = 0, 1/2, 1$ when \mathbf{x}_j is a minimum, saddle or maximum point of $T(\mathbf{x}, \mathbf{y})$ respectively. Here the value of $|\mu_j|$ coincides with the definition of the magnification factor in section 2.

6.2 Lens models

6.2.1 The point mass lens

The easiest solution of (6.2) to work with is the point mass lens. From all the other possible lenses, this is the only one with an analytical solution [91]. For the normalization constant in this case it is usually agreed to use $\xi_0 = (4M_L D_L D_{LS} / D_S)^{1/2}$

¹ $\int_{-\infty}^{\infty} dx e^{iax^2} = \sqrt{\frac{\pi}{|a|}} e^{i\pi/4 \times \text{sign}(a)}$

which correspond to the Einstein radius of the point mass lens in the geometric optics limit [102, 78]. The amplification factor is then defined as

$$F(w, y) = \exp \left[\frac{\pi w}{4} + i \frac{w}{2} \left\{ \ln \left(\frac{w}{2} \right) - 2\phi_m(y) \right\} \right] \Gamma \left(1 - \frac{i}{2} w \right) {}_1F_1 \left(\frac{i}{2} w; 1; \frac{i}{2} w y^2 \right), \quad (6.12)$$

where $w = 4M_{Lz}\omega$; $\phi_m(y) = (x_m - y)^2/2 - \ln x_m$ with $x_m = (y + \sqrt{y^2 + 4})/2$; M_{Lz} is the red-shifted lens mass and ${}_1F_1$ is the confluent hyper-geometric function [126]. Figure 6.2 shows an example of the amplification factor; here the interference pattern between multiple images mentioned earlier is clearer above $w > 10$. In the same way, this equation has a solution for the geometrical optics limit with $w \gg 1$ which is given by

$$F_{geo} = |\mu_+|^{1/2} - i|\mu_-|^{1/2} e^{\omega\Delta T}. \quad (6.13)$$

The magnification for each image is $\mu_{\pm} = 1/2 \pm (y^2 + 2)/(2y\sqrt{y^2 + 4})$, and the time delay is given, as presented in [126, 81, 120], by

$$\Delta T = y \frac{\sqrt{y^2 + 4}}{2} + \ln \left(\frac{\sqrt{y^2 + 4} + y}{\sqrt{y^2 + 4} - y} \right). \quad (6.14)$$

The next subsections present examples for other types of lens, but these are solved numerically.

6.2.2 Singular Isothermal Sphere(SIS) - lens

Several properties of the SIS have already been presented in chapter 2. In the case of wave treatment the SIS can no longer be solved analytically, and needs to be done numerically. The normalizing Einstein radius is $\xi_0 = 4\pi v^2 D_L D_{LS} / D_S$. The amplification factor eq. (6.2) is integrated numerically where the potential is $\psi(\mathbf{x}) = |x|$. As in the previous lens, the potential constant is obtained by the shortest time delay which is taken as the positive solution of x of the lens equation. This corresponds to $\varphi(y) = y + 1/2$, and it is possible to define a mass similar to the case of the Point Mass lens as $M_{Lz} = 4\pi^2 v^4 (1 + z_L) D_L D_{LS} / D_S$. This defines the frequency $w = 4M_{Lz}\omega$.

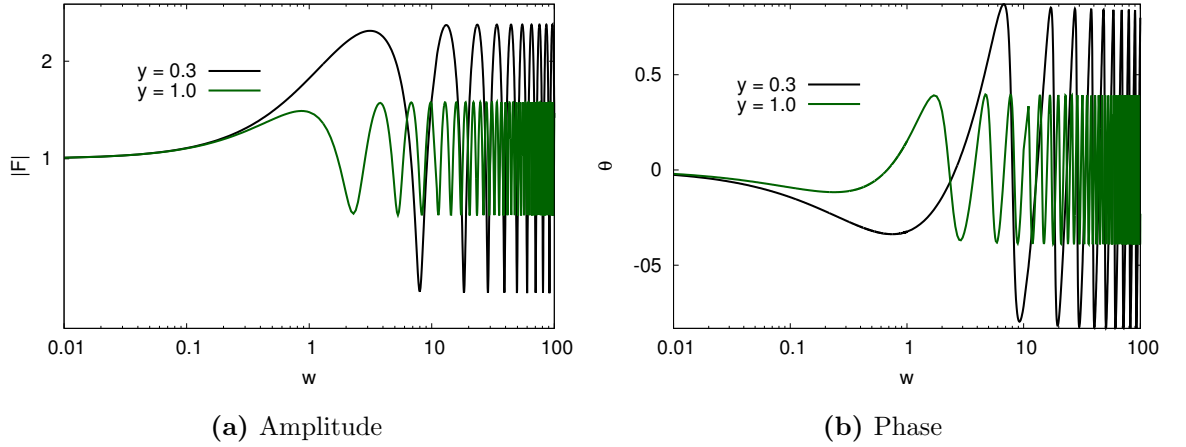


Figure 6.2: Amplification factor for the point mass lens. a) The amplitude of the lens for $y = 0.3$ and $y = 1.0$. The values with high oscillation correspond to $w > 1$; as the frequency w increases it approaches to the geometrical limit. b) The phase of the point mass lens amplification factor. The selection of the phase constant allows the phase to be contained within a range of values of θ , and it can be seen how the increase in w produces the oscillatory effect on the phase, similar to the amplitude.

The amplification factor F only depends on two parameters, w and y . The geometrical optics limit is given by [126],

$$\begin{aligned}
 F_{geo} &= |\mu_+|^{1/2} - i|\mu_-|^{1/2} e^{iw\Delta T} \quad \text{for } y < 1, \\
 &= |\mu_+|^{1/2} \quad \quad \quad \quad \quad \text{for } y \geq 1,
 \end{aligned} \tag{6.15}$$

where $\mu_{\pm} = \pm 1 + 1/y$ and $\Delta T = 2y$. The value of y separates the condition for the number of images. For $y < 1$ double images are formed, while for $y \geq 1$ only a single image is formed.

6.2.3 NFW lens

The Navarro, Frenk and White (NFW) profile as mentioned earlier in chapter 2 is the most general profile used for the description of the mass distribution in galaxies. As well as for the point mass lens and the SIS lens, the NFW profile can be used to

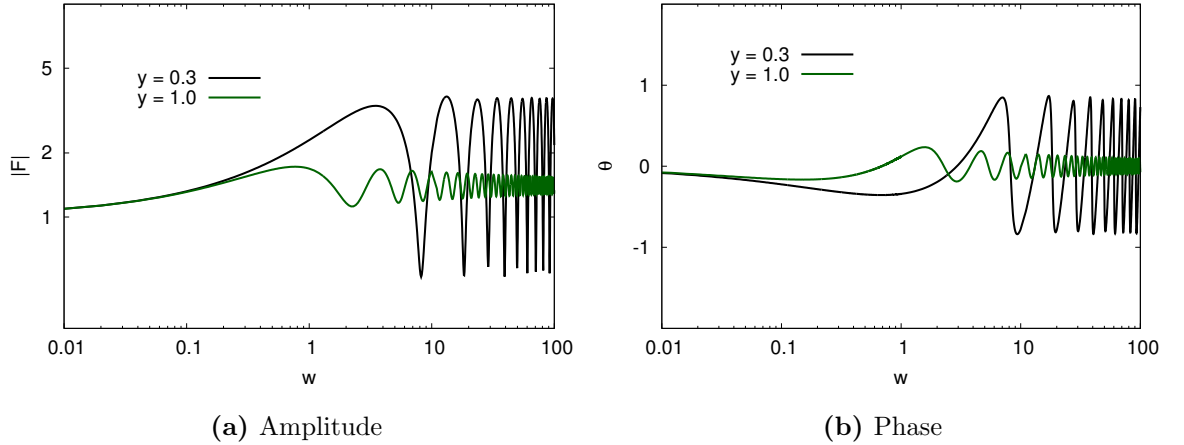


Figure 6.3: Amplification factor for Singular Isothermal Sphere (SIS). a) The amplitude of the SIS, as well as the point mass presents the same oscillatory pattern when $w > 1$, but for the same value of y the amplification of the amplitude is bigger for the SIS. As y increases, the oscillation in the amplitude is decreases but this in principle settles, which corresponds to the value in the geometric optics. b) The phase oscillates for higher values, but it is still bounded inside a region; the phase at the same time presents the same decreasing behaviour for increasing y .

describe a lens, as has been shown in previous chapters. The amplification factor F cannot be solved analytically, and it needs to be obtained numerically. Unfortunately, another difference exists with the previous two cases, since for the NFW profile the phase constant also needs to be obtained numerically because the lens equation cannot be solved analytically. In a similar manner to the other cases, the lens is described through its lensing potential which is given by [7, 54]

$$\begin{aligned} \psi(x) &= \frac{k_s}{2} \left[\left(\ln \frac{x}{2} \right)^2 - 4 \left(\operatorname{arctanh} \sqrt{\frac{1-x}{1+x}} \right)^2 \right] \quad \text{for } x \leq 1, \\ &= \frac{k_s}{2} \left[\left(\ln \frac{x}{2} \right)^2 + 4 \left(\operatorname{arctan} \sqrt{\frac{x-1}{1+x}} \right)^2 \right] \quad \text{for } x \geq 1. \end{aligned} \quad (6.16)$$

There is now a third parameter $k_s = 16\pi\rho_s(D_L D_{LS}/D_S)r_s$. In this case the normalization parameter is $\xi_0 = r_s$. This differs to the previous cases by not choosing the

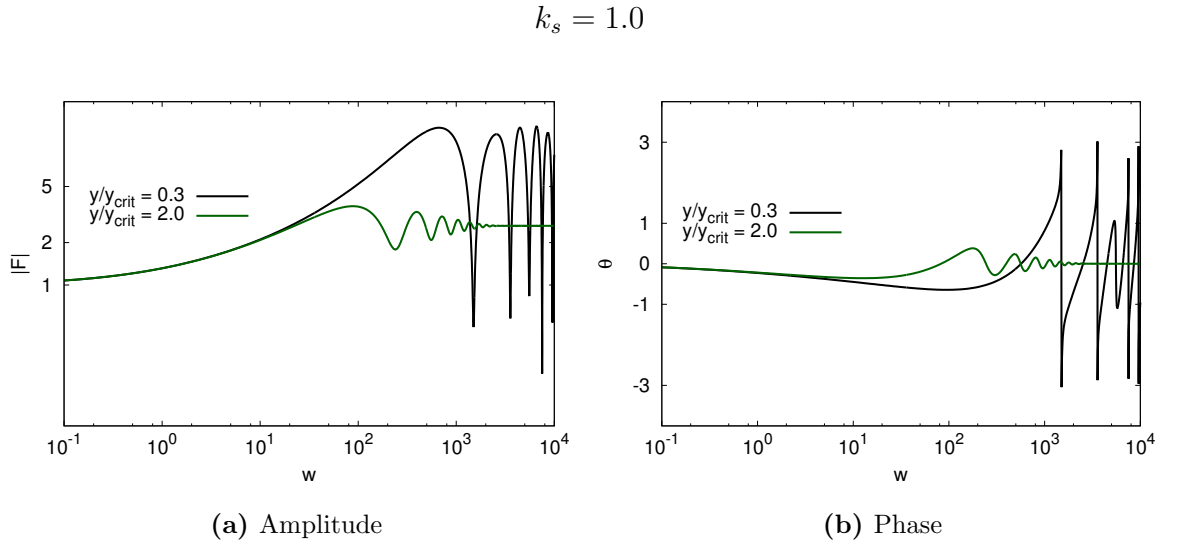


Figure 6.4: The NFW profile requires a different approach and has the extra parameter k_s . Both of the images correspond to the case $k_s = 1$. a) The amplitude of the amplification factor is plotted for two examples of y which is normalized by y_{crit} which corresponds to the radial caustic. b) The phase in this case decays faster than in the previous profiles, and for the case where there is not decay, there is an abrupt change.

Einstein radius, but the characteristic radius to provide the normalisation. The amplification factor and the phase constant for the zero time delay cannot be obtained analytically and needs to be solved numerically; the same situation arises for the geometrical limit for the derivation of the image positions x_j , magnifications μ_j and time delays T_j which are obtained from the numerical solution of the lens equation, meaning that F_{geo} is obtained numerically. The radial and tangential caustics are solutions of the lens equation where the magnification in the geometric approximation reaches a maximum, in the standard treatment of light they are theoretically infinite [102]. Furthermore, the tangential caustic corresponds to $y = 0$, and the radial defines a critical value $y \equiv y_{crit}$; $|y| < y_{crit}$ is a region where three images are formed, and when $|y| > y_{crit}$ only one image is formed. In this manner, y_{crit} helps to normalize the values of y for the NFW profile as seen in fig. 6.4. The amplification factor now depends on three parameters: w , y and k_s .

6.2.4 ψ DM - soliton lens

The WaveDM profile was introduced in chapter 4; There were two cases solved for the reduced mass: the soliton core alone and the soliton+NFW tail. For the amplification factor F , the lens is described by the lensing potential $\psi(x)$; unfortunately, the complete case is too complex to be solved analytically, and the numerical solution is not as straight forward to implement as the other cases we have considered and would require a more extended analysis. Nevertheless, in order to gain some useful insight, the soliton core lensing potential can be obtained and used to calculate the amplification factor. As shown in chapter 5, the soliton core is expected to make a major contribution to the mass and, depending on the core size, it can have a high density. So the use of the soliton-only case as a first approximation is justified in what follows, since we expect that the potential will be enhanced compared with the NFW case and that the main interaction will be with the inner core compared with the NFW tail - taking into account the fact that the tail extends over a larger region in its contribution to the mass of the halo. For this reason, and since it provides a simpler solution, the soliton-only case will be presented here and in the next chapter when the lensing of a gravitational wave is considered and the results the results of gravitational wave lensing are compared for different lens models with similar parameters.

The simpler way to obtain the lensing potential is by the integral [102]

$$\psi(x) = 2 \int_0^x x' dx' \kappa(x') \ln\left(\frac{x}{x'}\right). \quad (6.17)$$

The function $\kappa(x) \equiv \Sigma(x)/\Sigma_{crit}$, and from equation (4.20),

$$\Sigma(x) = \rho_s r_s \frac{429\pi}{2048} (1+x^2)^{-15/2}, \quad (6.18)$$

where $x = \xi/r_s$. By applying eq. (6.18) to eq. (6.17), performing the integral, for the evaluation at zero an expansion is considered; therefore the potential is

$$\psi(x) = 2 * k_s * \frac{429\pi}{2048} \left[\frac{1}{13} \left(\ln(\sqrt{x^2+1} + 1) - \sum_{n=0}^5 \frac{1}{(2n+1) * (1+x^2)^{n+1/2}} \right) + \frac{6508 - 3465 \ln(2)}{45045} \right], \quad (6.19)$$

where is $k_s = \rho_s r_s / \Sigma_{crit}$. The potential is used in the expression for the amplification factor, which is evaluated numerically similar to the treatment for the NFW profile. The image positions x_j and time delays T_j are solved numerically too, but the values of $u_j \equiv \mu(x_j)$ can be obtained from

$$\mu(x_j) = \left[\left(1 - \frac{m(x)}{x^2} \right) \left(1 + \frac{m(x)}{x^2} - 2\kappa(x) \right) \right]^{-1}. \quad (6.20)$$

The normalized surface density $\kappa(x)$ has the parameter k_s defined earlier, and the normalized projected mass is obtained from eq. (4.21) by an adjustment of the normalization,

$$m(x) = \frac{k_s}{\pi} \frac{2}{13\lambda_{crit}} \frac{(1+x^2)^{13/2} - 1}{(1+x^2)^{13/2}}. \quad (6.21)$$

In chapter 4 was shown that $\lambda_{crit} = 2048/(429\pi^2)$, and in the same chapter the parameter λ was introduced which encapsulated the information of the lens and the geometry of the system. It was mentioned that the condition $\lambda > \lambda_{crit}$ must be satisfied if the lensing system was expected to produce strong lensing. In this case due to the normalization it is more convenient to define the condition in terms of the extra parameter in the potential and assigning $\lambda = k_s/\pi$, this translates for the condition of strong lensing to be

$$k_s > \frac{2048}{429\pi} \approx 1.52. \quad (6.22)$$

The amplification factor similarly to the NFW profile also depends on three parameters w , y and k_s . In a similar manner, it is convenient to define a value y_{crit} to separate regions where there are several images; the next section will show how this approach is used in the solution, and compare the amplification factor with other type of lenses discussed.

6.3 Comparison of lens properties

The previous section introduced the basic lenses which had already been described in detail in [122, 81, 82, 126], and the introduction of the soliton-core as a lens in the wave approximation. The following section presents a brief comparison on the behaviour of the three lenses.

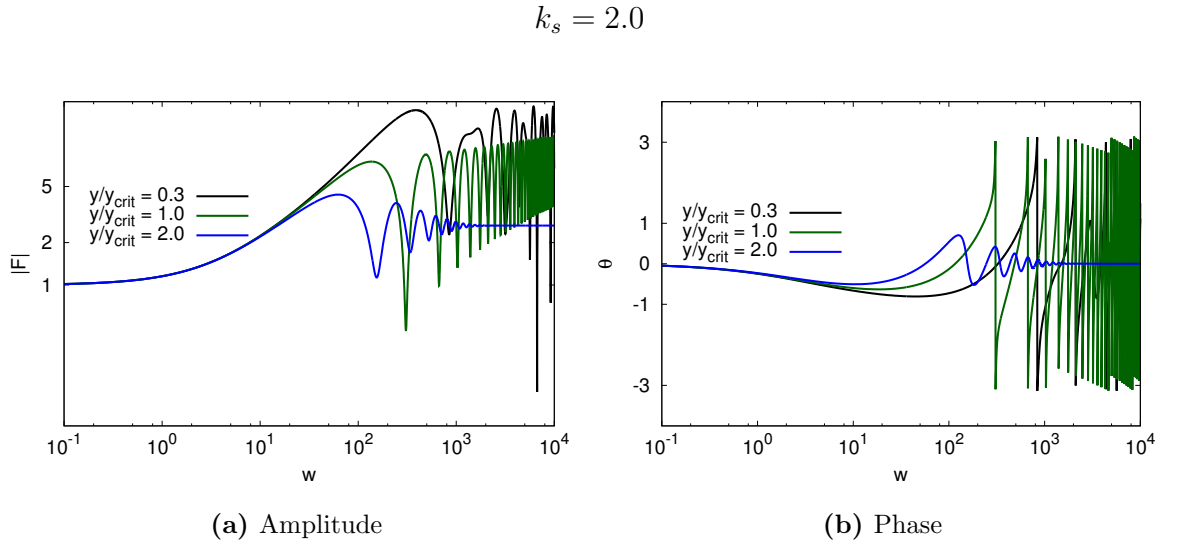


Figure 6.5: The soliton profile amplification factor for the fixed value of $ks = 2$. a) The amplitude of y is normalized by y_{crit} . It has three values, $y/y_{crit} = 0.3, y/y_{crit} = 1, y/y_{crit} = 2.0$. b) The phase has an oscillatory pattern due to the diffraction and image interference, but above y_{crit} the oscillations decrease and disappear at sufficiently high frequency as there is only one image produced.

The point mass lens is the simplest of all the lenses, and it is the best to show the pattern of the amplification factor. There are three regions for all the lenses; the first region is $w \ll 1$, here there is no possible amplification, which is expected considering a wavelength long enough that the effect of the lens can be neglected [86]. The second region is $w \gtrsim 1$ which corresponds to the regime where the size of the lens and the wave are comparable and the lensing effect can be studied in the wave approximation [80]. The last is when $w \gg 1$ which modifies this corresponding to being close the geometrical approximation, and in fact if the value w is big enough both should agree [126]. The three regimes can be clearly found in 6.2 and 6.3 which correspond to the point mass and SIS; nevertheless, for the NFW and soliton there is a third parameter which modifies this. The amplification factor is a complex value, so it is separated into its amplitude and phase to better understand its behaviour. For the point mass lens in figure 6.2, panel (a) is the amplitude and panel (b) shows the phase. The case of the point mass is a great example to show the expected behaviour

of the lens since it may be completely solved analytically, so it is the simplest of all the solutions and the diffraction effect is clearer on it. The oscillations are clear and well defined, and this case has been widely used to show the basic behaviours of lensing in waves [120, 124, 92, 8, 32, 85, 65, 112, 34].

Scaling up in complexity, the following step is to take into account extended lenses, and the simplest of them is the Singular Isothermal Sphere(SIS). This is an axially symmetric lens, and the effect of the amplification is stronger compared with the point mass; this can be seen in fig. 6.3. Because it depends in the same parameters as the point mass, and the three regions previously mentioned of w are clearly visible, but as the value of y increases the oscillations decrease for both, the amplitude and phase, which should converge in the geometrical optics limit. Similar features can be observed to the point mass for the oscillatory pattern. This is especially analogous for $y < 1$ where there is interference of multiple images. For $y \gtrsim 1$, this is not the case, and only the diffraction from the lens is present, therefore decreasing at higher frequencies in contrast with the point mass as seen in fig. 6.2.

6.3.1 NFW and Soliton

For the other two lenses, NFW and soliton, similarities are shared on the lower frequencies and close to unity, $w \lesssim 1$; but because there is a third parameter, k_s , and the normalizing constant length is different, they are slightly different. The parameter k_s for both lenses represents the same idea, it compares the critical density, with the product of the density of the model and its characteristic radius. Larger the parameter more extended or denser is the lens, and this relates to a simple way to discriminate the possibility of strong lensing. This is related with a topic mentioned in Chapter 4, it was introduced as λ , and for the NFW lens it is always possible to produce lensing, but the soliton needs a minimum value which has been said in the previous section to be $k_s > 1.52$. Another difference is the oscillations; they are not smooth and stable as with the simpler profiles with the lower values of y , for both the amplitude and phase. This feature is shared for both of the lenses in figures 6.4 and 6.5. It should be noticed

that instead of y as the parameter, it is replaced by y/y_{crit} , which as mentioned earlier, is used to separate the region in which multiple images are produced from the region in which a simple image is produced. In fig. 6.5, the value for y_{crit} is plotted along the others, and it can be seen that for $y/y_{crit} > 1$ there is no interference between of multiple images as w increases; with only one image the amplification converges to a stable value which corresponds to the geometrical optics limit.

6.3.2 Summary

This chapters present a short review of the amplification factor for waves and the simple lenses studied, and it introduces the soliton-core as a lens in the wave approximation. It compared the selected values for the main parameters y and w , as well as a brief description of the general behaviour of the different models including the introduction of the basic features of the soliton-core as a lens. The next chapter will analyse more carefully the soliton, and will use it as a possible example of a lens for a gravitational wave.

Chapter 7

Gravitational lensing of gravitational waves

Gravitational lensing is a very useful tool for the detection of electromagnetic signals as mentioned earlier, and in the previous chapter it was introduced the basic description for the application of this effect in the wave optics regime. In particular, chapter 6 presented a description of the amplification factor which would be useful to describe another wave phenomenon that could be affected by lensing, which is gravitational waves. The following chapter gives a review of the recent discussions on parameter estimation for Gravitational Waves (GW), and describes in more detail the ψ DM profile and applies it to a simulated gravitational wave, and compares it with the SIS profile. At the end, a brief discussion is presented regarding the future work that could be done by using the effects on GW to discriminate the nature of galactic objects and haloes.

7.1 Gravitational lensing effects

As previously mentioned in chapter 6, the effects of lensing can be considered in the wave or geometrical optics approximation. The difference concerns the relation of sizes between the wavelength of the signal and the gravitational size of the lens, its Schwarzschild radius, which will determine the most adequate approximation [86, 80].

Although the wave treatment is still valid at shorter wavelengths, it becomes computationally expensive to calculate due to the oscillatory behaviour of the amplification integral as seen in eq. (6.2). The following sections will present brief review of the works done regarding the effect of lensing on the detection of gravitational waves.

7.1.1 Effects on the lensed wave

The previous chapter introduced the formalism of lensing for the wave optics approximation. This was done considering the effect of a wave interacting with the gravitational field of the lens. Here onwards the incoming wave is assumed to be a gravitational wave. For now, how the radiated wave is produced is not going to be of concern, but only the effects of the lens on the wave. In general, the lens is considered to interact in the exterior region of its the field, so it does not form a true focal point [87]. If a focused wave passed through the centre region of the gravitational field of the massive object, assuming this is not a black hole, a true focus could be formed, but by passing close to the object only caustics are formed [86, 87]; the latter being the case of consideration.

The gravitational wave could be treated in the wave or geometric optics regime. The discriminating factor as mentioned before is the relation existing between the Schwarzschild's radius of the lens and the wavelength of the wave being $\sim M_L/\lambda$. For geometric optics, the amplification is appreciable for small displacements of the axis; meanwhile for wave optics it is the determined by the relation of M_L/λ [86, 87]. This relations not only affects the regime in which the lensing should be analysed, but it also constrains the detectors that would be able to detect a lensed signal.

Considering the Advanced Laser Interferometer Gravitational-Wave Observatory (Advanced LIGO) detector which possesses a sensitive frequency range between $10 - 10^3$ Hz, this translates to a range $\lambda \sim 3 \times 10^4 - 10^2$ km [71]. A quick calculation with the adequate units leads

$$mr = \frac{4\pi G M_L}{c^2 \lambda} = 2 \times 10^4 \left(\frac{1\text{m}}{\lambda} \right) \left(\frac{M_L}{M_\odot} \right). \quad (7.1)$$

Here mr will be defined as the lens mass relation with wavelength, and any value that is $mr \ll 1$ will have minimum to no lensing. For $mr \gg 1$ the geometric optics

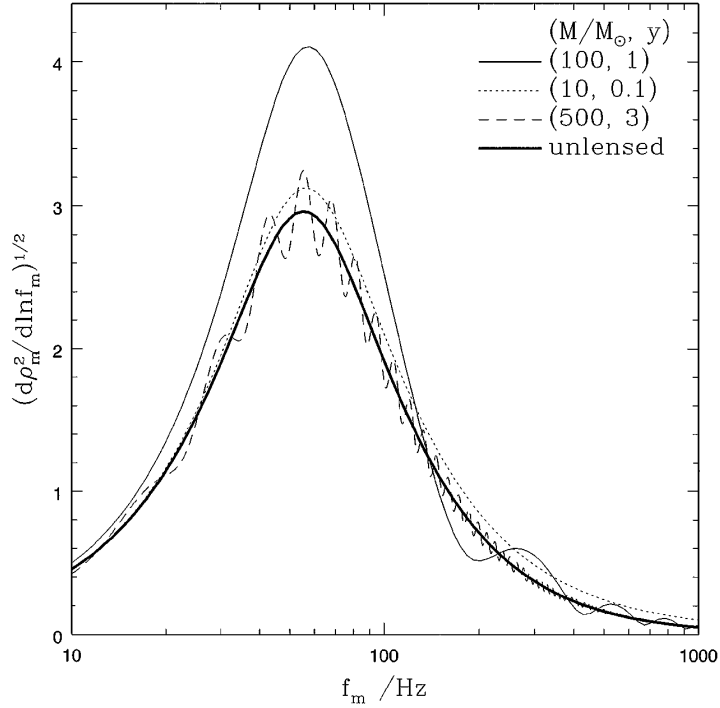


Figure 7.1: Frequency distribution of the signal-to-noise ratio against for several configurations of point mass lenses, and positions y . It presents several deviations from the unlensed case as well as the oscillatory pattern which could represent a signature of gravitational lensing. Figure taken from [80].

approximation is valid, and $mr \gtrsim 1$ will be the closest region where diffraction effects are present and the wave approximation is more adequate [133].

Selecting the minimum wavelength for LIGO's range, from eq. (7.1) the mass that satisfies an $mr \sim 1$ is $\sim 15M_\odot$ where the diffraction effects become significant. Even more, in [80] it is recommended that the wave flux cannot be magnified significantly by any mass lighter than $\sim 10^2M_\odot$. Analysis done in [135], considers geometrical optics, but this is not adequate due to the need to consider the diffraction effects are present, as mentioned in [6, 133, 80].

Going even further, it is possible to set a cut-off frequency to determine the validity of geometrical optics or to take the effects of diffraction into account.

The cut-off frequency is given by [133, 14],

$$\omega_c = \left(\frac{\pi}{10} \frac{GM_L}{c^3} \right)^{-1}. \quad (7.2)$$

G and c are Newton's gravitational constant and speed of light, respectively. M_L is the mass of the lens. As an example, M_L bigger than $10^6 M_\odot$ has a cut-off frequency lower than 1Hz. Which would indicate that sources which could be lensed by this object should be treated by the geometric optics approximation for the case of Earth-based detectors, but it is in the regime of a detector such as LISA (Laser Interferometer Space Antenna) which has a frequency range that extents up to 10^{-4} Hz [133, 49].

Rates of lensed events for Binary Black Holes for LIGO of $0.2_{-0.1}^{+1.0} \text{yr}^{-1}$ that rises to $14.2_{-10.7}^{+80.5} \text{yr}^{-1}$ at design sensitivity limit have been estimated in [85].

Going even further by consider the new generation detector called the Einstein Telescope (ET thereafter), its improved sensitivity would be excellent for the detection rate of lensed Double Compact Objects (DCO) like Black Hole-Black Hole (BH-BH), Black Hole-Neutron Star (BH-NS) and Neutron Star-Neutron Star (NS-NS) binaries [127, 8, 32]. In principle, it should be able to detect galaxy size lenses and not just by point mass lens [92].

Table 7.1 present an example of some of the expected numbers of lensed events calculated in [8] for DCO's for the initial and advanced "xylophone" configurations. These results consider the time of the survey T_{surve} and the sources to be around between a redshift $z_s = 5$ to $z_s = 1$. From this table, the conclusion to be taken is that it is likely that lensed events will be observed by the ET, and it is expected that strongly lensed events will be dominated by BH-BH binaries [8].

The study in the wave optics regime can lead to interesting differences. One of these is considering the particular case of a gravitational wave signal being emitted simultaneously with its electromagnetic counterpart and being lensed by the same type of lens. In this case a comparison in the time delay of the signals would be necessary. The electromagnetic counterpart would be treated by geometric optics, but for the gravitational wave, if the path difference between the multiple signals is smaller than the wavelength of the wave, given by the condition $w(T_i - T_j) \gtrsim 1$ where w and T are

the dimensionless frequency and time delay as defined in section 6.1.3, respectively; the geometric optics approach is not valid any more as stated in [125]. Analysis shows that in this particular situation the gravitational wave would arrive earlier than the Electromagnetic counterpart; even more, it presents some estimates for the different type of detectors about the maximum time difference considering a point mass lens, being typically $\sim 1\text{ms}(f/100\text{Hz})^{-1}$ for ground-based detectors, $\sim 2\text{min}(f/\text{mHz})^{-1}$ for space-based detectors, and $\sim 4\text{months}(f/10^{-8}\text{Hz})^{-1}$ for pulsar timing arrays [125].

Up to here the majority of the effects described have been related with the signal or how its modification changes the detection, including examples of rates. In the following subsection it will be briefly reviewed how the parameter estimation of the signals could be affected by the lensing effect.

7.1.2 Effects on parameter estimation

The previous section described briefly the effects of the lensing over a signal and how this is modified compared to the unlensed case; mentioning some of the rates or cases for the different detectors and separating the wave and geometric optics limits. In the previous section, what was the source was not of main importance, although several possible cases were mentioned. However, when detecting gravitational waves, although important in itself, the goal is to obtain information about the sources, including their mass or redshift, that would give information about astrophysical processes or even cosmological parameters [1, 71, 53, 18]. This section describes some other works about how the lensing of a signal could create challenges in the parameter estimation of the sources. Therefore, some sources could have a different consideration than others. The majority of work has been done considering a point mass lens; for the case of a gravitational wave signal which travels through a uniformly distributed point-like masses region, if it is lensed on the regime where $\lambda \gg M_L$, it will produce a magnification that is small but not negligible due to the total effect being the accumulation of the several magnifications. On the other hand, for $\lambda \ll M_L$, the geometric optics approximation is valid, and the total magnification comes from the focusing and interference

ET configuration	standard	optimistic
T_{surv}	(1yr; 5yrs;continuous)	(1yr; 5yrs;continuous)
NS-NS		
initial design	(0.06; 0.07; 0.07)	(0.2; 0.2; 0.2)
xylophone	(0.2; 0.2; 0.2)	(0.7; 0.8; 0.8)
BH-NS		
initial design	(0.4; 0.5; 0.5)	(1.1; 1.3; 1.3)
xylophone	(0.9; 1.1; 1.1)	(2.1; 2.4; 2.5)
BH-BH		
initial design	(30.3; 36.1; 37.6)	(99.1; 116.0; 120.2)
xylophone	(45.8; 54.9; 57.2)	(136.7; 160.8; 166.8)
TOTAL		
initial design	(30.8; 36.7; 38.2)	(100.4; 117.4; 121.7)
xylophone	(46.9; 56.2; 58.5)	(139.5; 164.2; 170.1)

Table 7.1: Expected numbers of lensed GW events from inspiralling DCOs of different classes under different evolutionary scenarios. Predictions for the Einstein Telescope in the initial and “xylophone” configuration. Table taken from [8].

of the ray bundles [139].

Considering the wave optics approximation, due to the dependence of the lensing magnification on the mass of the lens, effects caused by lens objects with small masses more often can be considered negligible, but the most concerning effects on the signal appear as the mass approaches $\sim 1000M_{\odot}$ [20]. This introduces errors that would need to be taken into account when doing parameter estimation of the waveforms; the standard tools, like Markov Chain Monte-Carlo(MCMC) are mentioned in chapter 3. So adjustment for the process to include the lensing parameters is necessary.

For the case of a point mass, the parameters which describe the lens are M_{lz} and y , which are the red shifted lens mass and the source position respectively. If these two

parameters were known before hand, and it is only desired to determine the wave signal parameters; the error would not be much more different than just trying to determine the unlensed case, with an increase of difficulty due to the lens modification [20]. If the opposite is true and the wave signal parameters are known then determining the lens parameters would lead to an error around 20 – 100% [20]. Which makes the obtaining any information of the lens unlikely, but a strong correlation is present on the lens set of parameters, and if other information is available about the mass or the source position, it will be possible to find the other one. But of course these are not the usual cases; in the majority of situations, little information about is know apriori.

Fortunately, the strong correlation between the lens set of parameters, and a lack of correlation with the signal source parameters allows to treat them individually, and the the properties of the separated cases can be used. Of course this brings, the same problems if trying to obtain information of the lens; here is were the importance of an optical counterpart would be important, for the source or the lens. For example, optical information leading to an estimate of the lens mass could allow to confirm its distance [20].

But this is not the only effect existent. Another which is present in the estimation and which could result in a different challenge is the existence of a degeneracy in the mass of the binaries, M , and the redshift, z . The problem is important for stellar mass BH-BH mergers more than for NS-NS; the latter could produce an electromagnetic counterpart that would help to break the degeneracy. But without other ways to break the degeneracy, BH mergers produce a physically identical response in a gravitational wave detector to an unlensed merger with a lower intrinsic redshift and larger intrinsic mass scale while the other dimensional parameters remain unchanged. By considering only geometric optics, the strain amplitude of the gravitational wave is modified by $\sqrt{\mu}$ [81, 121]. Trying to fit parameters to a waveform ignoring if this is lensing could lead to an intrinsic mass $\tilde{M} \neq M$ and an intrinsic redshift $\tilde{z} \neq z$. Due to lensing not affecting the frequency, the mass-redshift degeneracy is $\tilde{M}(1 + \tilde{z}) = M(1 + z)$ [28]. This could affect the calculated luminosity distance by re-scaling as $d_L(\tilde{z}) = d_L(z)/\sqrt{\mu}$. This does not affect the wave frequency, but it leads to an incorrect estimation of the

cosmology used on the parameter fitting. It would cause that apparently high-mass

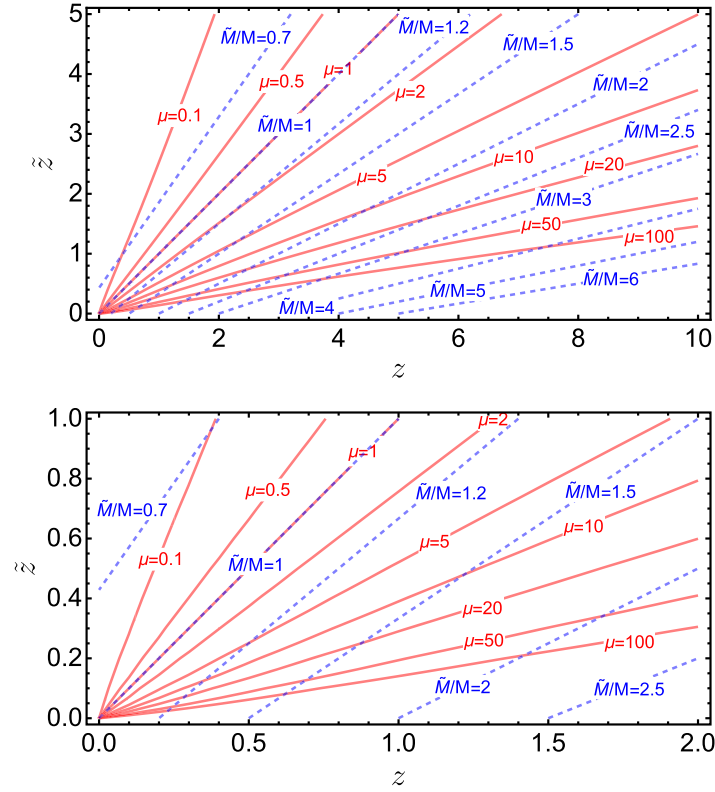


Figure 7.2: The top panel shows the mapping of the intrinsic redshift z and the inferred redshift \tilde{z} for contours of constant magnification μ , red lines, and fixed ratios of inferred and intrinsic mass \tilde{M}/M . The bottom panel shows the same plot but for lower redshifts. Taken from [28].

mergers from low redshifts as an artefact of lensing magnification [28].

Figure 7.2 shows the mapping of the intrinsic redshift and the inferred redshift for several values of the magnification μ and mass relations. The red lines mark contours for constant magnification which can clearly show that for a selected ratio of masses of inferred and intrinsic masses could lead to a lower redshift value, the blue dashed lines. This is dependent on the cosmology which is assumed to be a flat Λ CDM for $\Omega_m = 0.27$ and $h = 0.7$ [28]. The unlensed case is the $\mu = 1$ line which agrees with $\tilde{M}/M = 1$ giving the correct value of redshift. Thus, in cases like this an electromagnetic

counterpart would be needed or multiplicity of the images. The importance of the latter becomes apparent because even for estimations which do not consider the strong lensing, because they will best-fit the sky location and dimensional parameters for the multiple images [27]. These effects should be taken into consideration when carrying out parameter estimation.

For the recent gravitational wave detections the exercise was carried out to determine the likelihood of any of the signals being lensed [1], and it was found to be unlikely with odds of $\sim 10^5 : 1$. If another lensed signal existed, it should arrive 3 years after detection [112]. The majority of these studies have been done considering a point mass lens, and it has been interesting to consider the important characteristics of the lens. Carrying out the analysis using different type of lens could be an important way to use lensing to investigate other problems, such as the nature of Dark Matter [53, 18]. The following section will present some other lensing results for the case of a lens that consist of the soliton core.

7.1.3 The soliton lens revisited

In the previous chapter the basic formalism for wave optics approximation was introduced including several lens models, and a description for a soliton lens model was introduced. This section will focus solely in its features. The soliton unlike the point mass and the Singular Isothermal Sphere (SIS) has three lensing parameters, w , y and k_s which are the adimensional frequency, the adimensional source position and the surface density ratio. The first two parameters appear in other profiles, but this time they are normalized by the characteristic radius r_s of the soliton, which contrasts with the Einstein radius for the point mass and SIS. Nevertheless, the soliton does not have a definition of mass of the lens, as with the point mass lens or the SIS, and in this case k_s becomes a factor which helps to set a mass definition. In a similar fashion as with the point mass and SIS, for the soliton we select $w = 4M_{solz}\omega$ where a definition for effective redshifted lens mass is

$$M_{solz} = M_{sol}(1 + z_l), \quad (7.3)$$

and

$$M_{sol} \equiv \frac{\pi \rho_s r_s^3}{k_s}. \quad (7.4)$$

z_l is the redshift of the lens, ρ_s , r_s are the central density and characteristic radius of the soliton. The definition by itself might seem redundant due to k_s containing the last two quantities already, but in fact, it becomes a mathematical artefact. k_s tells how many times the soliton exceeds the critical superficial density. In turn, the product $\rho_s r_s^3$ can be thought of an intrinsic mass M_i of the soliton. Therefore, by choosing to represent the effective mass this way, it hides the direct dependence on the geometry of the system and only expresses it as an overall factor without losing information. Here onwards when referring to the soliton lens mass the quantity in question will be that defined in eq. (7.4).

It must be emphasized that k_s is not a physical property of the lensing system. It is a mathematical definition which appears due to the normalization. If the Einstein radius could be obtained analytically and used as normalization for the equations, the real physical parameters such as the frequency and source position would be the only ones involved.

Another clear difference with the point mass and with the SIS, shared with the NFW, is that the dimensionless frequency is proportional to their characteristic radius; therefore, a change in ξ_0 increases $w \sim \xi_0^2$. It is obvious that the extra parameter for the soliton lens acts as a stretching factor of the dimensionless frequency due to $k_s \sim r_s$. Examples of the graphical solution for the lens equation are presented in fig. 7.3.

The first figure presents the case of $k_s = 1$. The condition for strong lensing presented in the previous chapter was that it is necessary to satisfy $k_s > 1.52$. Below this value no Einstein radius can be formed, as seen in fig. 7.3a. Fig. 7.3b represents $k_s = 2$, and the crossing of the axis corresponds to the value of the Einstein radius, and $x = 1$ corresponds to r_s . In this example, r_s is ~ 3.34 times bigger than the Einstein radius, and therefore this means that dimensionless frequency will be 11 times bigger compared to using the Einstein radius as the normalization length. As well, it can be seen the graphical mark of the transition between multiple images and a single image, which is

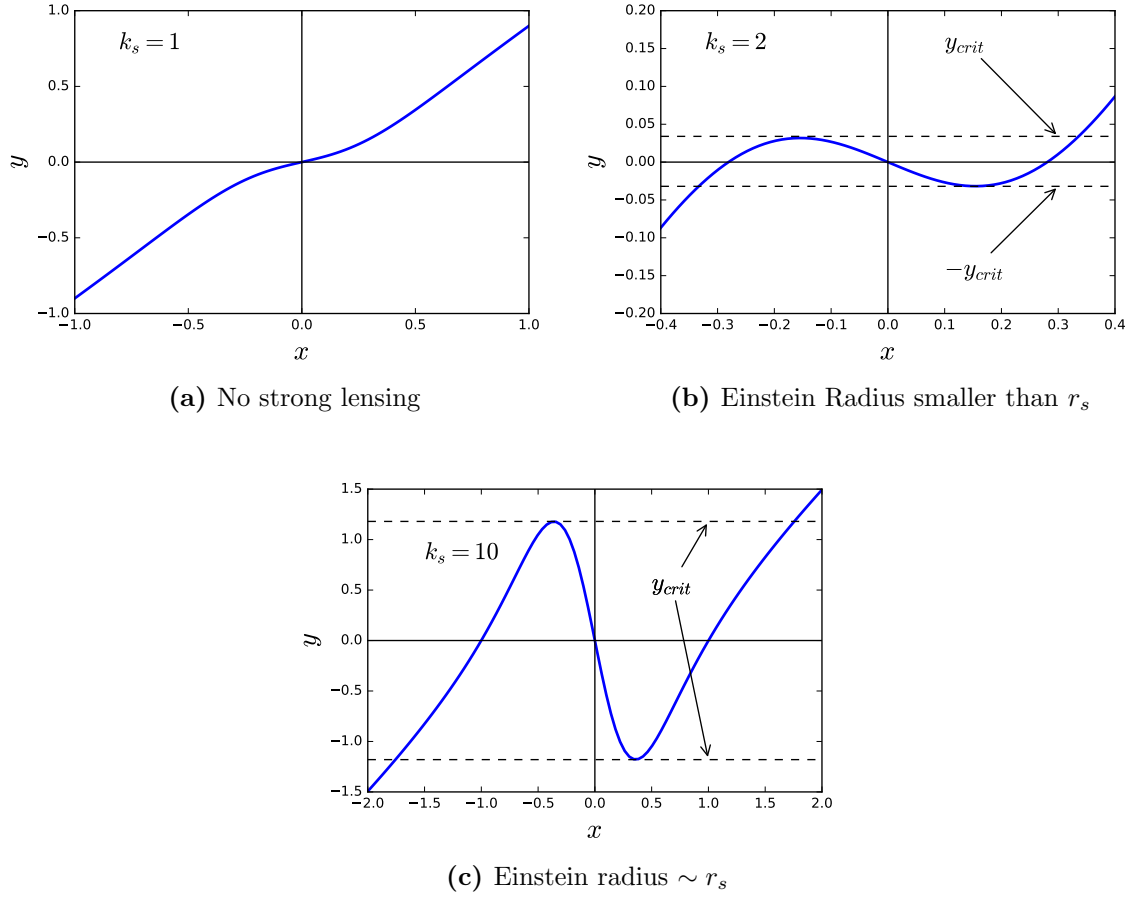


Figure 7.3: The relation of k_s on the lens equation which affects the adimensional frequency. (a) is the case for no strong lensing which is a value below $k_s \approx 1.52$. In (b), $k_s = 2$, there is strong lensing, but r_s is bigger than the Einstein radius which means that w bigger as well. The dashed lines show the transition from multiple to a single image and defines y_{crit} . (c) presents the case for $k_s = 10$ where the Einstein radius $\sim r_s$, and y_{crit} is closer to the unity in this case.

the definition of y_{crit} , and it is obtained numerically. Fig. 7.3c is the case where r_s is of the same size of the Einstein Angle, and here the value of $y_{crit} \sim 1$.

To add more information, in the previous chapter it was presented the amplification factor for several fixed values of y , and it would be helpful to have a general idea how this parameter affects the amplification.

Figures 7.4, 7.5 and 7.6 are a series of density plots for three selected values of k_s .

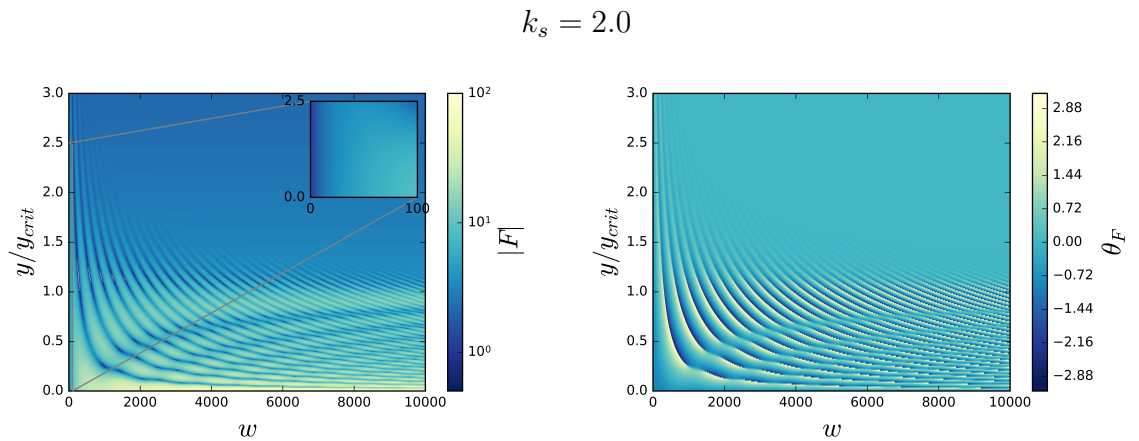


Figure 7.4: Density plot of the amplification factor for $k_s = 2.0$. Left side plot is the amplitude and the right is the phase. Oscillatory regions can be observed due to the multiple image interaction.

They present y as a function of w while the colour represents the amplification factor magnitude, $|F|$, to the left and the phase, θ_F to the right. Figure 7.4 correspond to the value of $k_s = 2$ which has an Einstein radius smaller than the characteristic length of the soliton. Several of the features mentioned earlier can be seen, and the most obvious of them is the size of w is bigger as well. It can be seen that it can extend up to $\sim 10^4$ to appreciate a noticeable decrease of oscillations around the $y/y_{crit} = 1$ which corresponds to the transition from multiple to a single image. This interaction is between three images. The ripples are the oscillatory patterns produced from the diffraction and the image interference.

Another feature is the amplitude of the amplification factor, which could be up to 100 times in certain frequencies and values of y . The phase in comparison has a similar structure of ripples, but this oscillates around a more reasonable value between -3 and 3 .

It was mentioned before that for values above $y/y_{crit} = 1$ only one image is present, so there should be no interference. However, as shown in [126, 121] for the other lens models, there is a diffracted image formed at the lens centre by the diffraction effect, which in turn interacts with the main image, as the value of y and w increases the effect decreases until it can be seen clearly a region to the right of both the amplitude

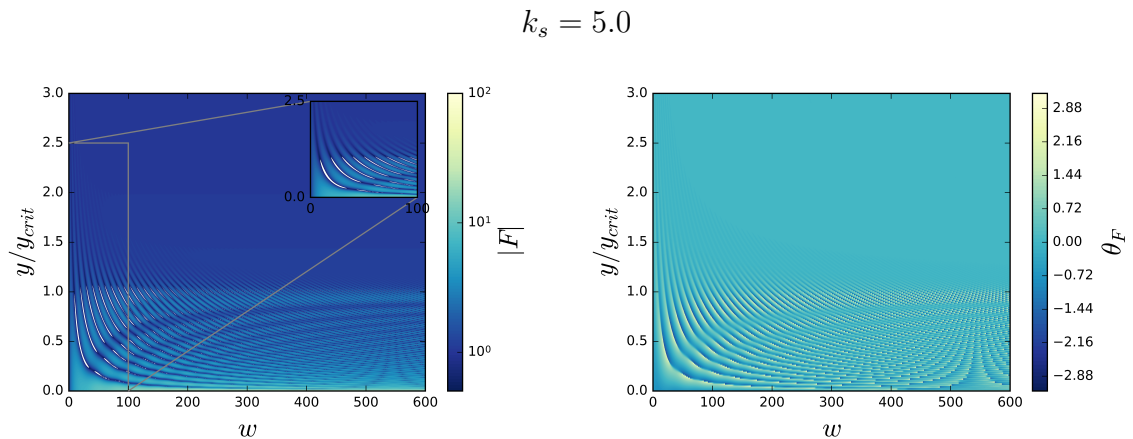


Figure 7.5: Density plots for $k_s = 5.0$. Left image is the amplitude of the amplification factor F , and the right image is the phase. The amplitude has a clear decrease in magnification after $y/y_{crit} = 1$ which is the transition between multiple image interaction and a single image.

and the phase which is where the amplification is in the optics regime.

Figure 7.5 considers the case of $k_s = 5$. The Einstein angle is still smaller than the characteristic radius but clear differences can be observed compared to $k_s = 2$. It can be seen that the interference region is much more well defined around y_{crit} . By comparing using the same colour scale, it is clear that the amplification region is smaller compared with other cases. The interference from the diffracted image of the centre is small too, as can be seen in the zoomed-in region in the amplification map. This is due to the interaction with the inner region being lower by having the Einstein radius at a greater distance from the centre than in the previous case. Another clear difference is that the dimensionless frequency is much more smaller, as was expected. The phase does not have a bigger difference in the maximum range, but it still follows a similar pattern as the amplitude.

The third selected case is $k_s = 10$, and it can be seen in fig. 7.6. Here the Einstein radius is approximately around the characteristic radius, and greater differences can be observed. The first, it is that in this case, the transition from multiple images to a single image is clearly shown; even in the zoomed-in region the value of $y/y_{crit} = 1$ shows minimal interaction above it. The diffracted image at the centre contributes in

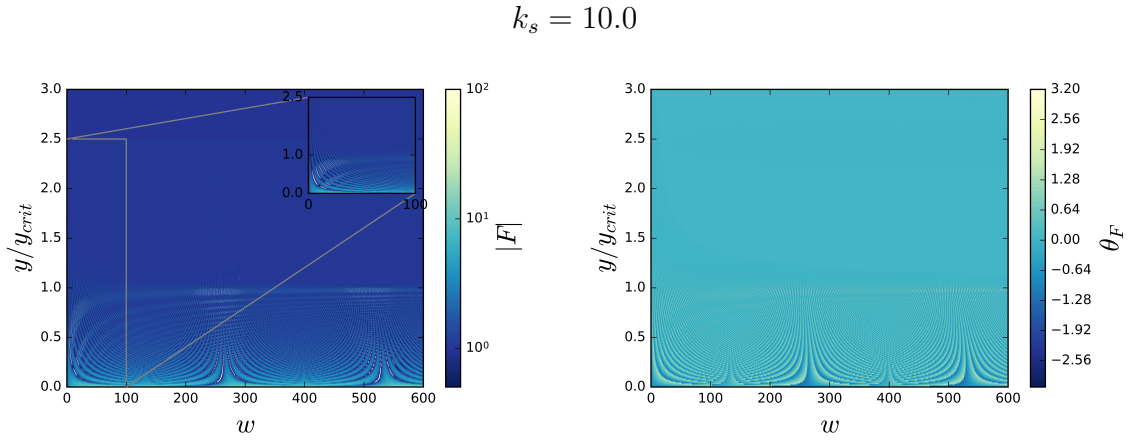


Figure 7.6: Density plots for $k_s = 10.0$. The left and right images are the amplitude and phase of F , respectively. Different from the previous density plots, in this case the Einstein radius is almost the characteristic length of the profile, and low amplification can be observed in general.

a minimal value. The actual amplification in fact it is too small to be appreciated, and only the region of small y gives an appreciable amplification. The phase as well follows a similar pattern as before. By now a general idea can be obtained from the density plots, but it is better to select more specific values, and observe the amplification factor for individual values.

In chapter 6, a similar version of figure 7.7 was presented. In this case, it can be seen clearly that the amplification ranges from 1 up to 30 in the amplitude, and in the case of $y/y_{crit} = 2$ it quickly reaches a consistent value; all of this range has an amplification larger than 2. The source position is normalized by $y_{crit} \approx 0.32$.

For comparison, figure 7.8 presents the same selected values of y . Immediately, it is possible to observe that the maximum amplification has decreased by almost an order of magnitude, but still is considerable for $y/y_{crit} < 1$. In contrast, however, $y/y_{crit} > 1$ has minimal amplification. Nevertheless, the frequency has been reduced. For this case $y_{crit} \approx 0.424$.

The last of the selected values is $k_s = 10$, which corresponds to the Einstein angle being almost the characteristic radius, and has a $y/y_{crit} = 1.18$. On the density plot it was not clear as shown now, but values $y/y_{crit} < 1$ still produce some amplification,

$$k_s = 2.0$$

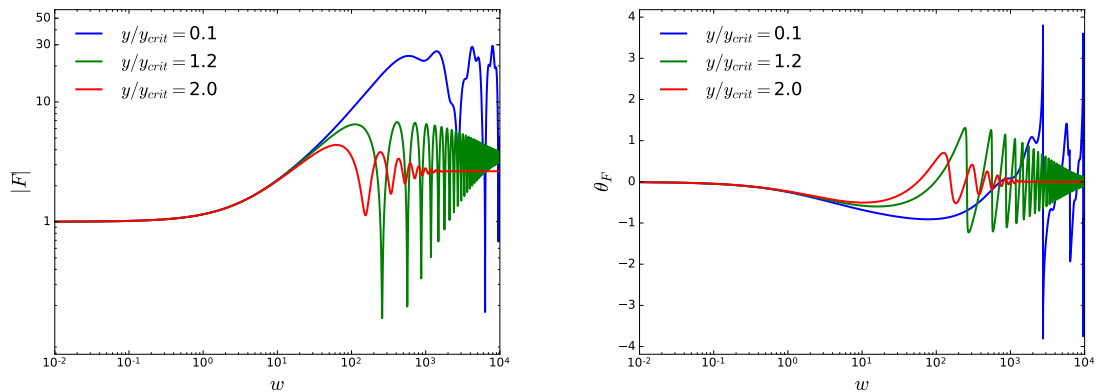


Figure 7.7: Amplification factors for $y/y_{crit} = 0.1, 1.2$ and 2.0 for $k_s = 2$. Left plots are the amplitude, $|F|$ and Right are the phase, θ_F . The overall magnification can be seen to be up to 30 times for the lowest value of y , and it can be seen to be considerable even for bigger values.

$$k_s = 5.0$$

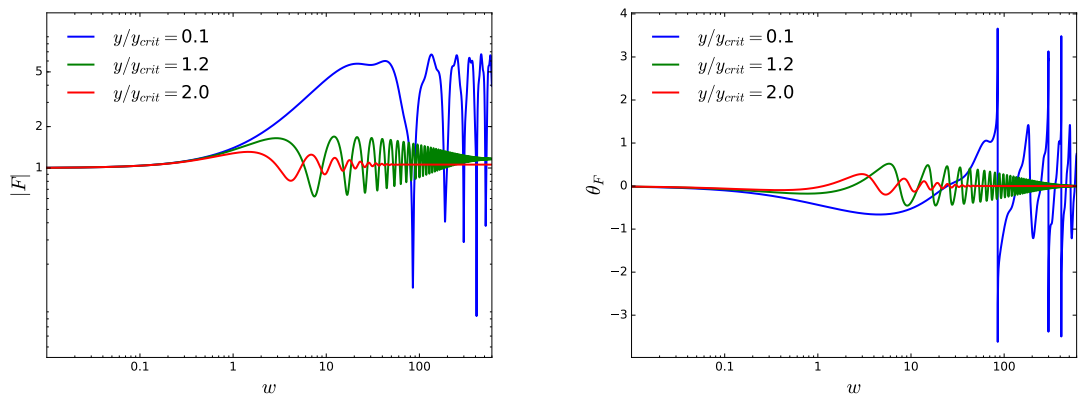


Figure 7.8: Amplification factors for $y/y_{crit} = 0.1, 1.2$ and 2.0 for $k_s = 5$. Left plots are the amplitude, $|F|$ and Right are the phase, θ_F . Compared to the $k_s = 2$ the magnification is an order of magnitude lower, but still significant for the lower value; nevertheless, $y/y_{crit} > 1$ presents magnifications lower than 2. The phase oscillations decrease as well as the magnitude.

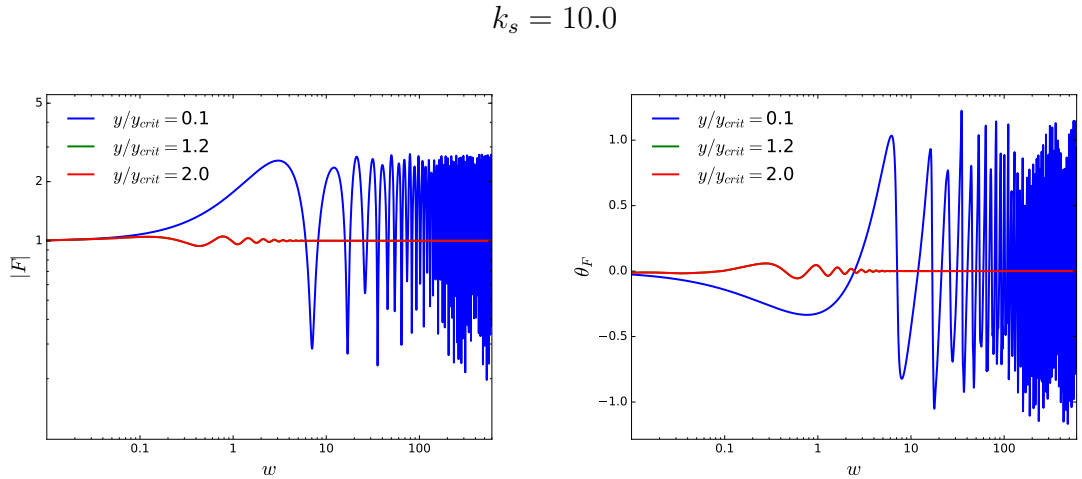


Figure 7.9: Amplification factors for $y/y_{crit} = 0.1, 1.2$ and 2.0 for $k_s = 10$. Left plots are the amplitude, $|F|$ and Right are the phase, θ_F . The overall magnification is slightly greater than 2 for the lowest y , meanwhile any of the values above $y/y_{crit} > 1$ presents no magnification whatsoever, and just small rippling due to the image diffracted by the central region. The phase follows a similar behaviour as the magnitude.

which is barely comparable with the other cases. Unfortunately $y/y_{crit} > 1$ do not have any amplification. This now makes clearer what was seen in the density plot 7.6. From this something important can be deduced, that for the case of $k_s = 10$, only values where multiple images are present should be considered and no amplification can be observed for a single image.

This description of the lens now prepares us to observe how a gravitational wave signal is lensed by this type of lens. This will be explored in the next section.

7.2 Lensing of a gravitational wave

The previous section showed some of the features of the soliton lens. The following section would show how the lens modifies a gravitational wave signal.

The case into consideration is a noise free case, and it does not take into account the antenna pattern of the detector. This approach is chosen because the purpose is to show the effect on the wave itself and not how it affects its detection. Those considerations,

for other lens models, are subject for other works [28, 27, 61] and their extension to the soliton case will be the subject of future work.

7.2.1 Applying the amplification factor

The amplification factor is applied directly to the wave by multiplying it in the frequency domain. This has been done and is shown to be [126, 80, 121]

$$h^L(f) = h(f) \times F(f), \quad (7.5)$$

where $h^L(f)$ is the lensed strain of the gravitational wave. This simple expression is due to the parameters of the gravitational wave and the amplification factor are not correlated [20], and the only parameter shared is the frequency. Taking this into account, the wave source will be fixed, and only the lens will be changed. Earlier in the chapter it was mentioned that there could be several different sources; this creates an ample selection of choices, but for simplicity we select a Black Hole-Black Hole (BH-BH) binary generated from the PhenomD model [50, 55]. With the aim of keeping the interaction simple, the frequency, f , is normalized by the source total mass, M_{tot} , using instead the normalized frequency Mf . This choice makes more obvious the definition of a mass as in eq. 7.4, and allows to write a simple relation between the masses of the source and lens to simplify the units. The relation between Mf and w is given by

$$w = 8\pi Mf(M_{\text{z lens}}/M_{\text{source}}). \quad (7.6)$$

The frequency is modified only by the ratio between the mass of the source and the redshifted mass of the lens.

The generated input waveforms $h(f)$ and $h(t)$ are shown in figures 7.10 and 7.11, respectively. These are used in the rest of the section as the sources to be lensed; its properties are discussed in the next subsection.

7.2.2 Lensed signals

The BH-BH binary will have a simple mass ratio $q = m_1/m_2 = 1$, and total mass $M = m_1 + m_2$, and the spin $\chi_1 = \chi_2 = 0$. Because of the frequency, the real mass

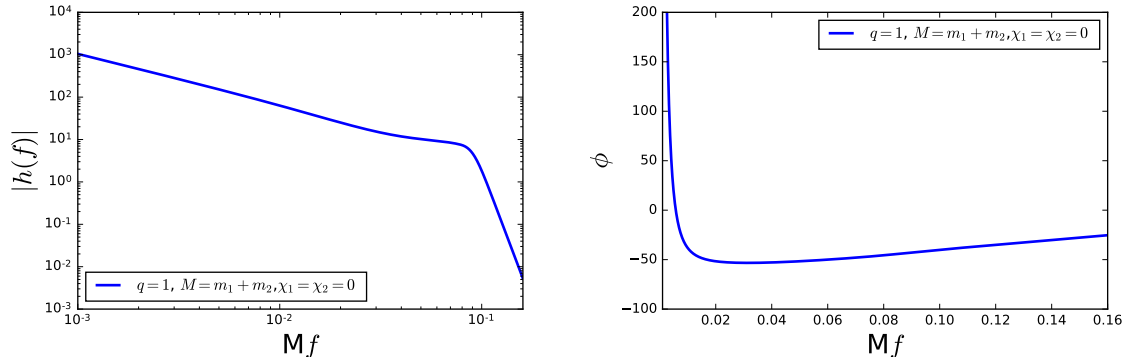


Figure 7.10: Form of the function $h(f)$ which was used as source signal. At the left, it is the magnitude, and at the right the phase. This is the generated source from the PhenomD model.

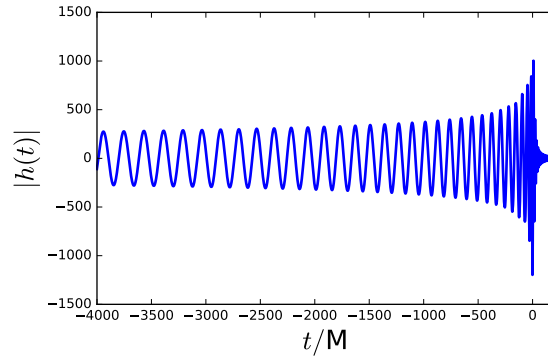


Figure 7.11: Unlensed Source signal, $h(t)$, which is the time domain version of $h(f)$. This is used as the source signal for the lensing.

of the source is not of great importance for now, and only the ratio with the lens mass will have an influence. Because only the relative parameters of the lens are to be compared, it should not be of concern that even for similar lens parameters w and y the physical values could be completely different. In fact, it would be helpful to discern the underlying properties on the lens.

Fig. 7.12 shows the simpler case in the frequency domain by having the ratio of redshifted lens and source mass, $M_{\text{lens}}/M_{\text{source}} = 1$, presented in comparison with several different lens models, including the point mass lens the SIS and the soliton with three selected values of $k_s = 2, 5$ and 10 for a $y = 1$. The frequency range was

$$M_{z\text{lens}}/M_{\text{source}} = 1, y = 0.1$$

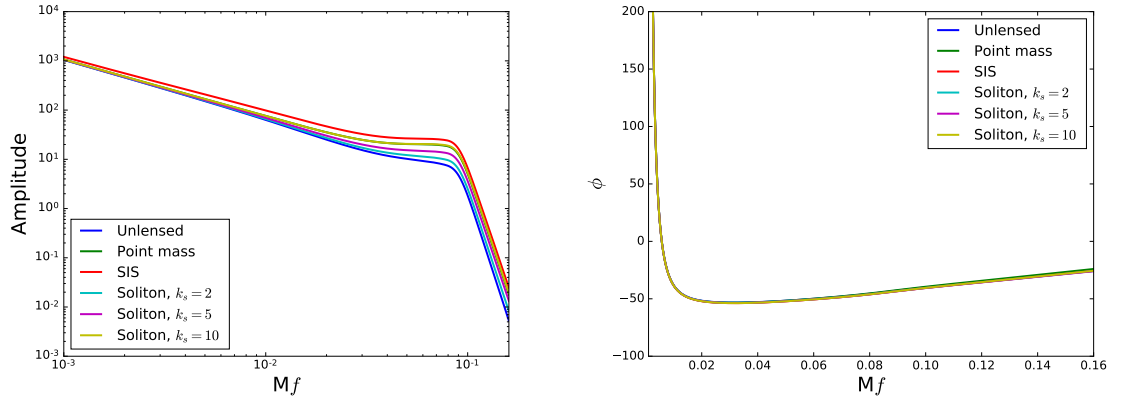


Figure 7.12: Comparison of different lens type waves against unlensed by considering lensed mass equal to the source mass and $y = 0.1$. The left plot is the amplitude, and the right is the phase of the wave. Only the amplitude shows and magnification.

selected to be between $10^{-3} < Mf < 0.16$ to contain the merger-ringdown region. For a ratio of masses of 1 this translates into a dimensionless frequency of $0.025 \lesssim w \lesssim 4.02$. It is clear that the only three models that have a significant amplification over this region are the point mass, SIS and the soliton $k_s = 10$. Although it is not for the same value of y , the expected order of magnitude for the amplitude can be appreciated to start at similar values as seen in figures 6.2, 6.3 and 7.9. The phase of the wave does not suffer any significant modification, and all the examples share a similar phase. The case of the soliton $k_s = 10$, again shows some interesting behaviour, because it is clear that it shares a similar behaviour as a point mass, which means that during parameter estimation this could lead to a difficulty to discern between the two lenses without an assumption about the possible object before hand or at least over the general properties of the type lens [61].

To compare how it changes for higher masses, fig. 7.13 shows the amplitude for the same mass ratio, but for $y = 1.2$ and $y = 2.0$. The first case shows a very low magnification but differences are clearly seen. The region of merger is where the majority of this is appreciated, but at a bigger y any amplification would be difficult to observe and, effectively, the amplified waves are only slightly different than the

$$M_{z\text{lens}}/M_{\text{source}} = 1$$

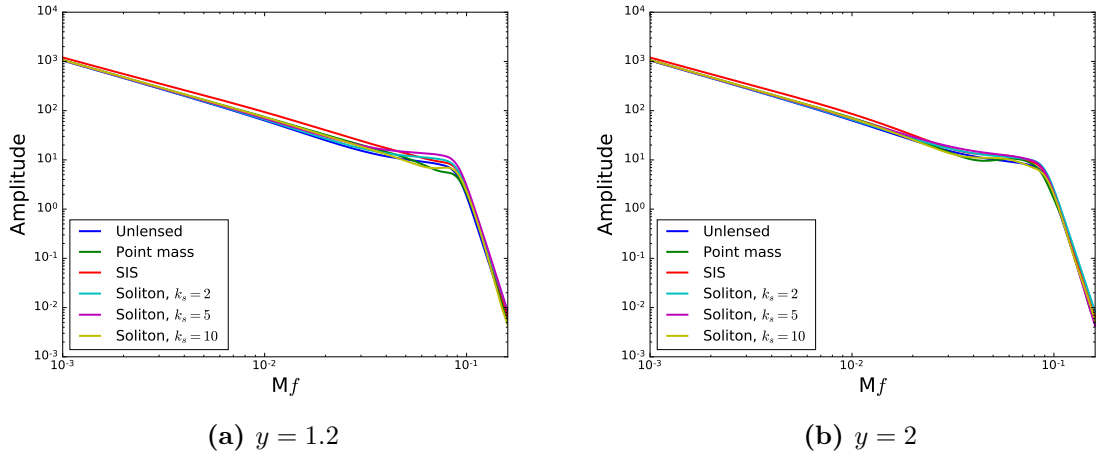


Figure 7.13: Comparison of the magnification amplitude for source positions $y = 1.2$ and $y = 2$ for a ratio $M_{z\text{lens}}/M_{\text{source}} = 1$.

unlensed wave.

In comparison, other than a slight change in the merger region, the actual amplified wave shows no discernible difference from the unlensed waves. This is as it should be expected in view of the size of the mass lens.

The situation is expected to change if a lens of bigger mass is present. Considering a ratio of $M_{z\text{lens}}/M_{\text{source}} = 100$ satisfies the condition of $mr \gtrsim 1$ without problems. The effect of a bigger mass can be immediately seen in fig. 7.14, which considers for comparison the value of $y = 0.1$, and the same conditions as before for the lenses. The range of dimensionless frequencies to cover is $2.5 \lesssim w \lesssim 402$, which changes the shape of the lensed waves significantly. The amplitude of the wave is clearly different for every profile, they have an oscillatory pattern in the frequency which has already been seen present in the amplification factor. The Point mass and SIS have similar behaviour as well as closely related the soliton with $k_s = 10$. In this case the major amplification is the case of soliton $k_s = 2$ which as expected has the greatest of all, but this is only the case for higher frequencies. No oscillatory pattern is distinct, but the inspiral wave is clearly amplified compared with the unlensed case. The phase shows a slight ripple,

$$M_{z\text{lens}}/M_{\text{source}} = 100, y = 0.1$$

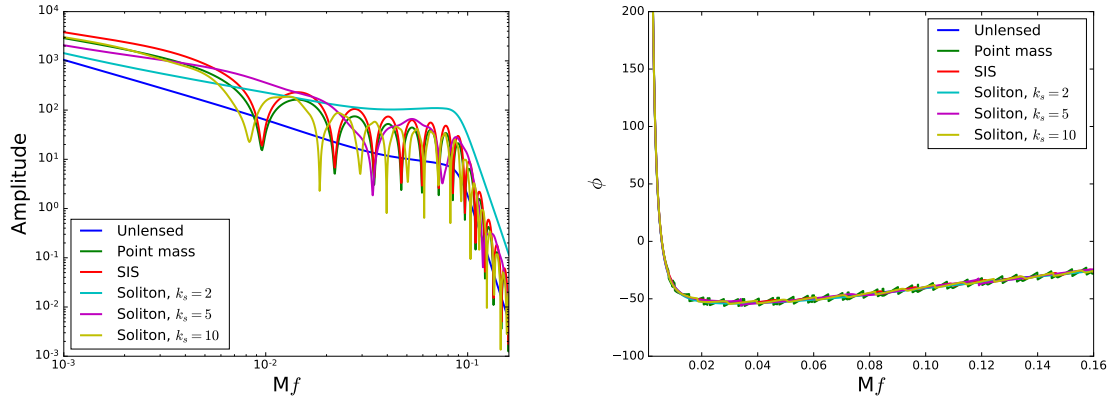


Figure 7.14: Comparison of different lens type waves against unlensed by considering a lens a 100 times the mass of the source, and a position of $y = 0.1$. The left plot is the amplitude, which clearly shows a big magnification and oscillatory pattern from the magnification factor. The right is the phase of the wave. Compared with the amplitude, the phase presents oscillations, but they do not show any significant modification for the unlensed case.

which in practical terms could be still considered the same as the unlensed phase and there is no appreciable change. The importance of the mass is now clear. Which means that bigger masses act as better lenses.

To compare how the effect of the source position changes this, fig. 7.15 shows $y = 1.2$ and $y = 2$. The latter case only has the ripples which do not change effectively the amplitude of the wave, and only the soliton $k_s = 2$ produces an appreciable change. $y = 1.2$ show clearly a lower amplification and in this case, as mentioned before, minimum amplification can be observed, and only the soliton $k_s = 2$ produces a significant contribution.

Despite the majority of the work being carried out in the frequency domain, it is insightful to observe what changes happen in the time domain. Figure 7.16 exemplifies this. It shows the unlensed wave compared to the wave lensed by the soliton lens for $M_{z\text{lens}}/M_{\text{source}} = 100$. Figure 7.16a shows the amplitude of the strain h for $y = 0.1$ which was previously the example which clearly modified the original unlensed wave,

$$M_{z\text{lens}}/M_{\text{source}} = 100$$

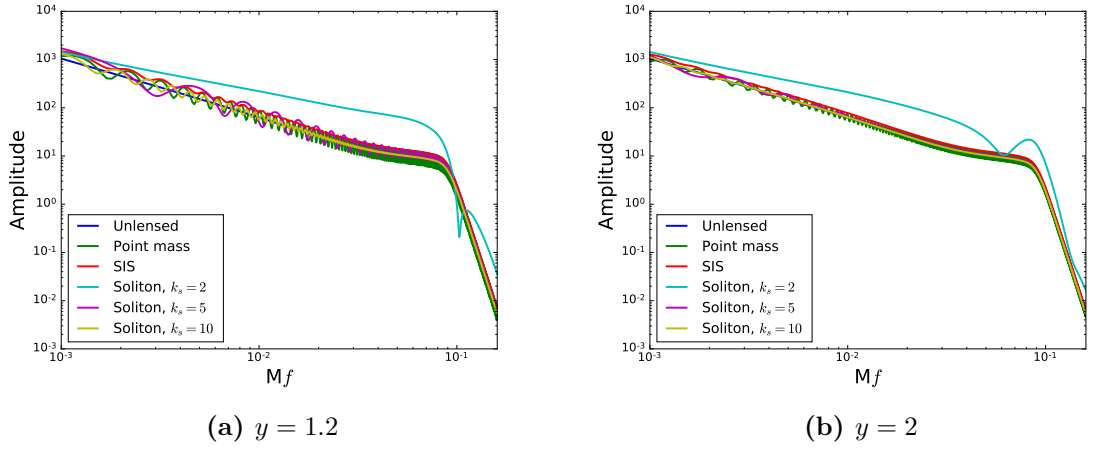


Figure 7.15: Comparison of the magnification amplitude for source positions $y = 1.2$ and $y = 2$ for a ratio $M_{z\text{lens}}/M_{\text{source}} = 100$.

and in the time domain this is the same case where if compared with fig. 7.16c, it looks like a completely different wave. Figure 7.16b, which is the case of $y = 2$, does not show any appreciable change, but of course the majority of the information would be obtained from the frequency domain.

The several changes that the lens can produce in the time or frequency domain shown in this work are only for demonstration purposes of the soliton mass profile. A more complete exploration of the effects of lensing on parameter estimation and other more in detail analysis are left for future work.

Cosmography of the lenses

It is important to obtain a general idea of how the lenses affect the wave form, but this is not the only purpose. The problem of lensing of gravitational waves has several stages; for example, it needs to be examined if the wave is lensed or not. Considering a gravitational wave signal that has indeed been affected by lensing, the lensing parameters need to be determined. Even where different lens models share two or more parameters, the best-fit values of the parameters will change depending on the model

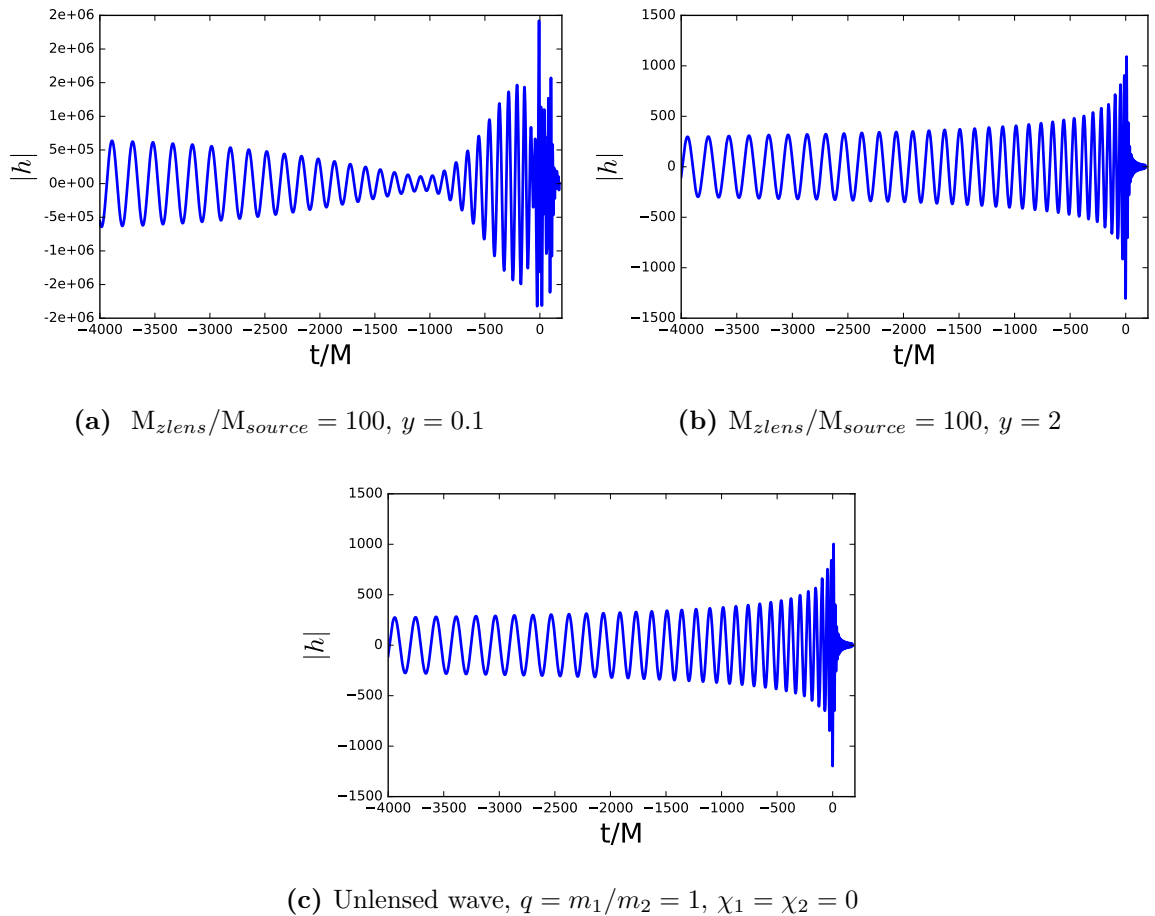


Figure 7.16: Gravitational wave in the time domain. The axes are the normalized time with the source mass, and the amplitude of the strain h . a) Shows the time domain version of the amplitude of fig. 7.14. It is clear that there is an major modification on the wave. b) Corresponds to the time domain version of the amplitude of fig. 7.15 for $y = 2$ where there is no change if compared c), which is the unlensed wave with parameters $q = m_1/m_2 = 1, \chi_1 = \chi_2 = 0$.

selected, which by itself reveal important information about the nature of the lens. Once that the model as appropriate, information on the model parameters needs to be extracted from the data.

The purpose for the rest of this chapter is not to address these stages, which should be left to future work, but to compare and give a first insight about how the different models might be suitable for consideration for either ground-based detectors such as

LIGO or for space-based detectors such as LISA. The reason of this is because the majority of works done, as mentioned earlier have been considering a point mass lens, which of course as we have shown is not the only case possible, and only very recently other works started to address how the lensing signatures are affected by comparing different models [61].

As a simple example, consider a lensing system where the lens is midway between the observer and the source, which gives the angular diameter distances as $D_L = D_{LS}$ and $D_S = 2D_L$, which in turn fixes the relative position of the lens by considering where the source is located. This is one of the simpler cases, and there are several works which address the distribution of gravitational-wave sources [85, 25, 65]. We make use of the results of those analyses, even though they were carried out for different lens models, since the purpose of the section is not to address the impact of a full estimation but only to give some insight about the future expectations.

The rest of this chapter will, therefore, treat 2 cases in which compares the previous shown models. The NFW model is not considered because it would require a more in-depth analysis, and it is desired to show details for the soliton profile rather than the standard universal model.

The first situation to address would be to use similar given physical values for the lens parameters and investigate which models would be more likely to give an adequate description of the observations. In this case, apart from the fixed system position, the shared values would be the lensing parameters w and y as well as the normalization length ξ_0 , and from them we can obtain the information and compare between the models. The mass ratios and values of y will be the same as used in the previous section unless stated otherwise. Reasonable distances for the normalization radius would be $\xi_0 \approx 10\text{kpc}$ which represents an Einstein radius or a characteristic radius as from chapter 5 This value is of the order of magnitude of small galaxies, if it is desired to use for the soliton profile case.

From [85, 61], a source position of $z \approx 0.2$ is expected to have a change due to lensing effects, so this will be the selected redshift for the source. Now, it is possible to give physical values to the dimensionless quantities, so the proper units for the Newton's

constant, G , and speed of light, c , will be restored for this purpose. The assumed cosmology will be the standard Λ CDM with $H_0 = 67.74 \text{ km}^{-1}\text{s}^{-1}\text{Mpc}^{-1}$, $\Omega_{BM} = 0.0486$, $\Omega_{DM} = 0.2589$ and $\Omega_{\Lambda} = 0.6911$ [94].

For a redshift of $z = 0.2$, the angular diameter distance is $D_S = 702.5 \text{ Mpc}$ which gives $D_L = D_{LS} = 351.25 \text{ Mpc}$, which in turns correspond to a redshift of the lens of $z_L \approx 0.088$. These are all the required values.

From the different lensed waves, the strongest effect is appreciable for $y = 0.1$, so this will be the chosen example. The obtained values the lenses and their parameters are compiled in table 7.2. This information gives an idea of the type of objects described by the lens. For the different lenses, it is possible to do an educated guess about what is the object which is described.

Considering the point mass is clearly a super massive black hole, meanwhile the SIS has a dispersion velocity, σ , that is comparable only with globular clusters, which for the source distance is quite unlikely [115]. The case of the soliton is comparable with dwarf galaxies [21], which for the distances of the system are a better option. Nevertheless, if the object indeed acted as a lens, considering the masses of the lenses they have $M_{lz} \sim 10^{12} M_{\odot}$, which for the ratio $M_{zlens}/M_{source} = 100$, would produce the smallest source mass around $M_{source} \sim 10^{10} M_{\odot}$. For this masses, the possible sources would be of the order of Super Massive Black Holes (SMBH), which could only be seen by Space Telescopes like LISA [107]. The last row on table 7.2 compares the mass of the different lenses by integrating the density profile around an sphere with the radius of the corresponding Einstein radius,

$$M_{sph}(r) = 4\pi \int_0^r \rho(s) s^2 ds. \quad (7.7)$$

For the soliton, this is given by [41],

$$M_{sol}(x) = \frac{\rho_s r_s^3}{215040 (x^2 + 1)^7} \left[3465 (x^2 + 1)^7 \tan^{-1}(x) + x (3465x^{12} + 23100x^{10} + 65373x^8 + 101376x^6 + 92323x^4 + 48580x^2 - 3465) \right]. \quad (7.8)$$

The previous example was easy to address because the normalization length was provided beforehand. The second case considers the selected source mass and to have iden-

	pm	SIS	Sol, $k_s = 2$	Sol, $k_s = 5$	Sol, $k_s = 10$
ξ_0			10 kpc		
η/kpc			2 kpc		
R_E/kpc	10	10	2.81	6.81	10
Parameters		σ 638 km/s		r_s 10 kpc	
		$\rho_s/(\text{M}_\odot\text{pc}^{-3})$	1.89	4.73	9.46
$M_{z\text{lens}}$			$3.23 \times 10^{12} \text{M}_\odot$		
$M_{\text{sph}}(R_E)/\text{M}_\odot$	2.97×10^{12}	1.89×10^{12}	1.23×10^{11}	1.26×10^{12}	2.93×10^{12}

Table 7.2: Mass and physical parameters for the different lenses by considering similar source position of $y = 0.1$ and a normalization length $\xi_0 = 10\text{kpc}$.

tified the lens as a soliton lens; from which, it is desired to retrieve physical information from the compared lens parameters. As in the previous example $y = 0.1$, $k_s = 2, 5$ and 10 . Again due to the lens effects being stronger for high ratios, $M_{z\text{lens}}/M_{\text{source}} = 100$, this will be the ratio selected. The previous example was better suited for a Space-based telescope, therefore, a reasonable source of $M_s = 100 \text{M}_\odot$ will be used to compare with a Ground-based telescope. The geometry of the system and redshifts will be the same as before. The different physical parameters are presented in table 7.3.

It is clear from the characteristic radius size and density that this is not the appropriate description for the lens [114]. The mass inside the Einstein radius is shown too. From this example, it is clear that the soliton needs to have a several orders of magnitude bigger ratio with the source to be effective as a description of a lens. From the previous two exercises, there are two points that can be extracted. The first is that for sources detectable by space-based detectors, the soliton have a reasonable parameters to not be discarded on the study for appreciable lensing effects. The second is that for small sources, unless observed by other technique, it is not clear that the soliton profile would be adequate for this type of sources, therefore, affect the waveforms observed by ground-based detectors.

	Sol, $k_s = 2$	Sol, $k_s = 5$	Sol, $k_s = 10$
M_s		$100M_\odot$	
$M_{z\text{lens}}$		10^4M_\odot	
r_s		0.556 pc	
$\rho_s/(M_\odot\text{pc}^{-3})$	3.4×10^4	8.5×10^4	1.7×10^5
R_E/pc	0.16	0.379	0.556
$M_{\text{sph}}(R_E)/M_\odot$	724.6	4.26×10^3	9.2×10^3

Table 7.3: Mass and physical parameters for a soliton lens with a BH-BH source with total mass of $100M_\odot$

7.2.3 Summary

The beginning of this chapter presented a brief review of the effects of gravitational wave lensing. Using it as a motivation, it introduced an analysis of a soliton core as a gravitational lens for a gravitational wave signal. Furthermore, it compared it with other lenses and finally showed some examples of information that is possible to extract from them.

The main results from the comparison of the gravitational wave signal are that a lens can modify it significantly to the point it looks completely different from the unlensed signal. This situation arises due to the relative sizes of the source and the lens. Furthermore, except for special cases, lens models in general can be distinguished from each other. The introduction of a lens indeed can change the signal, especially for when the lens has a mass a hundred or more times bigger than the source.

The last section presented examples of possible information obtainable from the soliton core, point mass or SIS lens models. The first example compared the adequacy of each model where a lens signal is assumed and the second considers only the soliton case. The former being in the range of spaceborn while the latter for ground-based detectors. Furthermore, it was found that the soliton lens model represents more adequately a galaxy in the spaceborn case. Nevertheless, the work done in this thesis

is presented only as an introduction of the soliton core model as an extended mass distribution. Therefore, a complete Bayesian analysis is left for future work.

Overall, the chapter emphasizes the importance of the study of gravitational wave lensing to help in the detection of signals. In particular, it focuses on the soliton core lens properties. The studies of point mass and extended mass distributions acting as a lens are expected to gain importance in the future once a lensed signal is detected.

Chapter 8

Concluding remarks and future work

The global idea behind this thesis was to explore the viability of Scalar Field Dark Matter, in particular ψ DM, as an alternative model for the description of Dark Matter - for which the standard paradigm is Cold Dark Matter. For this purpose, strong gravitational lensing was selected as a tool. Then three questions were implicitly posed:

- *what are the basic properties of a wave dark matter lens?*
- *how well do observations constrain the parameters of the wave dark matter model?*
- *What can we say about the use of the wave dark matter lens as a lens of gravitational waves?*

The first question was addressed in chapter 4. Here a derivation of the necessary analytical functions, i.e. lensing mass or surface mass density, was presented with their related lensing properties. In the same manner, two configurations were detailed: a soliton profile and a soliton core + NFW tail. The former configuration was a particular case of the latter when the core extends to larger radii.

The second question was analysed and discussed in chapter 5. In essence, by using a small sub-sample of galaxies from the galaxy lensing catalogue SLACS, a parameter estimation was carried out in order to constrain the values required to reproduce the

observational data. The sub-sample was selected taking into consideration galaxies with half or more of the content as Dark Matter; this was done to reduce any biases of the baryonic matter. In principle, the idea behind the data sub-sample was a proof of concept for the study and effect of the lensing parameters for the Wave Dark Matter profile.

From this analysis it was found that, for the sizes of the galaxies considered, the soliton core must represent a compact and dense object if it is to adequately describe the observed properties of the lensed galaxies. Meanwhile, the soliton + NFW tail configuration is able to represent more successfully a galaxy; nevertheless, it is not possible to constrain the characteristic length of the NFW tail and only a minimum threshold can be established.

The third question was briefly introduced in chapter 6 and was the main objective of 7. To clarify, only the soliton core was considered in those chapters because it represents the major contribution to the mass compared with the NFW tail and it has a simpler formulation.

Overall, from the examples presented, it was shown it is more likely to observe a lensed signal with space-based detectors, from a lens that is a galactic-sized objects. In such a case it should be possible to use the information about the lens parameters derived from the gravitational wave data to determine the suitability of a Wave Dark Matter object.

This work has contributed to the literatures by deriving a mathematical functions that form the bases of the soliton+NFW tail profile for the Wave Dark Matter lens; these functions can be used to predict and study the lensing signatures for this model. Furthermore, the proof of concept results obtained in this by comparing the Wave Dark Matter lens model with observational data for several lensed galaxies agree with the range of axion masses reported in the literature, at least for the case of a soliton+NFW tail. This work has also introduced another dark matter profile to the growing field of research on the lensing of gravitational wave - were the modelling of extended mass distributions in this regime is still in development. Additionally, our results for the lensing of gravitational waves by Wave Dark Matter lenses are in good agreement with

the expected range of lensing galaxy masses that have been presented in the few works that discuss it in the literature that have considered extended mass distributions.

The results presented in this thesis can be considered as a first approach to the use of the Wave Dark Matter model as lens. Future researchers who work with this model can therefore add another tool to include in their description of galaxies, adding to the perspective of electromagnetic observations of lensing. Likewise, because this work considers the case of gravitational wave lensing, not only has presented an opportunity to study the possibility of detection of this phenomenon, but also to compare with an electromagnetic counterpart - should that also be observed.

On the other hand, our work is limited in some respects - e.g. by the small sample of lensed galaxies that we have considered, and by the simple and somewhat qualitative description of the gravitational waves parameters that we have presented. Additionally the scope of the study was only in to consider the strong lensing regime. The work presented here, therefore, opens the door for several other possible future analyses and comparisons. For example, a combination of galaxy dynamics and lensing could be possible, and could increase the opportunity to constrain the profile parameters. Moreover, it would be beneficial to explore, in addition to the lensing amplification, the deformation of an extended source caused by the lens - and to expand the analysis into the regime of weak lensing.

For the case of gravitational waves lensing there are also multiple future opportunities - including a Bayesian model comparison between different lens models, analysis of the population of lenses and a full simultaneous estimation of both lens and source parameters. As the study of gravitational wave lensing develops, and a lensed signal is detected, these further analyses will be both appropriate and necessary.

In any case, it will be interesting to consider if Scalar Field Dark Matter models gain further momentum as observations that combine light and gravitational waves become available. It is hoped that these future studies might give deeper insight into the elusive component of the universe known as Dark Matter, so that a better understanding of the universe can be reached at the end.

Bibliography

- [1] B. P. Abbott, R. Abbott, T. D. Abbott, M. R. Abernathy, F. Acernese, K. Ackley, C. Adams, T. Adams, P. Addesso, R. X. Adhikari, and et al. Astrophysical Implications of the Binary Black-hole Merger GW150914. *ApJ*, 818:L22, February 2016.
- [2] B. P. Abbott, R. Abbott, T. D. Abbott, F. Acernese, K. Ackley, C. Adams, T. Adams, P. Addesso, R. X. Adhikari, V. B. Adya, and et al. A gravitational-wave standard siren measurement of the Hubble constant. *Nature*, 551:85–88, November 2017.
- [3] Kenath Arun, S.B. Gudennavar, and C. Sivaram. Dark matter, dark energy, and alternate models: A review. *Advances in Space Research*, 60(1):166–186, 2017.
- [4] M. W. Auger, T. Treu, A. S. Bolton, R. Gavazzi, L. V. E. Koopmans, P. J. Marshall, K. Bundy, and L. A. Moustakas. The Sloan Lens ACS Survey. IX. Colors, Lensing, and Stellar Masses of Early-Type Galaxies. *ApJ*, 705:1099–1115, November 2009.
- [5] M. W. Auger, T. Treu, A. S. Bolton, R. Gavazzi, L. V. E. Koopmans, P. J. Marshall, L. A. Moustakas, and S. Burles. The Sloan Lens ACS Survey. X. Stellar, Dynamical, and Total Mass Correlations of Massive Early-type Galaxies. *ApJ*, 724:511–525, November 2010.
- [6] Christian Baraldo, Akio Hosoya, and Takahiro T. Nakamura. Gravitationally

- induced interference of gravitational waves by a rotating massive object. *Phys. Rev.*, D59:083001, 1999.
- [7] M. Bartelmann. Arcs from a universal dark-matter halo profile. *A&A*, 313:697–702, September 1996.
- [8] M. Biesiada, X. Ding, A. Piórkowska, and Z.-H. Zhu. Strong gravitational lensing of gravitational waves from double compact binaries—perspectives for the Einstein Telescope. *J. Cosmology Astropart. Phys.*, 10:080, October 2014.
- [9] A. Blasco. *Bayesian Data Analysis for Animal Scientists: The Basics*. Springer International Publishing, 2017.
- [10] C G Böhmer and T Harko. Can dark matter be a Bose–Einstein condensate? *Journal of Cosmology and Astroparticle Physics*, 2007(06):025, 2007.
- [11] A. S. Bolton, S. Burles, L. V. E. Koopmans, T. Treu, R. Gavazzi, L. A. Moustakas, R. Wayth, and D. J. Schlegel. The Sloan Lens ACS Survey. V. The Full ACS Strong-Lens Sample. *ApJ*, 682:964–984, August 2008.
- [12] A. S. Bolton, S. Burles, L. V. E. Koopmans, T. Treu, and L. A. Moustakas. The Sloan Lens ACS Survey. I. A Large Spectroscopically Selected Sample of Massive Early-Type Lens Galaxies. *ApJ*, 638:703–724, February 2006.
- [13] A. S. Bolton, T. Treu, L. V. E. Koopmans, R. Gavazzi, L. A. Moustakas, S. Burles, D. J. Schlegel, and R. Wayth. The Sloan Lens ACS Survey. VII. Elliptical Galaxy Scaling Laws from Direct Observational Mass Measurements. *ApJ*, 684:248–259, September 2008.
- [14] R. J. Bontz and M. P. Haugan. A diffraction limit on the gravitational lens effect. *Ap&SS*, 78:199–210, August 1981.
- [15] I. S. Bowen and A. B. Wyse. The spectra and chemical composition of the gaseous nebulae, NGC 6572, 7027, 7662. *Lick Observatory Bulletin*, 19, 1939.

-
- [16] M. Boylan-Kolchin, J. S. Bullock, and M. Kaplinghat. Too big to fail? The puzzling darkness of massive Milky Way subhaloes. *mnras*, 415:L40–L44, July 2011.
- [17] A. Burkert. The Structure of Dark Matter Halos in Dwarf Galaxies. *The Astrophysical Journal Letters*, 447(1):L25, 1995.
- [18] R.-G. Cai, T.-B. Liu, and S.-J. Wang. Gravitational wave as probe of superfluid dark matter. *ArXiv e-prints*, October 2017.
- [19] Shuo Cao and Zong-Hong Zhu. Constraints on cosmological models from lens redshift data. *Astron. Astrophys.*, 538:A43, 2012.
- [20] Zhoujian Cao, Li-Fang Li, and Yan Wang. Gravitational lensing effects on parameter estimation in gravitational wave detection with advanced detectors. *Phys. Rev.*, D90(6):062003, 2014.
- [21] Shu-Rong Chen, Hsi-Yu Schive, and Tzihong Chiueh. Jeans Analysis for Dwarf Spheroidal Galaxies in Wave Dark Matter. 2016.
- [22] Shu-Rong Chen, Hsi-Yu Schive, and Tzihong Chiueh. Jeans Analysis for Dwarf Spheroidal Galaxies in Wave Dark Matter. 2016.
- [23] Y. M. Cho and Y. Y. Keum. Dilatonic dark matter and unified cosmology: A new paradigm. *Class. Quant. Grav.*, 15:907–921, 1998.
- [24] Sébastien Clesse and Juan García-Bellido. Massive Primordial Black Holes from Hybrid Inflation as Dark Matter and the seeds of Galaxies. *Phys. Rev.*, D92(2):023524, 2015.
- [25] M. Colpi and A. Sesana. *Gravitational Wave Sources in the Era of Multi-Band Gravitational Wave Astronomy*, pages 43–140. World Scientific Publishing Co, 2017.

- [26] Monica Colpi, Stuart L. Shapiro, and Ira Wasserman. Boson Stars: Gravitational Equilibria of Self-Interacting Scalar Fields. *Phys. Rev. Lett.*, 57:2485–2488, Nov 1986.
- [27] L. Dai and T. Venumadhav. On the waveforms of gravitationally lensed gravitational waves. *ArXiv e-prints*, February 2017.
- [28] L. Dai, T. Venumadhav, and K. Sigurdson. Effect of lensing magnification on the apparent distribution of black hole mergers. *Phys. Rev. D*, 95(4):044011, February 2017.
- [29] W. J. G. de Blok. The Core-Cusp Problem,. *Advances in Astronomy*, 2010(789293):14 pages, 2010.
- [30] Kenyon B. De Greene. The Bayesian Way. *Science*, 286(5449):2449–2449, 1999.
- [31] S. Dhawan, S. W. Jha, and B. Leibundgut. Measuring the Hubble constant with Type Ia supernovae as near-infrared standard candles. *A&A*, 609:A72, January 2018.
- [32] X. Ding, M. Biesiada, and Z.-H. Zhu. Strongly lensed gravitational waves from intrinsically faint double compact binaries—prediction for the Einstein Telescope. *J. Cosmology Astropart. Phys.*, 12:006, December 2015.
- [33] Xiaolong Du, Christoph Behrens, and Jens C. Niemeyer. Substructure of fuzzy dark matter haloes. 2016.
- [34] X.-L. Fan, K. Liao, M. Biesiada, A. Piórkowska-Kurpas, and Z.-H. Zhu. Speed of Gravitational Waves from Strongly Lensed Gravitational Waves and Electromagnetic Signals. *Physical Review Letters*, 118(9):091102, March 2017.
- [35] XiLong Fan, Christopher Messenger, and Ik Siong Heng. A Bayesian approach to multi-messenger astronomy: Identification of gravitational-wave host galaxies. *Astrophys. J.*, 795(1):43, 2014.

- [36] F. Feroz, M. P. Hobson, and M. Bridges. MultiNest: an efficient and robust Bayesian inference tool for cosmology and particle physics. *Mon. Not. Roy. Astron. Soc.*, 398:1601–1614, 2009.
- [37] F. Feroz, M. P. Hobson, E. Cameron, and A. N. Pettitt. Importance Nested Sampling and the MultiNest Algorithm. *ArXiv e-prints*, June 2013.
- [38] M. Fich and S. Tremaine. The mass of the Galaxy. *ARA&A*, 29:409–445, 1991.
- [39] R. Gavazzi, T. Treu, L. V. E. Koopmans, A. S. Bolton, L. A. Moustakas, S. Burles, and P. J. Marshall. The Sloan Lens ACS Survey. VI. Discovery and Analysis of a Double Einstein Ring. *ApJ*, 677:1046–1059, April 2008.
- [40] R. Gavazzi, T. Treu, J. D. Rhodes, L. V. E. Koopmans, A. S. Bolton, S. Burles, R. J. Massey, and L. A. Moustakas. The Sloan Lens ACS Survey. IV. The Mass Density Profile of Early-Type Galaxies out to 100 Effective Radii. *ApJ*, 667:176–190, September 2007.
- [41] Alma X. González-Morales, David J. E. Marsh, Jorge Peñarrubia, and Luis Ureña-López. Unbiased constraints on ultralight axion mass from dwarf spheroidal galaxies. 2016.
- [42] A. X. González-Morales, A. Diez-Tejedor, L. A. Ureña-López, and O. Valenzuela. Hints on halo evolution in scalar field dark matter models with galaxy observations. *prd*, 87(2):021301, January 2013.
- [43] PETER J. GREEN. Reversible jump Markov chain Monte Carlo computation and Bayesian model determination. *Biometrika*, 82(4):711–732, 1995.
- [44] P. Gregory. *Bayesian Logical Data Analysis for the Physical Sciences: A Comparative Approach with Mathematica® Support*. Cambridge University Press, 2005.
- [45] Kim Griest. The Search for dark matter: WIMPs and MACHOs. 1993. [Annals N. Y. Acad. Sci.688,390(1993)].

- [46] F. Siddhartha Guzman and L. Arturo Urena-Lopez. Evolution of the Schrodinger-Newton system for a selfgravitating scalar field. *Phys. Rev.*, D69:124033, 2004.
- [47] E. Harrison. *Cosmology: The Science of the Universe*. Cambridge University Press, 2000.
- [48] D. W. Hogg. Distance measures in cosmology. *ArXiv Astrophysics e-prints*, May 1999.
- [49] S. A. Hughes. Listening to the universe with gravitational-wave astronomy. *Annals of Physics*, 303:142–178, January 2003.
- [50] Sascha Husa, Sebastian Khan, Mark Hannam, Michael Pürrer, Frank Ohme, Xisco Jiménez Forteza, and Alejandro Bohé. Frequency-domain gravitational waves from nonprecessing black-hole binaries. I. New numerical waveforms and anatomy of the signal. *Phys. Rev. D*, 93:044006, Feb 2016.
- [51] Vid Iršič, Matteo Viel, Martin G. Haehnelt, James S. Bolton, and George D. Becker. First Constraints on Fuzzy Dark Matter from Lyman- α Forest Data and Hydrodynamical Simulations. *Phys. Rev. Lett.*, 119:031302, Jul 2017.
- [52] H. Iro. *A Modern Approach to Classical Mechanics*. World Scientific, 2002.
- [53] S. Jung and C. S. Shin. Gravitational-Wave Lensing Fringes by Compact Dark Matter at LIGO. *ArXiv e-prints*, December 2017.
- [54] C. R. Keeton. A Catalog of Mass Models for Gravitational Lensing. *ArXiv Astrophysics e-prints*, February 2001.
- [55] Sebastian Khan, Sascha Husa, Mark Hannam, Frank Ohme, Michael Pürrer, Xisco Jiménez Forteza, and Alejandro Bohé. Frequency-domain gravitational waves from nonprecessing black-hole binaries. II. A phenomenological model for the advanced detector era. *Phys. Rev. D*, 93:044007, Feb 2016.
- [56] A. Klypin, A. V. Kravtsov, O. Valenzuela, and F. Prada. Where Are the Missing Galactic Satellites? *apj*, 522:82–92, September 1999.

- [57] C. S. Kochanek. The implications of lenses for galaxy structure. *ApJ*, 373:354–368, June 1991.
- [58] Edward W. Kolb and Michale S. Turner. *The Early Universe*. Westview Press, 1994.
- [59] L. V. E. Koopmans, T. Treu, A. S. Bolton, S. Burles, and L. A. Moustakas. The Sloan Lens ACS Survey. III. The Structure and Formation of Early-Type Galaxies and Their Evolution since $z \sim 1$. *ApJ*, 649:599–615, October 2006.
- [60] Kerstin E. Kunze. An introduction to cosmology. In *Proceedings, 8th CERN–Latin-American School of High-Energy Physics (CLASHEP2015): Ibarra, Ecuador, March 05-17, 2015*, pages 177–212, 2016.
- [61] Kwun-Hang Lai, Otto A. Hannuksela, Antonio Herrera-Martín, Jose M. Diego, Tom Broadhurst, and Tjonnie G. F. Li. Discovering intermediate-mass black hole lenses through gravitational wave lensing. 2018.
- [62] J.-W. Lee. Is Dark Matter a BEC or Scalar Field? *Journal of Korean Physical Society*, 54:2622, June 2009.
- [63] J.-W. Lee. Brief History of Ultra-light Scalar Dark Matter Models. *ArXiv e-prints*, April 2017.
- [64] T.G.F. Li. *Extracting Physics from Gravitational Waves: Testing the Strong-field Dynamics of General Relativity and Inferring the Large-scale Structure of the Universe*. Springer Theses. Springer International Publishing, 2015.
- [65] K. Liao, X.-L. Fan, X.-H. Ding, M. Biesiada, and Z.-H. Zhu. Precision cosmology from future lensed gravitational wave and electromagnetic signals. *ArXiv e-prints*, March 2017.
- [66] Andrew Liddle. *An Introduction to Modern Cosmology*. WILEY, 2003.
- [67] Andrew R. Liddle and David H. Lyth. *Cosmological Inflation and Large-Scale Structure*. Cambridge University Press, 2000.

- [68] David H. Lyth and Andrew R. Liddle. *The Primordial Density Perturbation*. Cambridge University Press, 2009.
- [69] A. V. Macciò, S. Paduroiu, D. Anderhalden, A. Schneider, and B. Moore. Cores in warm dark matter haloes: a Catch 22 problem. *mnras*, 424:1105–1112, August 2012.
- [70] D. J. E. Marsh and A.-R. Pop. Axion dark matter, solitons, and the cusp-core problem. *ArXiv e-prints*, February 2015.
- [71] D. V. Martynov, E. D. Hall, B. P. Abbott, R. Abbott, T. D. Abbott, C. Adams, R. X. Adhikari, R. A. Anderson, S. B. Anderson, K. Arai, and et al. Sensitivity of the Advanced LIGO detectors at the beginning of gravitational wave astronomy. *Phys. Rev. D*, 93(11):112004, June 2016.
- [72] Tonatiuh Matos, Francisco Siddhartha Guzman, and L. Arturo Urena-Lopez. Scalar field as dark matter in the universe. *Class.Quant.Grav.*, 17:1707–1712, 2000.
- [73] Tonatiuh Matos and Arturo Ureña López. Further analysis of a cosmological model with quintessence and scalar dark matter. *PHYSICAL REVIEW D*, 63(063506), 2001.
- [74] Tonatiuh Matos, Jose-Ruben Luevano, Israel Quiros, L. Arturo Urena-Lopez, and Jose Alberto Vazquez. Dynamics of Scalar Field Dark Matter With a Cosh-like Potential. *Phys.Rev.*, D80:123521, 2009.
- [75] Tonatiuh Matos and L. Arturo Urena-Lopez. Quintessence and scalar dark matter in the universe. *Class.Quant.Grav.*, 17:L75–L81, 2000.
- [76] Tonatiuh Matos and L. Arturo Urena-Lopez. A Further analysis of a cosmological model of quintessence and scalar dark matter. *Phys.Rev.*, D63:063506, 2001.
- [77] Tonatiuh Matos and L. Arturo Urena-Lopez. Scalar field dark matter, cross-section and Planck scale physics. *Phys.Lett.*, B538:246–250, 2002.

- [78] S. Mollerach and E. Roulet. *Gravitational Lensing and Microlensing*. World Scientific, 2002.
- [79] V. Mukhanov. *Physical foundations of cosmology*. 2005. Cambridge, UK: Univ. Pr. (2005) 421 p.
- [80] Takahiro T. Nakamura. Gravitational Lensing of Gravitational Waves from Inspiral Binaries by a Point Mass Lens. *Phys. Rev. Lett.*, 80:1138–1141, Feb 1998.
- [81] Takahiro T. Nakamura and Shuji Deguchi. Wave Optics in Gravitational Lensing. *Progress of Theoretical Physics Supplement*, 133:137–153, 1999.
- [82] Yasusada Nambu. Wave Optics and Image Formation in Gravitational Lensing. *International Journal of Astronomy and Astrophysics*, 3(1):1–7, 2013.
- [83] J. F. Navarro, C. S. Frenk, and S. D. M. White. A Universal Density Profile from Hierarchical Clustering. *ApJ*, 490:493–508, December 1997.
- [84] E. R. Newton, P. J. Marshall, T. Treu, M. W. Auger, R. Gavazzi, A. S. Bolton, L. V. E. Koopmans, and L. A. Moustakas. The Sloan Lens ACS Survey. XI. Beyond Hubble Resolution: Size, Luminosity, and Stellar Mass of Compact Lensed Galaxies at Intermediate Redshift. *ApJ*, 734:104, June 2011.
- [85] Ken K. Y. Ng, Kaze W. K. Wong, Tjonnie G. F. Li, and Tom Broadhurst. Precise LIGO Lensing Rate Predictions for Binary Black Holes. *Phys. Rev.*, B96:155205, 2017.
- [86] H. C. Ohanian. Focusing of Gravitational Radiation. *Phys. Rev. D*, 8:2734–2735, October 1973.
- [87] Hans C. Ohanian. On the focusing of gravitational radiation. *International Journal of Theoretical Physics*, 9(6):425–437, Jun 1974.
- [88] T. Padmanabhan. *Structure formation in the universe*. Cambridge University Press, 1993.

- [89] Papastergis, E., Giovanelli, R., Haynes, M. P., and Shankar, F. Is there a “too big to fail” problem in the field? *A&A*, 574:A113, 2015.
- [90] Y. Park and H. C. Ferguson. Gravitational Lensing by Burkert Halos. *apjl*, 589:L65–L68, June 2003.
- [91] P. C. Peters. Index of refraction for scalar, electromagnetic, and gravitational waves in weak gravitational fields. *Phys. Rev. D*, 9:2207–2218, Apr 1974.
- [92] A. Piórkowska, M. Biesiada, and Z.-H. Zhu. Strong gravitational lensing of gravitational waves in Einstein Telescope. *J. Cosmology Astropart. Phys.*, 10:022, October 2013.
- [93] Planck Collaboration, P. A. R. Ade, N. Aghanim, C. Armitage-Caplan, M. Arnaud, M. Ashdown, F. Atrio-Barandela, J. Aumont, C. Baccigalupi, A. J. Banday, and et al. Planck 2013 results. XVI. Cosmological parameters. *aap*, 571:A16, November 2014.
- [94] Planck Collaboration, P. A. R. Ade, N. Aghanim, M. Arnaud, M. Ashdown, J. Aumont, C. Baccigalupi, A. J. Banday, R. B. Barreiro, J. G. Bartlett, and et al. Planck 2015 results. XIII. Cosmological parameters. *ArXiv e-prints*, February 2015.
- [95] M. S. Roberts. M 31 and a Brief History of Dark Matter. In A. H. Bridle, J. J. Condon, and G. C. Hunt, editors, *Frontiers of Astrophysics: A Celebration of NRAO’s 50th Anniversary*, volume 395 of *Astronomical Society of the Pacific Conference Series*, page 283, August 2008.
- [96] V. H. Robles, V. Lora, T. Matos, and F. J. Sanchez-Salcedo. Evolution of a dwarf satellite galaxy embedded in a scalar field dark matter halo. *ArXiv e-prints*, April 2014.
- [97] Victor H. Robles and T. Matos. Flat central density profile and constant dark matter surface density in galaxies from scalar field dark matter. *Monthly Notices of the Royal Astronomical Society*, 422(1):282, 2012.

- [98] Remo Ruffini and Silvano Bonazzola. Systems of selfgravitating particles in general relativity and the concept of an equation of state. *Phys. Rev.*, 187:1767–1783, 1969.
- [99] Barbara Ryden. *Introduction to Cosmology*. Addison Wesley, 2003.
- [100] H.-Y. Schive, M.-H. Liao, T.-P. Woo, S.-K. Wong, T. Chiueh, T. Broadhurst, and W.-Y. P. Hwang. Understanding the Core-Halo Relation of Quantum Wave Dark Matter from 3D Simulations. *Physical Review Letters*, 113(26):261302, December 2014.
- [101] Schive Hsi-Yu, Chiueh Tzihong, and Broadhurst Tom. Cosmic structure as the quantum interference of a coherent dark wave. *Nat Phys*, 10(7):496–499, jul 2014.
- [102] P. Schneider, J. Ehlers, and E.E. Falco. *Gravitational Lenses*. Astronomy and Astrophysics Library. Springer, 1999.
- [103] P. Schneider, G. Meylan, C. Kochanek, P. Jetzer, P. North, and J. Wambsganss. *Gravitational Lensing: Strong, Weak and Micro: Saas-Fee Advanced Course 33*. Saas-Fee Advanced Course. Springer Berlin Heidelberg, 2006.
- [104] B.F. Schutz. *A First Course in General Relativity*. Series in physics. Cambridge University Press, 1985.
- [105] Bodo Schwabe, Jens C. Niemeyer, and Jan F. Engels. Simulations of solitonic core mergers in ultralight axion dark matter cosmologies. *Phys. Rev.*, D94(4):043513, 2016.
- [106] Edward Seidel and Wai-Mo Suen. Oscillating soliton stars. *Phys. Rev. Lett.*, 66:1659–1662, Apr 1991.
- [107] M. Sereno, P. Jetzer, A. Sesana, and M. Volonteri. Cosmography with strong lensing of LISA gravitational wave sources. *MNRAS*, 415:2773–2781, August 2011.

- [108] Sanjib Sharma. Markov Chain Monte Carlo Methods for Bayesian Data Analysis in Astronomy. *Annual Review of Astronomy and Astrophysics*, 55(1):213–259, 2017.
- [109] Sang-Jin Sin. Late-time phase transition and the galactic halo as a Bose liquid. *Phys. Rev. D*, 50:3650–3654, Sep 1994.
- [110] D.S. Sivia and J. Skilling. *Data analysis: a Bayesian tutorial*. Oxford science publications. Oxford University Press, 2006.
- [111] John Skilling. Nested sampling for general Bayesian computation. *Bayesian Anal.*, 1(4):833–859, 12 2006.
- [112] Graham P. Smith, Mathilde Jauzac, John Veitch, Richard Massey, Johan Richard, and Will M. Farr. What if the gravitational waves detected in 2015 were strongly lensed by massive galaxy clusters? 2017.
- [113] S. Smith. The Mass of the Virgo Cluster. *ApJ*, 83:23, January 1936.
- [114] Jay Strader, Anil C. Seth, Duncan A. Forbes, Giuseppina Fabbiano, Aaron J. Romanowsky, Jean P. Brodie, Charlie Conroy, Nelson Caldwell, Vincenzo Pota, Christopher Usher, and Jacob A. Arnold. The Densest Galaxy. *The Astrophysical Journal Letters*, 775(1):L6, 2013.
- [115] M. F. Struble and H. J. Rood. A Compilation of Redshifts and Velocity Dispersions for ACO Clusters. *ApJS*, 125:35–71, November 1999.
- [116] K.-Y. Su and P. Chen. Solving the cusp-core problem with a novel scalar field dark matter. *jcap*, 8:16, August 2011.
- [117] Abril Suarez and Tonatiuh Matos. Structure Formation with Scalar Field Dark Matter: The Fluid Approach. *Mon. Not. Roy. Astron. Soc.*, 416:87, 2011.
- [118] Abril Suárez, Victor H. Robles, and Tonatiuh Matos. A Review on the Scalar Field/Bose-Einstein Condensate Dark Matter Model. *Astrophys. Space Sci. Proc.*, 38:107–142, 2014.

-
- [119] T. Suyama, R. Takahashi, and S. Michikoshi. Wave propagation in a weak gravitational field and the validity of the thin lens approximation. *Phys. Rev. D*, 72(4):043001, August 2005.
- [120] Teruaki Suyama, Takahiro Tanaka, and Ryuichi Takahashi. Exact wave propagation in a spacetime with a cosmic string. *Phys. Rev. D*, 73:024026, Jan 2006.
- [121] R. Takahashi. Quasi-geometrical optics approximation in gravitational lensing. *A&A*, 423:787–792, September 2004.
- [122] R. Takahashi and T. Chiba. Gravitational Lens Statistics and the Density Profile of Dark Halos. *ApJ*, 563:489–496, December 2001.
- [123] R. Takahashi, T. Suyama, and S. Michikoshi. Scattering of gravitational waves by the weak gravitational fields of lens objects. *A&A*, 438:L5–L8, July 2005.
- [124] Ryuichi Takahashi. Amplitude and Phase Fluctuations for Gravitational Waves Propagating through Inhomogeneous Mass Distribution in the Universe. *The Astrophysical Journal*, 644(1):80, 2006.
- [125] Ryuichi Takahashi. Arrival time differences between gravitational waves and electromagnetic signals due to gravitational lensing. *Astrophys. J.*, 835(1):103, 2017.
- [126] Ryuichi Takahashi and Takashi Nakamura. Wave Effects in the Gravitational Lensing of Gravitational Waves from Chirping Binaries. *The Astrophysical Journal*, 595(2):1039, 2003.
- [127] ET Science Team. Einstein gravitational wave telescope conceptual design study, 2017. Available from European Gravitational Observatory, document number ET-0106C-10.
- [128] T. Treu, L. V. Koopmans, A. S. Bolton, S. Burles, and L. A. Moustakas. The Sloan Lens ACS Survey. II. Stellar Populations and Internal Structure of Early-Type Lens Galaxies. *ApJ*, 640:662–672, April 2006.

- [129] Michael S. Turner. Coherent Scalar Field Oscillations in an Expanding Universe. *Phys.Rev.*, D28:1243, 1983.
- [130] L. Arturo Urena-Lopez. Bose-Einstein condensation of relativistic Scalar Field Dark Matter. *JCAP*, 0901:014, 2009.
- [131] L. Arturo Urena-Lopez. Nonrelativistic approach for cosmological scalar field dark matter. *Phys. Rev.*, D90(2):027306, 2014.
- [132] Don van Ravenzwaaij, Pete Cassey, and Scott D. Brown. A simple introduction to Markov Chain Monte-Carlo sampling. *Psychonomic Bulletin & Review*, Mar 2016.
- [133] M. A. Varvella, M. C. Angonin, and P. Tournenc. Increase of the Number of Detectable Gravitational Waves Signals Due to Gravitational Lensing. *General Relativity and Gravitation*, 36:983–999, May 2004.
- [134] Benjamin D. Wandelt, Romeel Dave, Glennys R. Farrar, Patrick C. McGuire, David N. Spergel, et al. Selfinteracting dark matter. pages 263–274, 2000.
- [135] Y. Wang, A. Stebbins, and E. L. Turner. Gravitational Lensing of Gravitational Waves from Merging Neutron Star Binaries. *Physical Review Letters*, 77:2875–2878, September 1996.
- [136] J.A. Wheeler and K. Ford. *Geons, Black Holes, and Quantum Foam: A Life in Physics*. W. W. Norton, 2010.
- [137] S. Winitzki. A handy approximation for the error function and its inverse, 2008. Available online at <http://sites.google.com/site/winitzki/sergei-winitzkis-files/erf-approx.pdf>.
- [138] C. O. Wright and T. G. Brainerd. Gravitational Lensing by NFW Halos. *apj*, 534:34–40, May 2000.

-
- [139] C.-M. Yoo, K.-I. Nakao, H. Kozaki, and R. Takahashi. Lensing Effects on Gravitational Waves in a Clumpy Universe. In H. Kleinert, R. T. Jantzen, and R. Ruffini, editors, *The Eleventh Marcel Grossmann Meeting On Recent Developments in Theoretical and Experimental General Relativity, Gravitation and Relativistic Field Theories*, pages 1728–1730, September 2008.
- [140] F. Zwicky. On the Masses of Nebulae and of Clusters of Nebulae. *ApJ*, 86:217, October 1937.

Appendix A

Galaxy posteriors

This appendix contains the posteriors for the extra galaxies studied on chapter 5. They are for the soliton+NFW tail case.

The detailed description from the results obtained are described in chapter 5. In short, section A.1 groups the figures containing the posteriors for a soliton mass $M_s = 10^{11.5}$. This is considering that this the limit case where the soliton dominates the contribution. section A.2 contains the figures for any soliton mass $M_s < 10^{11.5}$. This are the posteriors with the actual constraints.

A.1 Posteriors for $M_s = 10^{11.5}$

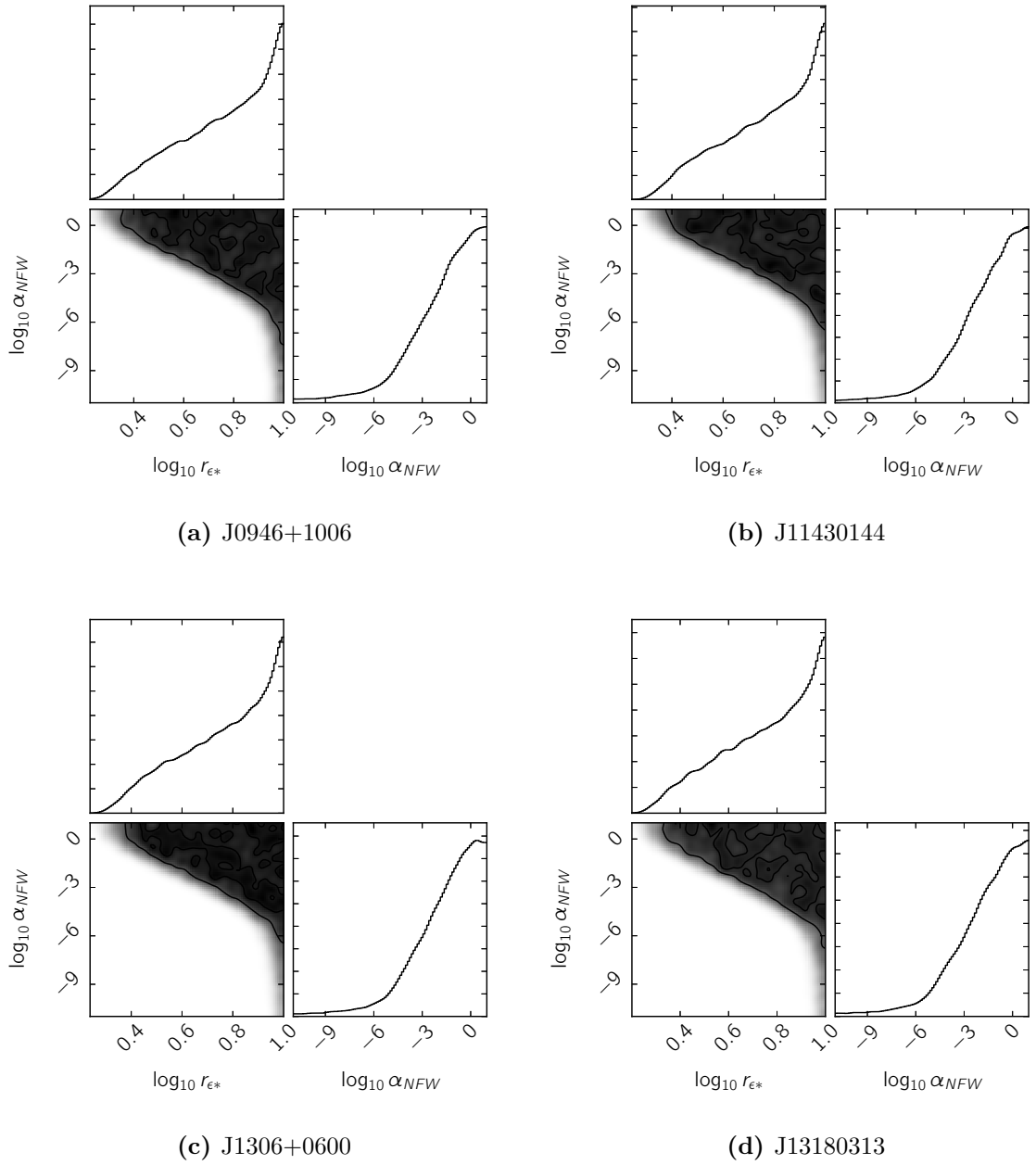


Figure A.1: Posteriors for a configuration soliton+NFW tail considering $m_{a22} = 10$ and a soliton mass $M_s = 10^{11.5}$. The Galaxy labels is specified in each subfigure, and description in chapter 5.

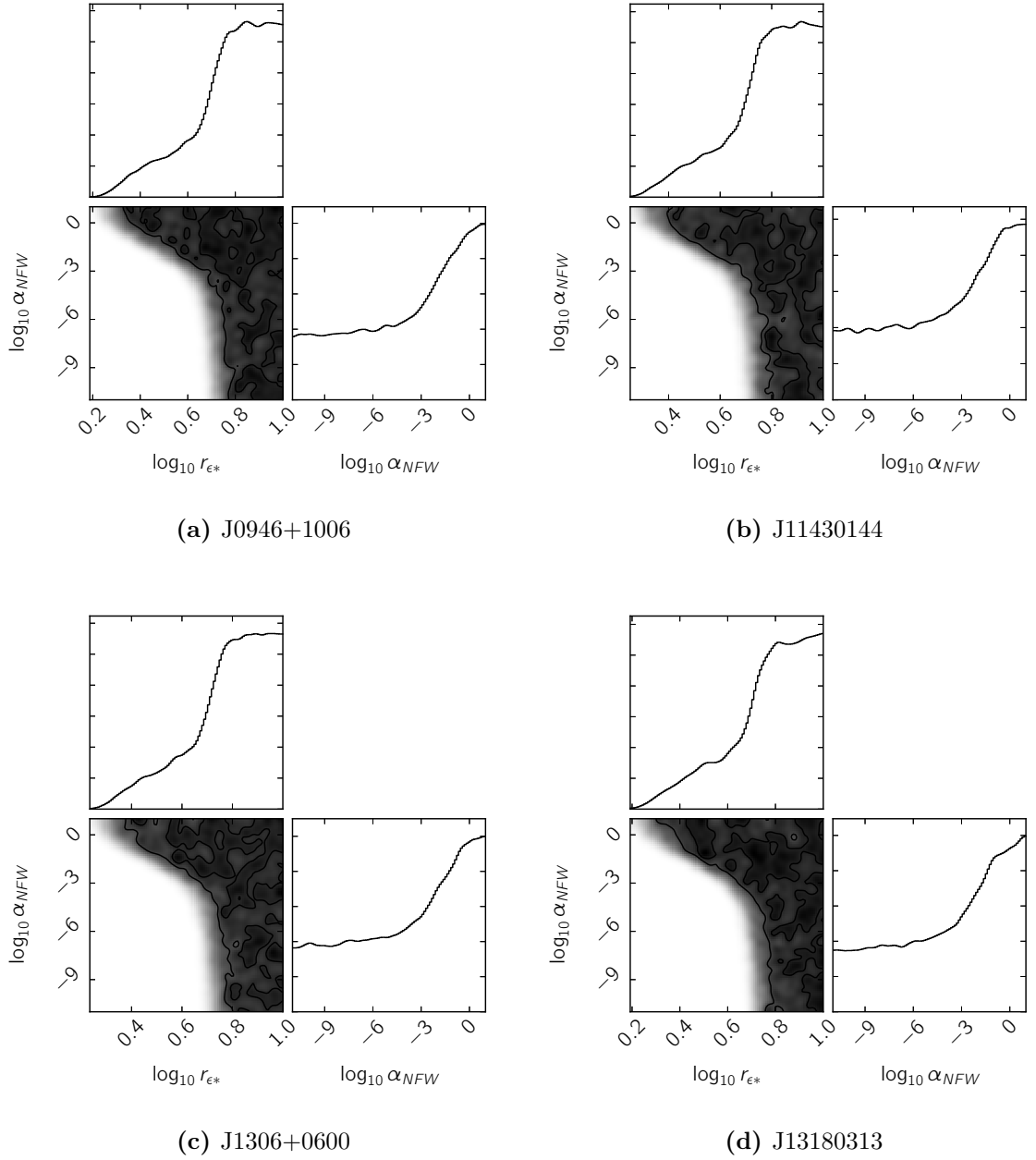


Figure A.2: Posteriors for a configuration soliton+NFW tail considering $m_{a22} = 1$ and a soliton mass $M_s = 10^{11.5}$. A transition value where the soliton has dominance is clearly delimited. The Galaxy labels is specified in each subfigure, and description in chapter 5.

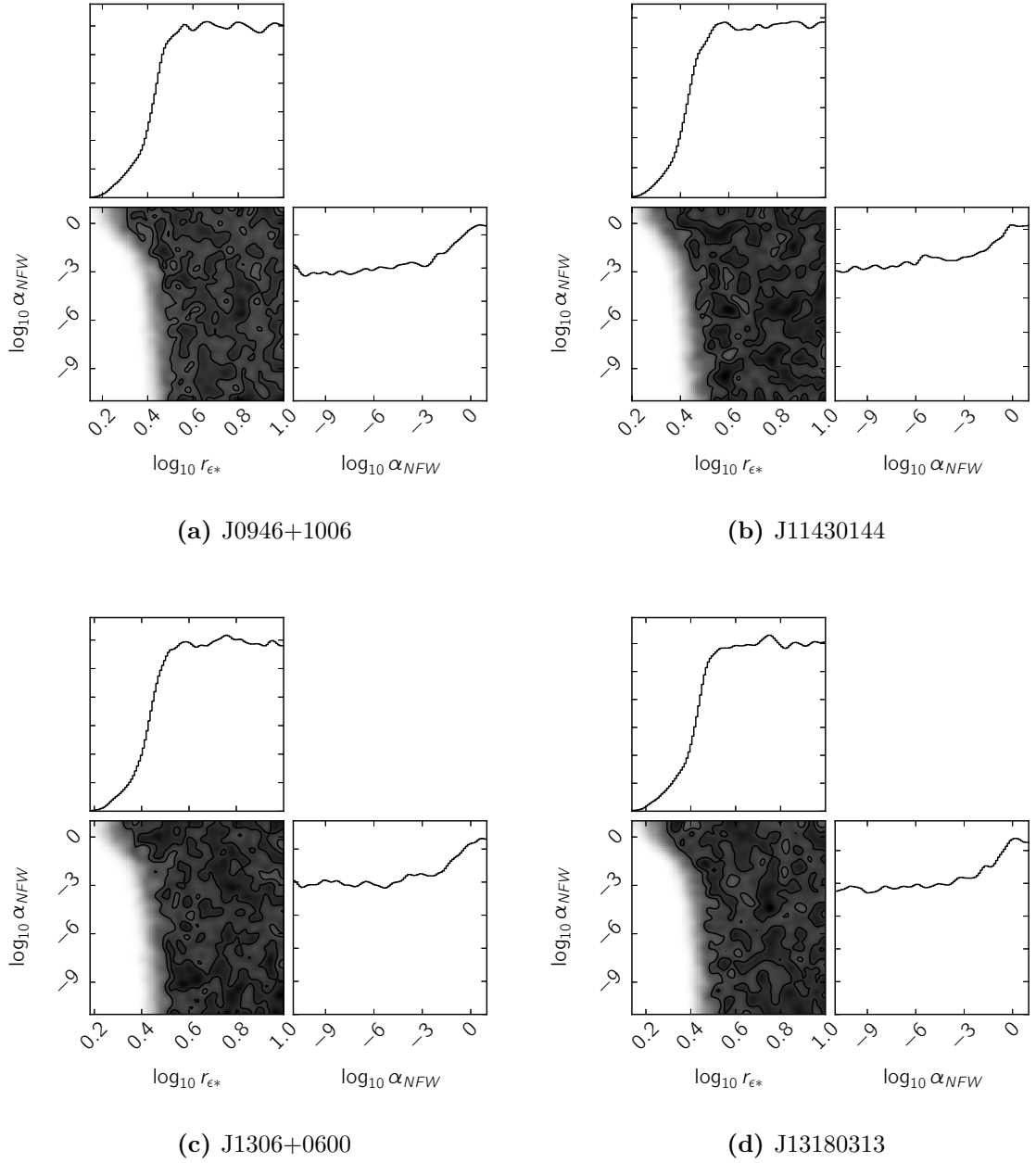


Figure A.3: Posteriors for a configuration soliton+NFW tail considering $m_{a22} = 0.1$ and a soliton mass $M_s = 10^{11.5}$. This is the particular case where the soliton dominates the configuration. This has the particular feature that the configuration of the tail is irrelevant. The Galaxy labels is specified in each subfigure, and description in chapter 5.

A.2 Posteriors for $M_s < 10^{11.5}$

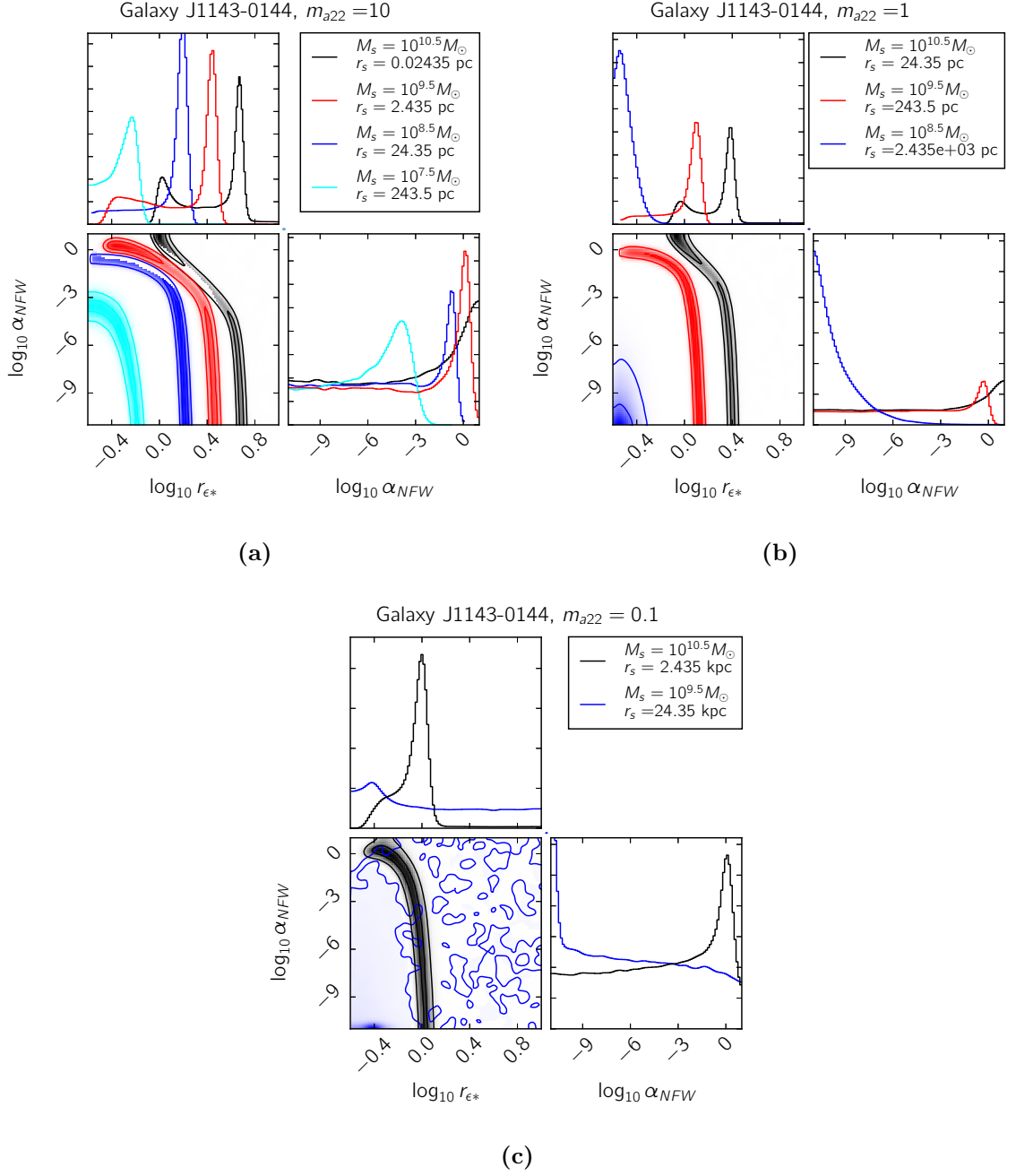


Figure A.4: Posteriors for a configuration soliton+NFW tail considering different axion masses and soliton mass $M_s < 10^{11.5}$. The Galaxy labels is specified in each subfigure, and description in chapter 5.

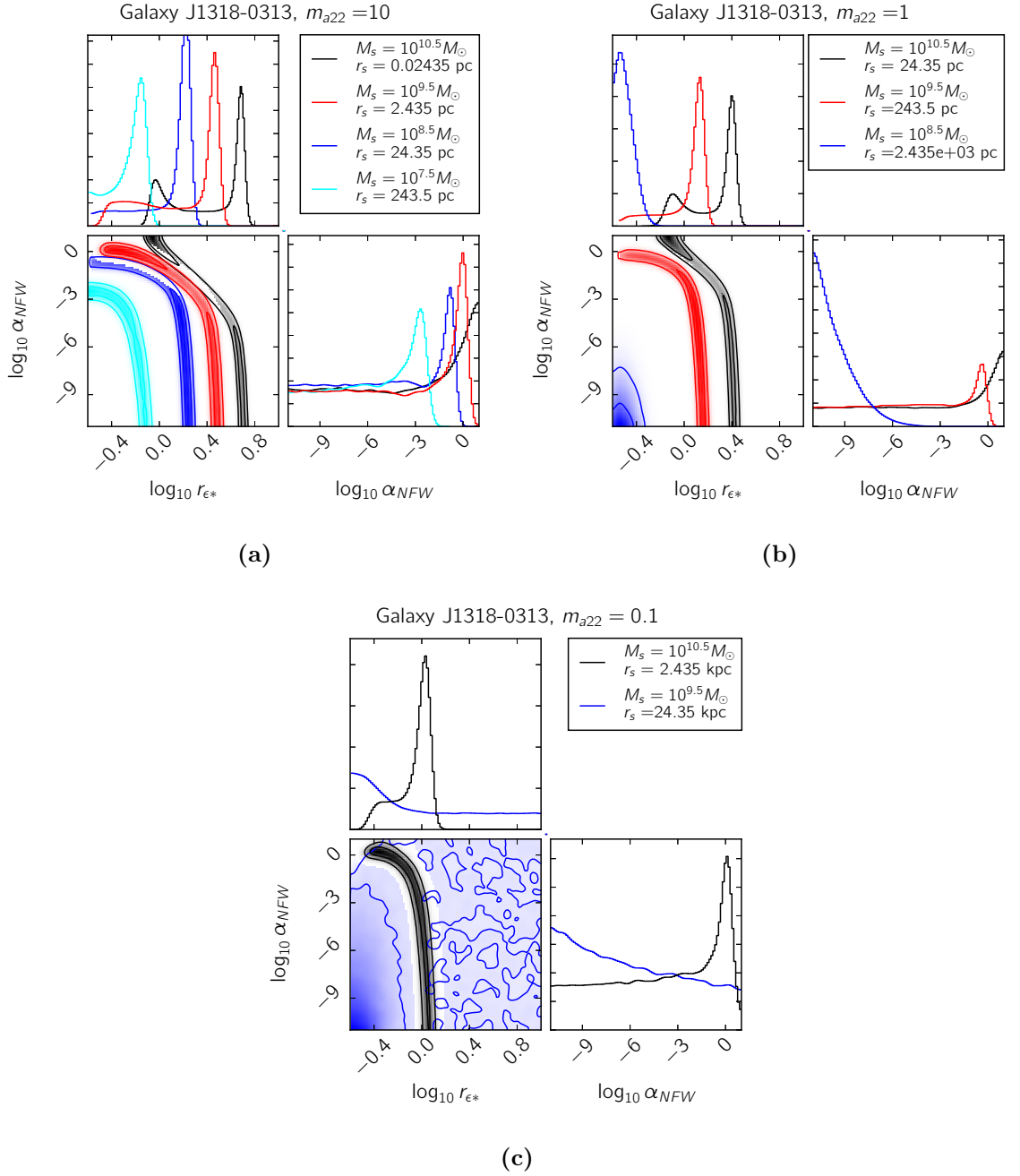


Figure A.5: Posteriors for a configuration soliton+NFW tail considering different axion masses and soliton mass $M_s < 10^{11.5}$. The Galaxy labels is specified in each subfigure, and description in chapter 5.

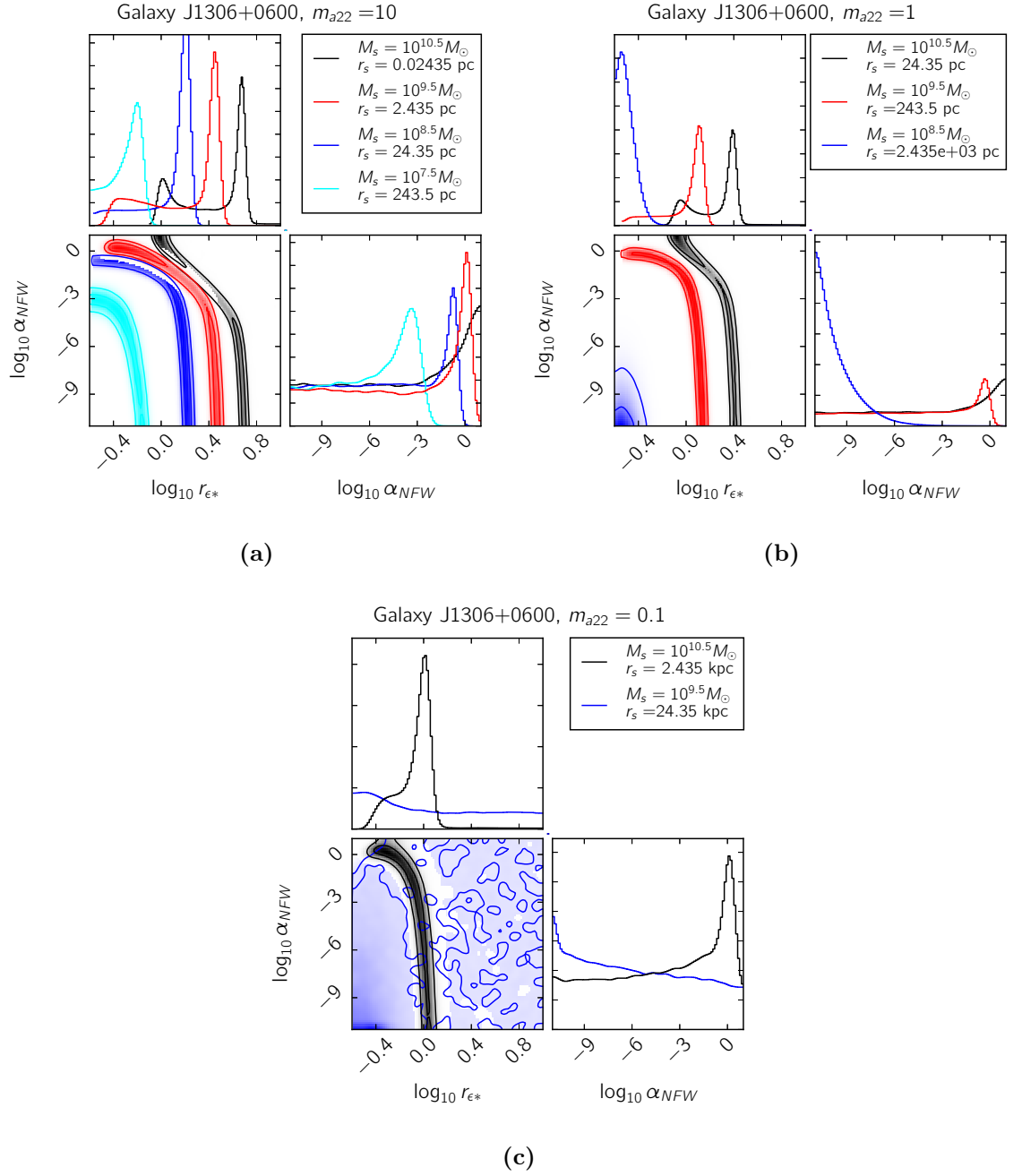


Figure A.6: Posteriors for a configuration soliton+NFW tail considering different axion masses and soliton mass $M_s < 10^{11.5}$. The Galaxy labels is specified in each subfigure, and description in chapter 5.

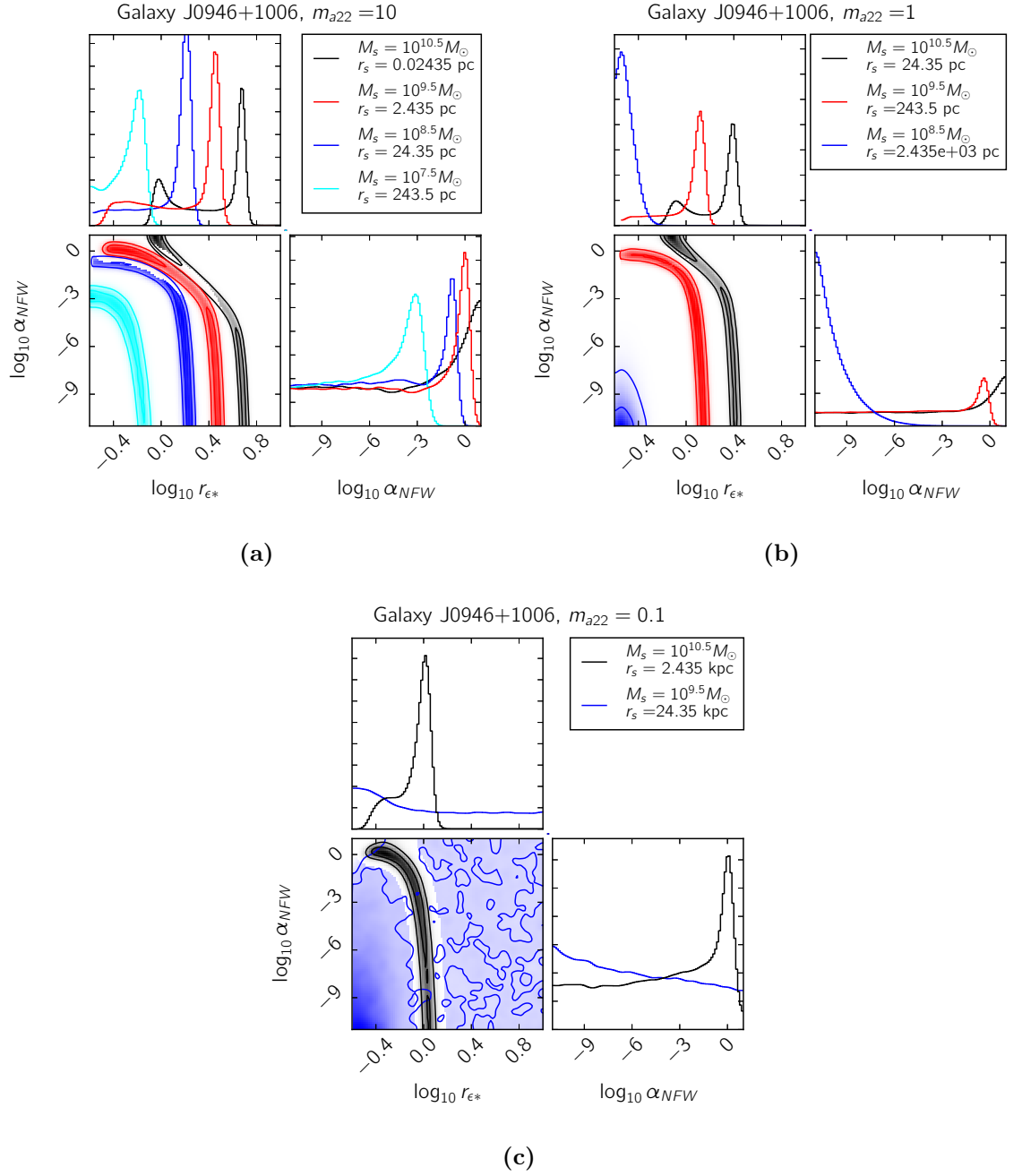


Figure A.7: Posteriors for a configuration soliton+NFW tail considering different axion masses and soliton mass $M_s < 10^{11.5}$. The Galaxy labels is specified in each subfigure, and description in chapter 5.

Appendix B

Lensing figures

This appendix contains a gallery of lensing impressions obtained using the functions derived in chapter 4. The figures represent selected lens positions acting over a small source centred at the origin. Nevertheless, they are presented only for illustrative purposes as lensing is an effect observed mainly on images, and it was appropriate to translate the abstract concepts into visual examples. To emphasize, no analysis or conclusions are extracted from them, and any remarks done are results obtained from the analysis of the properties for the lensing equations detailed in chapters 4 and 5 and are stated for clarity to the reader.

The images are presented in the following order:

- A shared source centred at $(0, 0)$ with respect to the lens position.
- Images of a point mass lens.
- Images of the solito-core profile.
- Images of the waveDM profile.

To maintain the gallery simple, only two positions of the lens were considered; one with the lens centred at the origin and presenting an Einstein ring, and a lens situated at the position $(0.2, 0.2)$ of the relative axes which are normalized according to each lens for the situation of an off-axis lens.

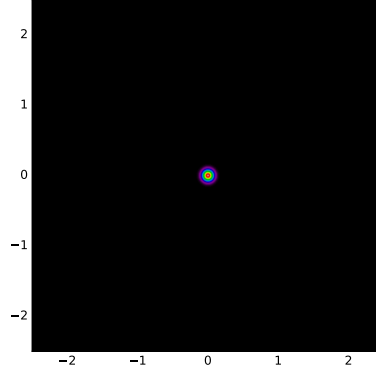


Figure B.1: Source considered for all lenses. Its position is at the origin of the axes, and their sizes are relative to each lens normalization.

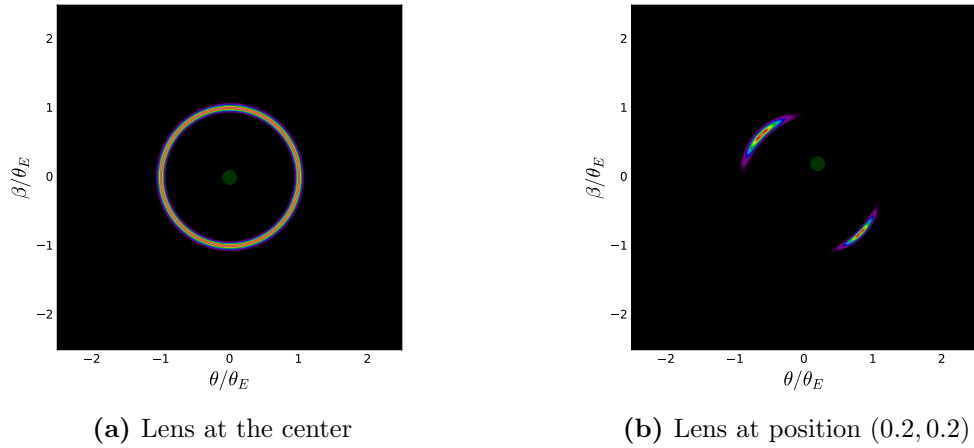


Figure B.2: An example of a point mass as a reference. The small green region in both images is a loose representation used to identify the position of the lens. The axes are normalized by the Einstein angle, so this provides a normalized lens mass of 1.

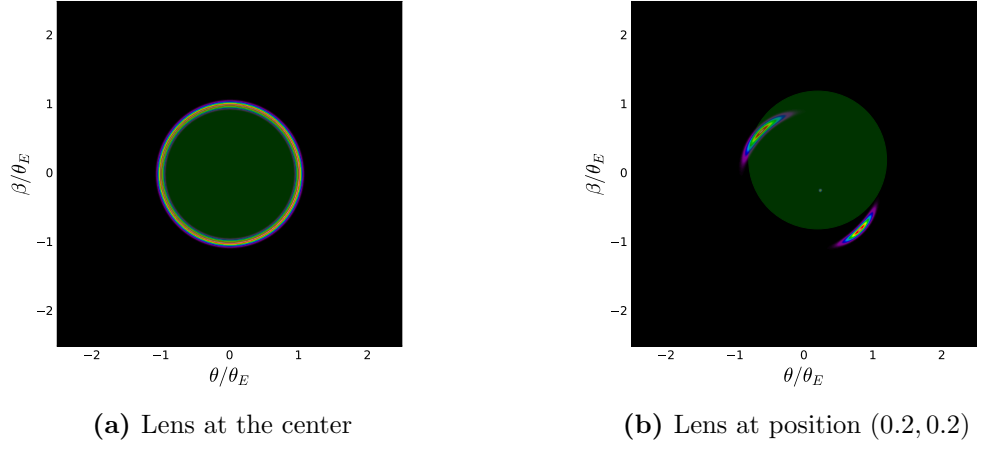


Figure B.3: The images represent a soliton core where its characteristic length, r_s , corresponds to its Einstein radius. This fixes that $\lambda \approx 3.18$ in the dimensionless lens equation. Additionally, the green region represents the hypothetical size core, and it is clear from resulting images that the lensing of the source is similar to a point mass lens.

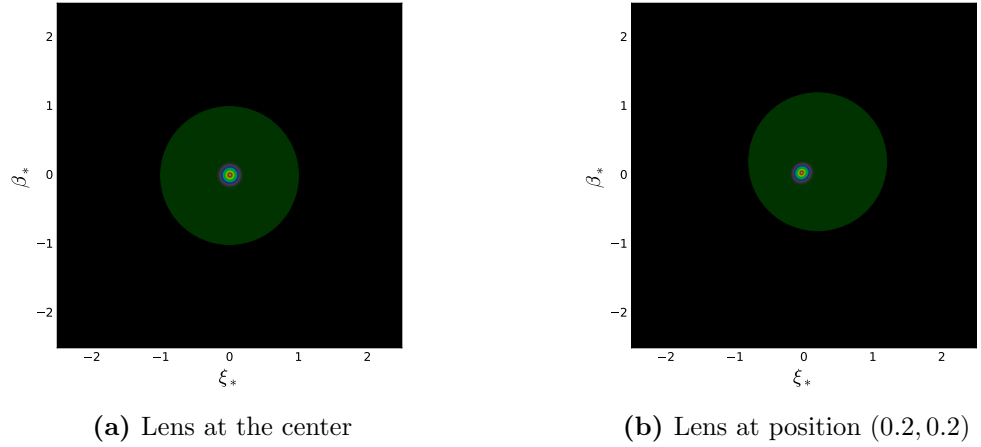


Figure B.4: A case of a soliton core with a parameter λ below λ_{crit} in the dimensionless lens equation. The green region represents the hypothetical size of the core. It is clear that the source experiences a minimum aberration as the lens is not able to produce strong lensing. This is an effect in the weak lensing regime.

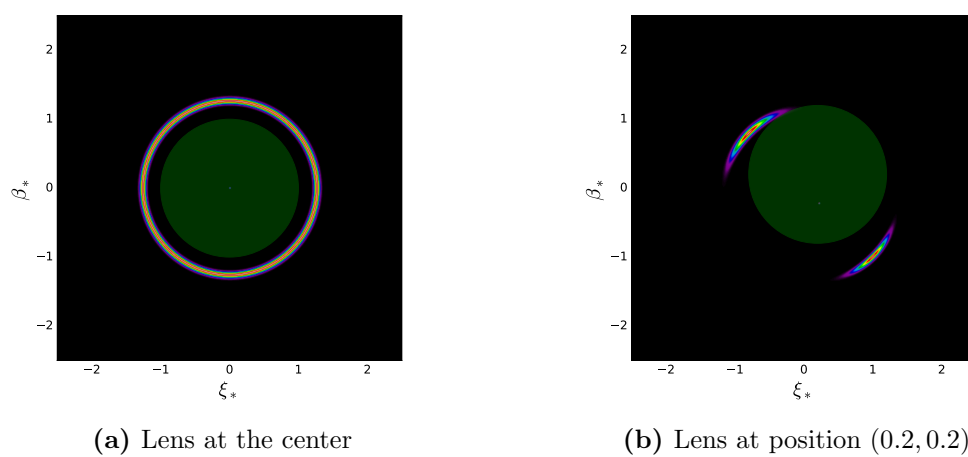


Figure B.5: Images presenting a soliton core with $\lambda = 5$ in the dimensionless lens equation. The green region represents the hypothetical size of the core. It is clear on both images that the relative Einstein ring and the image separations have a larger radius than the core.

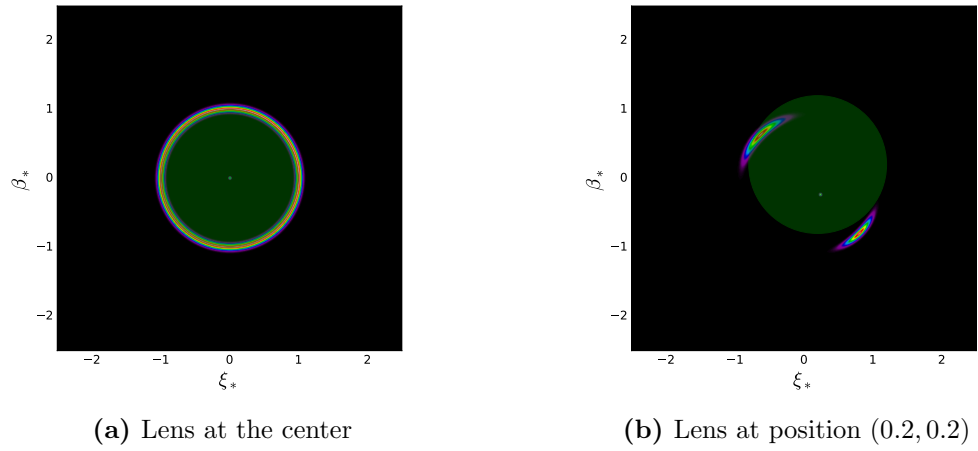


Figure B.6: The images introduce the Wave Dark Matter profile with a parameter $\lambda \approx 2.96$ in the dimensionless lens equation; $r_{\epsilon^*} = 1$, and $\alpha_{\text{NFW}} = 0.5$ for the lensing parameters. The green region represents the hypothetical size of the core. By observing the size, it is clear that this case is similar to the soliton core-only specially by considering the values of λ and r_{ϵ^*} which are conclusions described in the results of chapter 5.

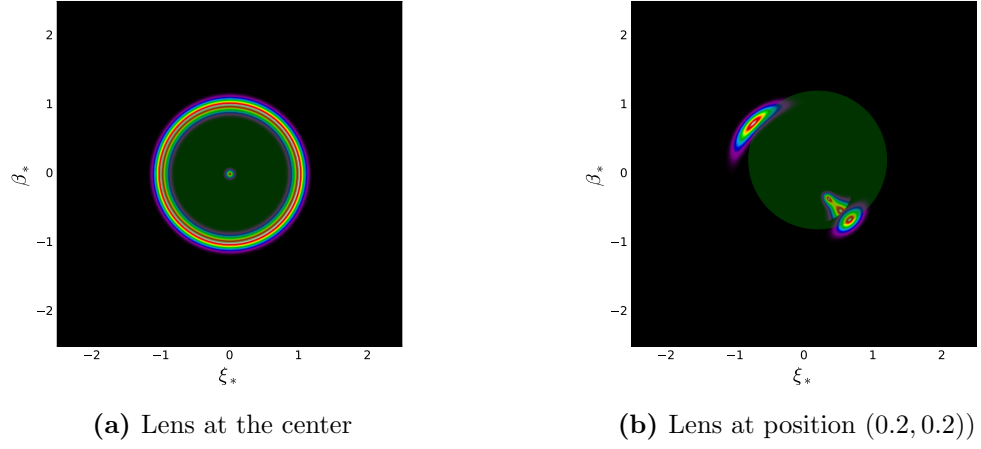


Figure B.7: The images present a Wave Dark Matter profile with $\lambda \approx 1.005$ in the dimensionless lens equation; $r_{\epsilon^*} = 0.5$, and $\alpha_{\text{NFW}} = 0.5$ for the lensing parameters. Even that $r_s \approx R_E$, the contribution of the NFW tail produces a noticeable difference in thickness compared with the soliton core and the point mass. The green region represents the hypothetical size of the core.

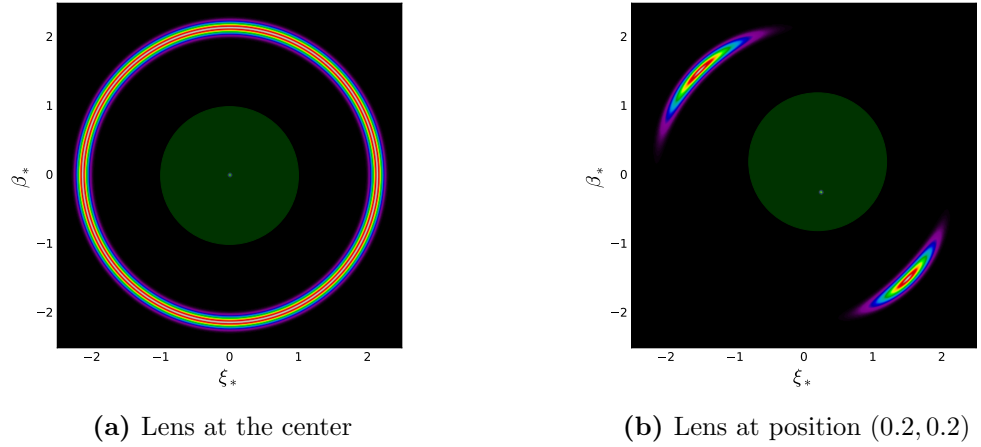


Figure B.8: The images present a Wave Dark Matter profile with $\lambda = 5$ in the dimensionless lens equation; $r_{\epsilon^*} = 0.5$ and $\alpha_{\text{NFW}} = 0.5$ for the lensing parameters. It is clear that the Einstein radius is bigger than the core. The green region represents the hypothetical size of the core.